EFFICIENT EUV LIGHT PLASMA SOURCES DRIVEN BY A 2-μm-WAVELENGTH LASER

Ph.D. thesis, Vrije Universiteit Amsterdam, 2023
Efficient EUV light plasma sources driven by a 2-μm-wavelength laser
Lars Behnke

Cover layout and design: Timo Wolf Kamp, persoonlijkproefschrift.nl
Print: Ridderprint, www.ridderprint.nl

ISBN 978-94-6483-376-8
An electronic version of this dissertation is available at: `research.vu.nl`

VRIJE UNIVERSITEIT

Efficient EUV Light Plasma Sources Driven by a 2-µm-Wavelength Laser

ACADEMISCH PROEFSCHRIFT

ter verkrijging van de graad van Doctor
aan de Vrije Universiteit Amsterdam,
op gezag van de rector magnificus
prof.dr. J.J.G. Geurts,
in het openbaar te verdedigen
ten overstaan van de promotiecommissie
van de Faculteit der Bètawetenschappen
op maandag 2 oktober 2023 om 11.45 uur
in een bijeenkomst van de universiteit,
De Boelelaan 1105

door

Lars Peter Behnke

geboren te Iserlohn, Duitsland

promotoren: dr. O.O. Versolato
prof.dr. W.M.G. Ubachs

promotiecommissie: prof.dr. A. Freise
prof.dr. H.L. Offerhaus
prof.dr. G. Kroesen
prof.dr. R. Abhari
dr. L.S. Dreissen

The work described in this thesis was carried out at the Advanced Research Center for Nanolithography (ARCNL), a public-private partnership between the University of Amsterdam (UvA), the Vrije Universiteit Amsterdam (VU), the University of Groningen (RUG), the Netherlands Organisation for Scientific Research (NWO), and the semiconductor equipment manufacturer ASML.

CONTENTS

Introduction **1**
Thesis outline and summary 6

1 High-energy parametric oscillator and amplifier pulsed light source at 2-µm **9**
1.1 Introduction 10
1.2 Experimental setup 11
1.3 Optical Parametric Oscillator 14
1.4 Optical Parametric Amplifier 18
1.4.1 Output Energy 18
1.4.2 Spatial profiles 20
1.4.3 Temporal profiles 21
1.5 Spectrum and bandwidth 25
1.6 Conclusion 26
1.7 Acknowledgments 27

2 Extreme ultraviolet light from a tin plasma driven by a 2-µm-wavelength laser **29**
2.1 Introduction 30
2.2 Experimental setup 33
2.3 Results 35
2.4 Conclusion 42

3 Characterization of 1- and 2-µm-wavelength laser-produced microdroplet-tin plasma for generating extreme ultraviolet light 45
3.1 Introduction 46
3.2 Experiment 47
3.3 Scaling of spectral features with laser intensity and wavelength 48
3.4 Scaling of optical depth 55
3.5 Conclusions 59
3.A Appendix 61

4 Characterization of angularly resolved EUV emission from 2-µm-wavelength laser-driven Sn plasma using preformed liquid disk targets 63
4.1 Introduction 64
4.2 Method 65
4.3 EUV generation using 2-µm light on preformed targets 69
  4.3.1 Target diameter 69
  4.3.2 Laser intensity 73
  4.3.3 Pulse duration 74
4.4 EUV generation using 1- and 2-µm laser light 75
4.5 Conclusions 78
4.A Appendix 80

5 Highly efficient generation of EUV light using 2-µm-wavelength drive laser light 83
5.1 Introduction 84
5.2 Experimental details 86
5.3 Results 89
  5.3.1 Intensity and Pulse length scaling 89
  5.3.2 Target size scaling 93
  5.3.3 Scaling with spatial beam properties 98
5.4 Conclusion 103

Conclusion & Outlook 105

Bibliography 110

List of Publications 125

Acknowledgments 127

INTRODUCTION

Integrated circuits (ICs) are essential in modern life, providing the computing power necessary to process vast amounts of data and perform complex calculations. As the backbone of the digital age, high-performance ICs drive innovation and enable the seamless functioning of our increasingly interconnected world, shaping the future of technology and human progress. In the age of climate change and the growing demand for new technologies, the energy efficiency of integrated circuits has become increasingly important. Koomey's Law, which states that the number of computations per unit of energy approximately doubles every 1.5 years, highlights the increasing efficiency of ICs over the past decades [1]. This ongoing improvement in efficiency is largely driven by innovations in the semiconductor manufacturing process, particularly in the field of lithography.

Lithography, the process of creating patterns on a surface using light, is a crucial component of semiconductor device manufacturing. Miniaturization, an essential aspect of this process, enables the creation of ever smaller and more complex features on silicon wafers from which ICs are made, which ultimately leads to improved energy efficiency. Achieving miniaturization in lithography involves reducing the wavelength of the light and with it the ultimately reachable feature sizes that can be printed on a wafer. Since 2019, extreme ultraviolet (EUV) lithography (EUVL) has been adopted for high-volume manufacturing, using light of wavelength 13.5 nm [2]. Generating the 250 W of EUV light required for the cost-efficient use of EUVL machines is challenging. The 13.5 nm EUV light for these scanners is provided by an EUV source based on the irradiation of micrometer-sized droplets of molten tin by a series of laser pulses. First, a low energy *pre-pulse* deforms the droplet into a thin disk-shaped tin sheet. Second, a high-energy *main-pulse* then irradiates the sheet to create a plasma comprised of multiply charged Sn^{10+}– Sn^{14+} ions emitting the desired 13.5 nm EUV light. This EUV light is reflected toward the intermediate focus (IF), where the source connects to the scanner, by the multilayer collector mirror. A powerful CO_2-gas laser is used to create the high-energy *main-pulse* at 10 µm-laser-wavelength. CO_2-gas lasers were chosen as plasma drivers due to their good scalability of output power and high obtainable efficiency in transforming laser energy into usable EUV light at 13.5 nm. To obtain the required 250 W of EUV light, a laser average power of $\sim$ 25 kW achieved by $\sim$ 50 kHz repetition rates is necessary. The semiconductor roadmap even calls for a stable 1000 Watt source to enhance productivity, which would require quadrupling the current source performance, including a drastic increase in the required laser power.

Using CO_2-gas lasers has several drawbacks in addition to its large and expensive physical footprint. The main disadvantage is the poor efficiency of converting electrical power to laser light (wall plug efficiency) of approximately 2–3%, in the industrial application, leading to megawatt-level electrical power consumption for a single EUVL unit. Since the manufacturing of ICs increasingly dominates the total carbon emissions of many IC-based devices and applications [3], the semiconductor industry plays an important role in combating climate change. A considerable contribution to the carbon footprint of the semiconductor industry comes from the high power consumption of EUVL machines. Transitioning to modern solid-state lasers could potentially enhance the energy efficiency of EUVL systems drastically: For example, the Yb:YAG (disk) laser exhibits wall plug efficiencies of 20–30% [4], roughly a factor 10× higher than the wall plug efficiency of CO_2-gas lasers. In addition, a solid-state laser would require a smaller physical footprint and is expected to be more easily scaled to higher output powers to meet future EUV power scaling demands. High demands on the average power limit the selection of possible solid-state lasers suitable for driving the plasma in EUVL. Besides the already mentioned Yb:YAG laser or a Nd:YAG laser, the high-power big-aperture thulium (BAT) laser based on a concept introduced by Lawrence Livermore National Laboratory is a promising candidate for driving the EUV emitting plasma [5, 6]. The BAT laser operates near 2 µm-wavelength and is expected to have a wall plug efficiency comparable to that of the 1 µm-wavelength Yb:YAG or Nd:YAG laser. New solid-state lasers operating at longer wavelengths may be enabled by future advancements in laser technology. This promising selection of laser technologies raises the intriguing question: What is the optimum laser system for driving the next generation's EUV sources?

To help answer that question, the impact of the drive laser wavelength on the EUV-emitting plasma needs to be studied. An important plasma parameter for EUV source performance is the conversion efficiency (CE) of the drive laser pulse energy to usable EUV emission within the 2% wavelength bandwidth around 13.5 nm (this bandwidth is referred to as *in-band* and is due to the multilayer optics) emitted in the

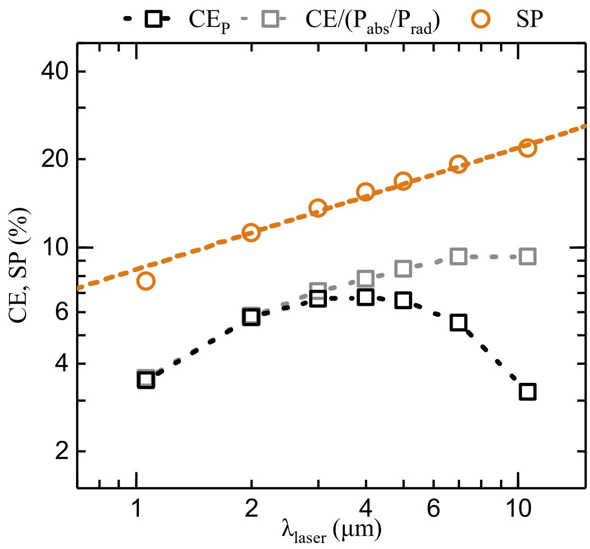

Figure 1: CE (black squares) and SP (yellow circles) as a function of laser wavelength. Data from radiation-hydrodynamics RALEF-2D simulations of plasma from a liquid tin droplet target, taken from Hemminga et al. [7]. Laser intensities are scaled with wavelength to be close to the optimum for in-band emission. Gray squares depict CE/(P_{abs}/P_{rad}) taking into only account the absorbed fraction P_{abs} of incoming laser energy P_{rad}, showing that reduced laser absorption is responsible for the declining CE beyond 4 µm laser wavelength.

2π steradian angle toward the collector mirror. Note, the CE is not only important to the overall efficiency of an EUV source but is also crucial to achieving the EUV source power requirements dictated by the semiconductor industry. Any lack in CE must be compensated with more laser power, potentially increasing the load from harmful plasma emissions such as tin debris, ions, and out-of-band radiation that may pose a risk to the costly EUV collector mirror. Another important parameter is the spectral purity (SP) of the EUV emission spectra, indicating the fraction of energy contained within the 13.5 nm in-band region over the energy in the spectral range from 5.5–25.5 nm. Experimental investigations have shown that $\sim$ 3% CE values can be reached when the droplet is directly irradiated by a 1-µm-wavelength *main-pulse* from an Nd:YAG laser, while plasma driven by a 10-µm-wavelength CO_2-gas laser reaches CE values of 5-6% (using a preformed disk target). Recent simulations performed for droplet-tin targets by Hemminga et al. [7] show a strong dependence of CE on the drive laser wavelength, as depicted in Fig1. This drive-wavelength dependence of CE can be explained by the interplay between increasing SP (yellow dots) and decreasing laser absorption of the tin plasma for increasing drive laser wavelength. The increase in SP with wavelength is attributed to reduced spectral broadening. This behavior is expected since the effective plasma density decreases with increasing drive laser wavelength leading to a reduction in optical depth which determines the spectral broadening. The decrease of laser absorption with wavelength is attributed to the decreasing typical plasma density with wavelength (see below) which correlates with increasing laser reflectivity. The CE corrected for the laser energy reflected by the plasma (gray squares; see the caption for details) shows a monotonic increase with drive wavelength, in line with the aforementioned reduction in optical depth. The laser absorptivity for laser wavelengths larger than 3 µm can be increased by pre-irradiating the tin droplet to transform it into a rarefied, spatially extended target. This leads to the already mentioned 5-6% CE in the case of the 10-µm-wavelength CO_2-gas laser at the cost of a spatially extended EUV plasma (cf. next paragraph). Interestingly, a 2-µm-drive wavelength already shows potential for a significant improvement in CE compared to the 1-µm-wavelength case. To optimize the global efficiency in turning electrical power into usable EUV light, the 2-µm-wavelength seems most promising because of the availability of efficient solid-state laser technologies such as for example Tm:YAG and Ho:YAG both operating at 2-µm-wavelength. Alternatively, non-linear conversion via optical parametric amplification of 1 µm-wavelength radiation from the mature Yb:YAG laser, would be most efficient at the degeneracy wavelength at 2 µm, as elaborated on in the patented concept by Behnke [8]. It is yet unclear which laser system could provide the steep power demands (pulse energy and repetition rate) for an industrial EUV source.

In addition to offering a potential sweet spot of high obtainable CEs and available efficient solid-state laser technologies, 2-µm-drivers could enable smaller plasma sizes. The plasma size is of relevance since the etendue of the collector mirror limits the size of the EUV-emitting plasma that can be imaged onto the waver. The drive laser wavelength λ_{laser} determines the critical density $n_{\text{e,cr}} \propto \lambda_{\text{laser}}^{-2}$ of the plasma, beyond which the laser light cannot propagate. Since most of the laser energy is coupled into the region close to the *critical surface* (i.e., the surface where the critical density is reached), the critical density surface determines the size of the EUV emitting volume. Effectively, the drive-laser wavelength sets the achievable plasma EUV emitter density, through the associated critical density, and thus could enable smaller plasma sizes while preserving the total count of emitting ions contributing to useful EUV radiation. A 2 µm-wavelength-driven plasma could enable significantly smaller plasma sizes compared to current CO_2-gas laser-driven EUV sources. There is even a possibility of using only a *main-pulse*, which would reduce the complexity of the EUV source since a *pre-pulse* laser including its beamline would no longer be required.

The outlook of significantly improving the overall efficiency and performance of EUVL systems by transitioning to efficient and reliable 2-µm-wavelength solid-state lasers calls for an experimental campaign investigating the performance of 2-µm-driven EUV plasmas. In addition to the need to demonstrate high CE values, the scaling potential of the total in-band energy toward >10 mJ per pulse also needs to be shown to be able to rival existing CO_2-gas-laser-driven EUV sources. High in-band energies are required to eventually enable the 1000 W of usable EUV power in an EUVL system for enhanced productivity while remaining at manageable repetition rates. Solid-state lasers could potentially provide higher laser pulse energies than the CO_2-gas laser, enabling scaling of the overall power output without increasing the repetition rate. In order to convert more laser energy to usable in-band light, one could exploit several options: longer pulse durations further extending the duration of the plasma, bigger laser beam spot sizes on target, or simply using higher laser intensities. Each of these options needs to be thoroughly investigated, particularly in view of their impact on CE for promising solid-state laser wavelengths such as the 2-µm. Additionally, it is important to study the tin mass consumption to optimize the tin mass efficiency, thereby limiting debris generation, and enabling a sufficient supply of tin at high laser pulse energies. On the basis of these studies, one needs to advise a strategy and a target preparation scheme tailored to the laser beam characteristics to ultimately enable high in-band energies.

The aim of this Thesis is to experimentally investigate and understand plasmas, and learn what CE and which in-band energies can be achieved by irradiating tin targets with 2-µm-wavelength laser light. To do so, we built a 2-µm-wavelength system, based on the parametric conversion of 1-µm- into 2-µm-wavelength, and applied it in our investigations of EUV light generation. This laser system is not envisioned to be used in any industrial application since it runs at a low 10 Hz repetition rate, but it is valuable as a first plasma driver to characterize the EUV emission from 2-µm-wavelength driven tin plasmas. Our studies include a comparison of 1-µm- and 2-µm-driven plasmas to gain insight on how the expected reduction in optical depth affects the CE and obtainable overall in-band energy. This insight is valuable to characterize and understand the effects of different laser irradiation parameters (i.e., laser intensity, laser pulse duration, laser beam spot size, and intensity distribution) and tin target morphology. We systematically investigate how the in-band energy that could be used in EUVL scales with laser irradiation parameters and tin target size. The goal is to determine if the in-band energy could be scaled to energy levels relevant to the industry without impairing the CE. Showing high obtainable CEs from 2-µm-wavelength driven EUV plasma close to those from the CO_2-gas laser, at relevant in-band energies would be a critical first step towards demonstrating the feasibility to enhance the overall energy efficiency of EUV sources by using 2-µm solid-state-lasers.

Thesis outline and summary

Chapter 1 introduces a laser system that generates high-energy pulses at 2-µm wavelength with pulse widths tunable from 10–24 ns. This laser system comprises an optical parametric oscillator that generates mJ-level signal seed radiation and an optical parametric amplifier that boosts the output to 800 mJ of combined signal and idler when pumped with 2 J pulses of 1064-nm laser light. The system, operating with KTP crystals and running at a 10 Hz repetition rate, is characterized in the spatial, temporal, and spectral domains. The effect of saturation leads to an output pulse approaching flat-top spatial and box-shaped temporal profiles, as desired in the current application. The amplified pulses can be imaged down to sub-100 µm diameters (we make use of this in final Chapter 5), making this laser system a suitable driver for plasma sources of extreme ultraviolet (EUV) light.

In **Chapter 2**, a first comparative experimental study of laser-produced plasmas driven by 1-µm and 2-µm pulsed lasers is conducted, examining a wide range of intensities. Both lasers produce similar EUV spectra and plasma ionicities when the intensity ratio is kept constant at $I_{1\mu\text{m}}/I_{2\mu\text{m}} = 2.4(7)$. Crucially, the conversion efficiency (CE) of 2-µm-laser energy into radiation within a 2% bandwidth centered at 13.5 nm relevant for industrial applications is found to be a factor of two larger. Our findings regarding the scaling of the optimum laser intensity for efficient EUV generation and CE with drive laser wavelength are extended to other laser wavelengths using available literature data.

Chapter 3 presents experimental spectroscopic investigations of EUV light emitted from plasmas driven by 2-µm and 1-µm wavelength lasers, produced from spherical tin microdroplets, as a next step in investigating the applicability of the 2-µm for EUVL application. Under similar conditions and intensities, both lasers yield comparable spectra and plasma charge state distributions when maintaining a fixed intensity ratio. The findings, supported by simulations, indicate an inversely proportional scaling of the relevant plasma electron density and drive laser intensities with laser wavelength. The observed scaling extends to the optical depth in relation to droplet diameters and emission maximization for EUV lithography. This scaling also extends to the optical depth that is captured in the observed changes in EUV emission spectra over a wide range of droplet target diameters.

Chapter 4 investigates the EUV emission properties of tin plasmas driven by 2-µm wavelength laser pulses. A two-pulse scheme is now used, where a pre-pulse laser shapes tin microdroplets into thin disks, followed by the main pulse creating EUV-emitting plasma – modeled on the current state-of-the-art workings of EUV sources. The efficiency of creating EUV in-band light around 13.5 nm is found to depend on the geometrical overlap of laser light with the target. We show that the angular dependence of the in-band emission around the incoming laser beam (backward 2π hemisphere) is almost independent of the intensity and duration of the 2-µm drive laser. For direct comparison, a similar set of experiments is performed with a 1-µm-wavelength drive laser. Emission spectra show significant self-absorption of light around 13.5 nm in the 1-µm case, while in the 2-µm case only an opacity-related broadening of the spectral feature at 13.5 nm is observed. This difference in spectral emission demonstrates the enhanced capabilities and performance of 2-µm-driven plasmas produced from disk targets compared to 1-µm-driven plasmas.

Chapter 5 experimentally investigates the emission properties of tin plasmas in the EUV regime, using spatially flat-top and temporally box-shaped laser pulses imaged onto pre-deformed tin targets. Key performance indicators such as conversion efficiency (CE), spectral purity, and angular distribution of in-band EUV emission are examined. High CE values of up to 4.7%, outperforming plasma driven by lasers with Gaussian beam profiles of about 60% are achieved. The performance indicators' scaling with laser intensity, pulse duration, and spot diameter is also explored. We demonstrate promising in-band energy scaling capabilities with in-band energies beyond 10 mJ in a 2π sr solid angle, at high conversion efficiencies for 2-µm-driven plasmas, motivating its application in future high-power EUV sources.

In the **Conclusions**, we summarize the key learnings of this Thesis: We show how employing a solid-state laser with a 2-micron wavelength to power the EUV-emitting plasma could potentially enhance the overall energy efficiency of future EUV sources significantly, compared to the traditional CO_2-gas laser-driven EUV sources. This Thesis is completed with an outlook for future measurements, also at ARCNL, using high-energy 2-µm drive lasers.

CHAPTER 1

HIGH-ENERGY PARAMETRIC OSCILLATOR AND AMPLIFIER PULSED LIGHT SOURCE AT 2-μm

Lars Behnke, Edcel J. Salumbides, Guido Göritz, Yahia Mostafa, Dion Engels, Wim Ubachs, and Oscar Versolato

Optics Express **31**, 24142-24156 (2023).

A laser system generating high-energy pulses at 2-μm wavelength with pulse widths tunable from 10–24 ns is described. It comprises an optical parametric oscillator that generates mJ-level signal seed radiation and an optical parametric amplifier that boosts the output to 800 mJ of combined signal and idler when pumped with 2 J pulses of 1064-nm laser light. The system operated with KTP crystals and running at 10 Hz repetition rate is characterized in the spatial, temporal, and spectral domains. The effect of saturation leads to an output pulse approaching flat-top spatial and box-shaped temporal profiles, as desired in various applications. The amplified pulses can be imaged down to sub-100 μm diameters, making this laser system a suitable driver for plasma sources of extreme ultraviolet light.

1.1 Introduction

Mid-infrared (MIR) laser sources are of interest in various applications, including spectroscopy [9], laser ranging (LIDAR) [10], medical applications [11], material processing [12], and defense [12]. These applications require continuous-wave to ultrafast pulsed sources [13, 14]. High-energy laser sources of nanosecond pulses at 2–10 µm radiation are of particular interest for extreme ultraviolet (EUV) light generation in EUV lithography [15]. Here, pulses of several hundred mJ are imaged onto tin targets to create EUV emitting plasma. A full geometrical overlap of laser profile and target is crucial to obtain the highest conversion efficiencies of laser pulse energy to EUV radiation [16]. This case poses an example of an application requiring high pulse energies with good spatial and temporal beam characteristics.

Possible sources at 2-µm wavelength fulfilling the aforementioned criteria are Tm^{3+}/Ho^{3+}-doped solid-state and fiber lasers [13]. An example is the high-energy Big Aperture Thulium (BAT) laser system operating at 1.9 µm-wavelength [5, 6]. This laser has been demonstrated to provide an output of several 10 joules per pulse [17, 18], albeit at a low repetition rate.

Alternatively, optical parametric oscillators (OPOs) can be used to generate MIR laser light based on non-linear wave mixing. Nanosecond OPOs generating several hundred mJ/pulse have been built [19, 20], but combining high energy, high efficiency, and good beam quality remains a challenge [21]. Arisholm et al. [22] give an overview of the main challenges of combining high pulse energies in OPOs and good beam quality. High-energy OPO designs are limited by the achievable build-up time, which is the characteristic time required for amplifying the signal beam from quantum noise to significant pulse energies. The build-up time needs to be short compared to the duration of the pump pulse to obtain a high overall efficiency because only after the build-up time is efficient amplification of the signal beam possible. Since laser pulse durations of high-power pump lasers are usually in the order of nanoseconds, it is crucial to limit the build-up time to values well below that. This constraint limits possible resonator designs, particularly regarding the maximum resonator length, that would enable more transverse-mode control for beam quality enhancement. There are many approaches to enhance beam quality, such as unstable confocal resonators [23–27] and image-rotating resonator designs [21, 28, 29]. However, these approaches tend to increase the build-up time [22]. Lowering the transverse mode count in the resonator by reducing the pump beam diameter would lead (at constant energy) to exceeding the damage thresholds of the non-linear crystals and other optics, resulting in a trade-off between pulse energy and beam quality.

These limitations can be overcome by implementing a master oscillator and power amplifier (MOPA) architecture [22, 30, 31]. In such a configuration, an OPO acts as the master oscillator creating a seed beam at relatively low pulse energies with a reduced beam diameter, thus suppressing higher transversal modes. The OPO output beam is expanded and used to seed an optical parametric amplifier (OPA) boosting the output energy of the combined system. This design enables the generation of several hundred mJ pulse energy at high spatio-temporal beam quality because the OPA does not allow additional modes to grow.

The parametric MOPA introduced by Arisholm et al. delivered close to 300 mJ of total pulse energy (signal and idler combined) at a pulse duration of 6 ns [22]. With our present laser design, similarly based on KTP crystals, we demonstrate the generation of 2 µm-wavelength laser light with more than twice the pulse energy, and with variable pulse durations including temporal shaping. The quality of the output beam supports the demagnification of a flat-top spatial beam profile by a factor of 75, to below a spot diameter of 100 µm. We designed the MOPA for driving EUV-emitting laser-produced plasma (LPP), and successfully used it to demonstrate tin-plasmas driven by a 2-µm laser wavelength [15, 32, 33]. In this publication, we report on an extensive characterization of our high-energy 2-µm MOPA system.

1.2 Experimental setup

A schematic of the laser system is shown in Fig. 1.1. The upper panel shows the master oscillator power amplifier (MOPA), with an OPO stage whose output is used for seeding a 4-crystal OPA amplification stage. The lower panel shows light transportation and a high numerical aperture imaging system used to project the flat-top beam profile onto tin microdroplets in a vacuum chamber as part of a typical application in laser-produced, EUV-emitting plasmas at ARCNL. The two stages are indicated by their respective frames.

The MOPA configuration generates high pulse energies at 2-µm wavelengths with high beam quality following the design of Arisholm et al. [22]. An injection-seeded Nd:YAG laser (Amplitude Agilite, referred to as pump laser), emitting pulses at a wavelength of 1064 nm and repetition rate of 10 Hz, pumps the MOPA. This pump laser has advanced temporal pulse shaping capabilities, here allowing the laser pulse durations to be varied between 10 ns and 27 ns by means of a Pockels cell, such that the pump laser peak power remains constant. Accordingly, the attainable pulse energies scale with the set pulse duration ranging from 2.3 J at 27 ns to 0.9 J at 10 ns. The pump laser beam is split using a polarizing beam splitter to provide a small fraction (<80 mJ) for pumping the optical parametric oscillator, while most of the pump energy is delivered to the optical parametric amplification stage.

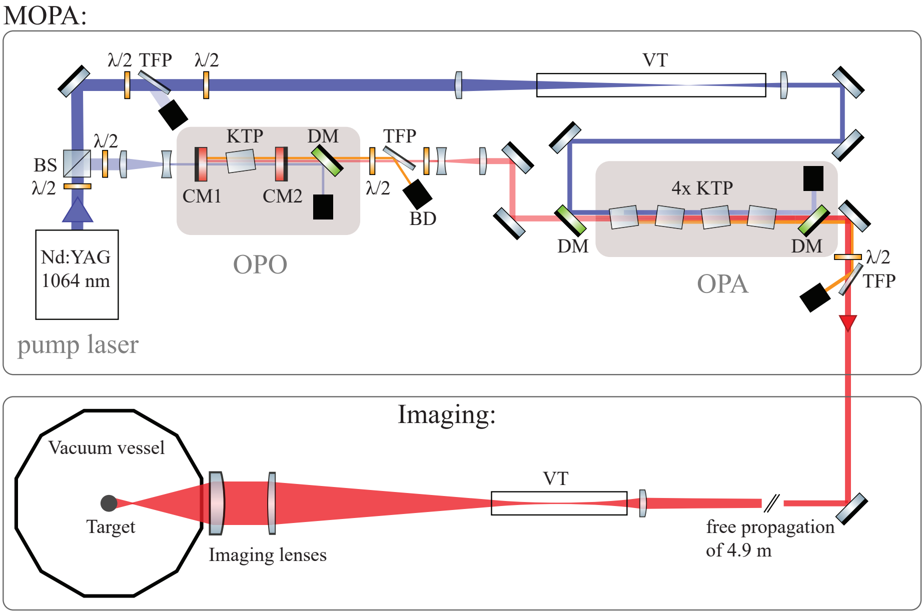

Figure 1.1: Schematic representation of the MOPA. The oscillator (OPO) and amplifier (OPA) are pumped by a Nd:YAG laser (pump laser) operating at 1064 nm wavelengths. The wavelengths generated are 2090 nm and 2167 nm. The flat-top beam profile of the MOPA output can be imaged onto a target with a 75-times reduction in size. ($\lambda/2$: half-wave plate, BS: polarizing beam splitter, TFP: thin-film polarizer, BD: beam dump, CM1 and CM2: cavity mirrors, DM: Dichroic mirror (reflection of 1064 nm, transmission of 2 µm wavelengths), KTP: Potassium titanyl phosphate (non-linear crystal for wave mixing), VT: vacuum tube).

Our OPO (a customized version of GWU versaScan-L 1064) has a 30-mm-length linear cavity comprised of flat dichroic resonator mirrors that are designed for single-pass pumping, so they are highly transmissive for the 1064-nm pump. The optical cavity resonates the signal wavelengths (i.e., wavelengths shorter than degeneracy at 2128 nm), and a fraction of the signal pulse energy being transmitted through the output coupler (CM2 in Fig. 1.1). The OPO contains a single KTP (potassium titanyl phosphate) crystal of 18.2 mm length and with an aperture of 15×13 mm^2. The crystal surfaces are anti-reflection coated for the 1064-nm pump wavelength and any wavelength generated in the range around 2 µm. A pump pulse energy of 76 mJ (at 27 ns) is used for pumping the OPO. The beam diameter is reduced with a Galilean-type telescope to 2 mm in front of the OPO resonator. This small beam diameter is chosen to improve the beam quality of the generated 2-µm laser light [22]. The crystal angle is tuned to an angle of θ =50.8° to achieve type II phase matching (oe-o) for a signal around 2090 nm and corresponding idler around 2167 nm wavelength. While the pump is linearly polarized vertically (defined as being perpendicular to the plane of Fig. 1.1), the signal has horizontal and the idler vertical polarization. The output pulse energy of the signal is 3 mJ with a pulse duration of 21 ns. A dichroic mirror is used to separate the unconverted 1064-nm pump transmitted through the cavity from 2-µm light that propagates further. The OPO output characteristics are discussed in section 1.3.

After the OPO, the signal beam is further separated from the idler by means of a polarizing filter. A Galilean-type telescope is used to magnify the beam diameter of the signal to approximately 5×2 mm^2 to seed the OPA at an intensity of 2 MW/cm^2. The OPA consists of four identical KTP crystals with a crystal length of 18.2 mm and an aperture of 15×13 mm^2 each. We use four crystals to obtain a pulse energy up to 800 mJ of combined signal and idler. Similarly to the OPO, the crystal surfaces have antireflective coatings for the pump wavelength and wavelengths in the 2-µm range. The crystal angle is tuned to θ =50.8° for type II phase matching (oe-o) to amplify the 2090 nm wavelength seed light. Here, the seed at the signal wavelength has horizontal polarization, and the pump is vertically polarized. For pumping the OPA, most of the 2.2 J (at 27 ns) of pump laser output is used. The beam is transported via relay imaging to ensure a flat-top spatial beam profile of the pump within the OPA. Additionally, the pump beam is optically delayed by 4 ns to account for the build-up time of the OPO. To achieve sufficient pump intensity within the OPA, its beam diameter is reduced from 12 mm to 6.5 mm, resulting in an intensity of approximately 220 MW/cm^2. The pump and seed beam are spatially overlapped using a dichroic mirror and aligned for propagation through the four crystals. The crystals are oriented for walk-off compensation (see Fig. 1.1). After the last crystal, the amplified 2-µm light and the remaining pump light are again separated by a dichroic mirror.

The MOPA is designed to drive LPPs at 2-µm wavelength. For this intended use, it is necessary to image and demagnify the flat-top beam profile onto a target as shown in the lower frame in Fig. 1.1. Flat-top imaged beams provide uniform heating of the LPP across the plasma surface at sufficiently high plasma temperatures, as was shown in the case of 1-µm wavelength-driven EUV emitting plasmas [16]. In this work, the output of the MOPA is imaged using a two-stage imaging setup. After a free propagation of about 4.9 m, the beam is imaged by a first spherical lens with a focal length of 400 mm (f400 mm). The intermediate image is reduced by about 11 times compared to the initial output beam diameter of the MOPA. After the intermediate image, the diverging beam is collimated with an f1000 mm lens. Subsequently, an f250 mm aspherical lens is used for imaging the beam onto a tin target. The total beam size reduction factor is up to 75 (chosen for a particular target size). Imaging the beam down to sub-100 µm diameters is possible due to a relatively low full beam divergence θ of approximately 2 mrad in the horizontal and 3 mrad in the vertical direction. Taking into account the waist diameter ω of the beam of approximately 5 mm, this leads to an M^2 value of $M_x^2 \approx 4$ along the horizontal axis and $M_y^2 \approx 6$ along the vertical axis following the

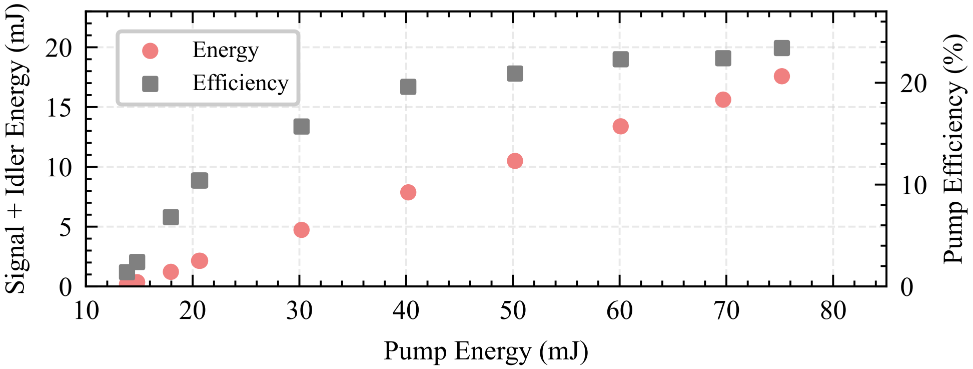

Figure 1.2: Combined signal and idler energies from the OPO as a function of the input pump energy (for a box-shaped pump pulse of duration $\tau_p = 27$ ns). The corresponding efficiency for conversion summed over both signal and idler is also indicated. Error bars are smaller than the markers.

relation $M^2 = \theta\pi\omega/(4\lambda)$ based on the beam parameter product with a wavelength of $\lambda = 2090$ nm. The characterization of the MOPA in terms of input and output energies, temporal beam profiles, and spatial profiles of the pump, signal, and idler beams are discussed in section 1.4.

1.3 Optical Parametric Oscillator

In this section, we discuss the characterization of the optical parametric oscillator including measurements on energy conversion, as well as recordings in the temporal domain. A representative graph in Fig. 1.2 shows the combined signal and idler OPO output energy as the input pump energy is varied. The conversion efficiency increases with pump energy, where pumping is limited below 80 mJ to avoid optical damage to cavity mirror coatings. Conversion to total output energies can reach efficiencies up to 24% (corresponding to a signal conversion efficiency of 12%) and shows a plateau indicating saturation at higher pumping energies. The pulse energy of the combined signal and idler, obtained for the highest pump energy of 76 mJ, is 17 mJ with a root-mean-square (RMS) stability of approximately 2% (for comparison, the pump RMS stability is 1%). For decreased input pump energies, the lower conversion efficiencies should in part be attributed to the long cavity build-up time of the signal (and idler).

Temporal profiles were recorded using fast photodiodes (EOT ET-5000, 12-GHz bandwidth) and a fast oscilloscope (Agilent Technologies DSO9404A, 4-GHz bandwidth), with a typical recording shown in Fig. 1.3. Dichroic mirrors and optical filters separate the signal beam from the idler and pump beams. At a pump energy of 76 mJ,

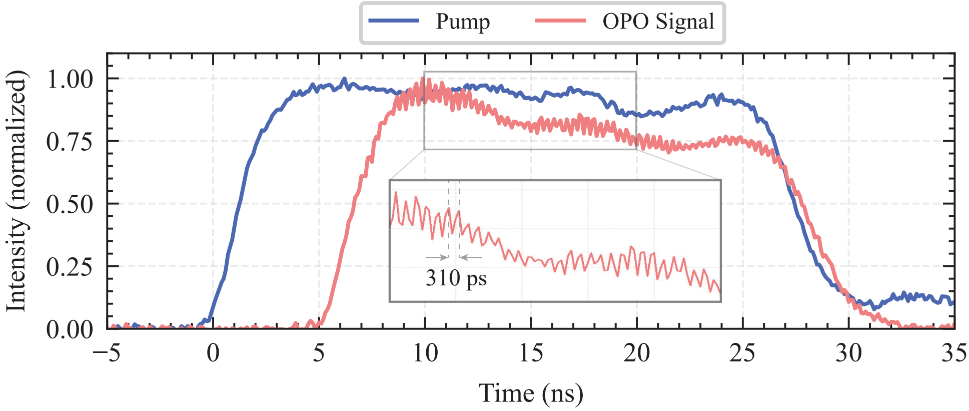

Figure 1.3: OPO oscilloscope traces for a 27 ns FWHM pump pulse duration at maximum OPO pump pulse energy. The temporal profiles of the initial pump beam (blue) and the generated signal beam (red) are shown for a pump energy of 76 mJ/pulse. The FWHM pulse duration of the signal is 21 ns revealing a build-up time of about 5.5 ns. The inset figure shows a magnified signal trace in the 10–20 ns interval highlighting the beating due to competing longitudinal modes. A beating period of 310 ps is measured, closely matching the cavity round time of 300 ps.

and pump pulse duration of $\tau_\mathrm{p} = 27$ ns, the signal resembles a box-shaped pulse with a full-width-at-half-maximum (FWHM) duration that is shorter ($\tau_\mathrm{s} = 21$ ns) than the pump. The build-up time τ_bu is defined as the delay between the onset of the signal and the pump pulse.

Cavity build-up times for the OPO signal were measured for varying pump input energies as shown in Fig. 1.4. For a pump pulse with duration $\tau_\mathrm{p} = 27$ ns, signal pulse durations of $\tau_\mathrm{s} = 5 - 21$ ns were observed for the pump energy range covered. In addition to decreasing the signal energies and longer build-up times, the signal temporal profiles are found to increasingly deviate from a box-shaped profile and tend towards a Gaussian profile at decreasing pump energies.

The cavity-build up time τ_bu behavior in Fig. 1.4 can be approximated following the relations from Refs. [22, 34], which can be expressed as:

$$\tau_\mathrm{bu} = \frac{\tau_\mathrm{cav}\; g_\mathrm{Log}}{\sqrt{E_\mathrm{p}/E_\mathrm{th}} - \epsilon}, \tag{1.1}$$

where τ_cav is the resonator roundtrip time, g_Log is related to photodetector sensitivity, ϵ contains information on the effective reflectivity and other optical losses and is of order unity, E_p is the input pump energy and E_th is a pump threshold energy directly related to the characteristic nonlinear threshold intensity I_th. The cavity roundtrip time is

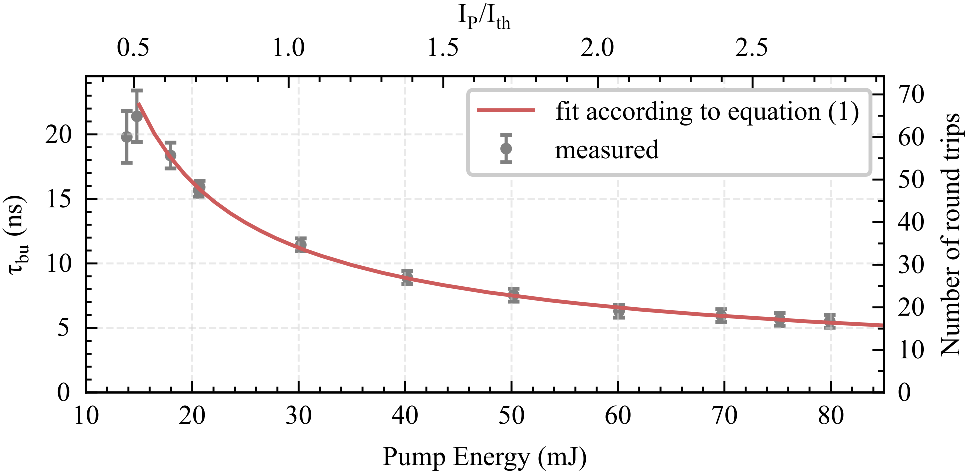

Figure 1.4: Measured OPO build-up times, τ_{bu}, of the signal output vs. pump energy input. The number of cavity round trips is also indicated given a round trip time $\tau_{cav} = 0.31$ ns. The red line represents a fit according to Eq. (1) for a value of the threshold pump energy $E_{th} = 29$ mJ. The alternate horizontal axis (top) indicates the normalized pump intensity I_p/I_{th} according to the intensity threshold I_{th} derived from the fitting procedure. Error bars are derived from shot-to-shot analysis.

estimated to be approximately 300 ps based on the KTP crystal length and cavity mirror separation. The fitted curve, displayed in Fig. 1.4, describes the experimental trend to sufficient accuracy. The fit yields $g_{Log} = 22$, which is close to $g_{Log} = \ln(I_{det}/I_{noise}) \approx 18$ that is the value commonly used in numerical studies [34, 35]. The extracted $\epsilon = 0.42$ is within the expected range and contains information on the effective reflectivity and other optical losses. For the $E_{th} = 29$ mJ obtained from the fit, the corresponding threshold intensity is $I_{th} = 36\,\mathrm{MW/cm^2}$, which is close to the characteristic irradiance of $I_{th,calc} = 38\,\mathrm{MW/cm^2}$ that we calculated from the definition given in Refs. [22, 36], for the signal and idler wavelengths and KTP crystal length. In Fig. 1.4, an alternate horizontal axis at the top is provided to indicate the normalized pump intensity I_p/I_{th} according to the intensity threshold I_{th} derived from the fitting procedure.

As expected, the OPO output is rather sensitive to the optical cavity alignment, as a result of interference between multiple cavity modes that can simultaneously be supported in an unstable resonator. The beating of these multiple modes can be observed from the oscilloscope traces for the OPO output as seen in the inset of Fig. 1.3. The measured beating period is 310 ps, which is close to the estimated cavity round trip time of 300 ps. Such beating dynamics has been anticipated in numerical studies [34, 37] but has not been experimentally shown in the temporal domain, to the best of our knowledge. The further slow oscillations at ~ 8 ns period visible in both pump and

OPO traces originate from the Agilite pump laser system.

Various measurements were performed to characterize and optimize the OPO for the highest output energies, optimal temporal profiles (considering build-up and temporal widths), and narrowest spectral widths (for mode stability, as discussed below). At these optimal conditions, the energy and beam pointing stability are also highest, providing an ideal starting point in seeding the MOPA amplification stage.

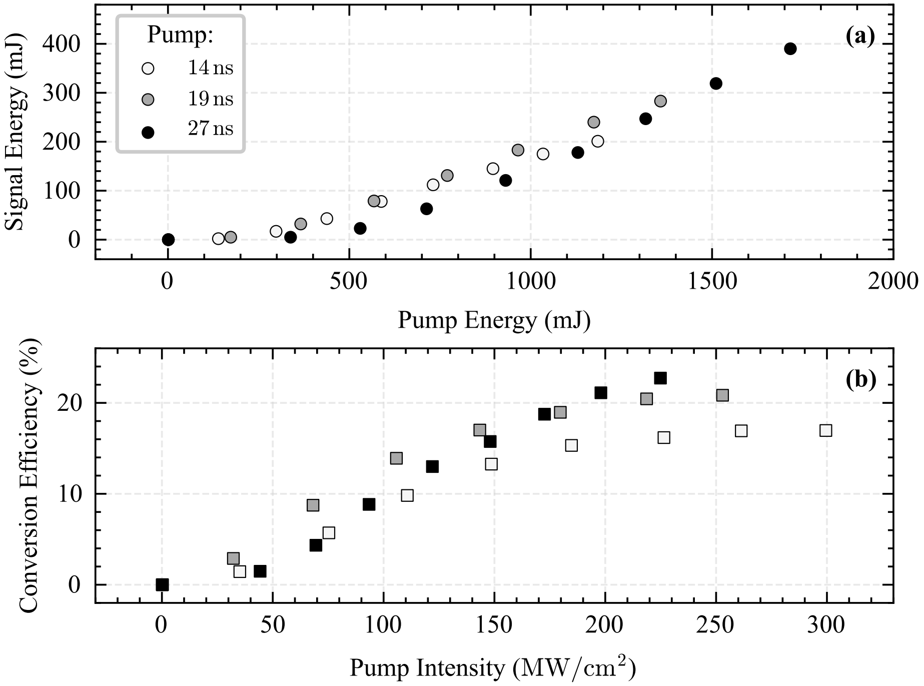

Figure 1.5: (a) MOPA output, plotted as pulse energies at the signal wavelength of 2090 nm, as obtained by varying pump energies at three different pump pulse durations. (b) Conversion efficiencies for different pump intensities, again for the three different pump pulse durations. The conversion efficiency is defined as signal energy divided by pump energy. Error bars are smaller than the markers.

1.4 Optical Parametric Amplifier

1.4.1 Output Energy

Fig. 1.5(a) shows a graph of signal energies vs. varying OPA-pump pulse energies for the three different set pulse durations of the pump laser: 14 ns, 19 ns, and 27 ns. The pulse durations are altered by changing the timing of a Pockels cell within the pump laser to crop the box-shaped laser pulse to the desired duration. Hence, the duration is changed without affecting the peak intensity and the overall shape of the laser pulse. To perform a scan of the pump pulse energy, a $\lambda/2$ wave-plate in combination with a thin-film polarizer is used. The intensity of the seed is kept constant at approximately $2\,\mathrm{MW/cm^2}$, meaning that the seed energy is fixed at 1.3 mJ in the 14 ns setting, at 2 mJ in the 19 ns setting, and at 3 mJ in the 27 ns setting.

For pump energies E_{pump} ranging from 0 to 1.7 J used in the 27 ns setting, up to 390 mJ of signal energy is achieved, thus yielding an amplification factor of 130. Since idler and signal energies are similar, the total energy is estimated at 780 mJ. The corresponding maximum pump intensity is 220 MW/cm^2, calculated via $I = E_{\text{pump}}/(\tau\pi w^2)$ with the pump laser pulse duration $\tau = 27$ ns and the laser beam radius w = FWHM/2 = 3.0 mm. Maximum pump intensities for the 19 ns and 14 ns settings are respectively 250 MW/cm^2 and 300 MW/cm^2, yielding signal (and, equivalently, idler) energies of up to 300 mJ and 200 mJ, respectively. Maximum pump intensities are limited by laser-induced damage thresholds of the antireflective coatings on the KTP crystal surfaces.

Fig. 1.5(b) displays the conversion efficiency of pump energy to signal or idler energy for the OPA for varying pump intensities for the three different set pulse durations 14 ns, 19 ns, and 27 ns. The trends for all pulse duration settings follow the same pattern. The conversion efficiencies at 14 ns (CE_{14ns}) and at 19 ns (CE_{19ns}) settings show a plateauing behavior starting at pump intensities of 180 MW/cm^2. Here, the term saturation refers to this leveling of conversion efficiency at high pump intensities. CE_{14ns} saturates at 17 % and CE_{19ns} saturates with 20 % at a somewhat higher efficiency. CE_{27ns} does not reveal such a distinct saturation behavior and it reaches a total conversion efficiency of 22 % for the highest pump intensity. These differences in saturation behavior might be explained by the varying temporal pulse shapes across the spatial profile of the pump beam (see section 1.4.3). This saturation of conversion efficiencies coincides with the transition of a non-linear increase of the signal/idler energies to a linear incline in Fig. 1.5(a), which is in line with the findings of Arisholm et al. [22]. The RMS deviation of the output energies at the highest pump intensity is 2.8% and increases to approximately 10% at the lowest pump intensities. This phenomenon may be ascribed to the effect of saturation.

It might be expected that higher output energies could be achieved by a further increase of the pump energy. However, for increased pump energies, laser-induced damage of the antireflective coatings on the KTP crystal surfaces is observed. Alternatively, more KTP crystals could be added to the OPA to enable operating at lower pump intensities. Additionally, dichroic mirrors could be used in between the KTP crystals of the OPA to reflect the idler beam out of the OPA. The latter would suppress nonlinear backconversion, although no direct evidence of such backconversion is observed. Filtering of the idler beam inside the OPA might be required, however, for increasing the efficiency at pump energies beyond 2 J, and for future power gains of high-energy pulsed KTP-based MOPA systems [22].

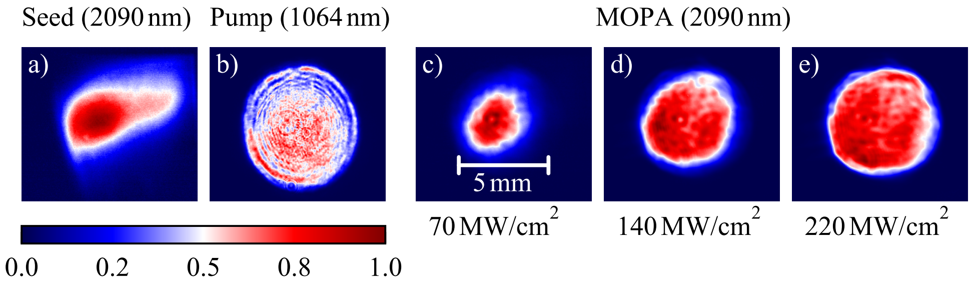

Figure 1.6: Selection of beam profiles as imaged from a defined plane inside the OPA stage for the 27 ns pump pulse duration setting: (a) seed (signal) beam generated by the OPO with an FWHM of 5.3 × 2.3 mm^2. (b) flat-top pump beam profile with an FWHM of 6 mm. (c)-(e) show the amplified seed beam that is the output of the MOPA system, for different pump intensities. The flat-top beam profile generated at the highest pump intensity in panel (e) has an FWHM of 4.5 × 5.1 mm^2, and 85% of its total energy is enclosed within the FWHM contour. The OPO is for all cases pumped with a pump energy of 76 mJ at 27 ns pump-pulse duration.

1.4.2 Spatial profiles

Fig. 1.6 shows normalized spatial profiles of the seed beam, pump beam, and the signal beam generated by the MOPA at different pump intensities. The profiles at 2-μm wavelength are recorded using a pyroelectric camera (Ophir PyroCam IV), located at a fixed position approximately 3 m after the OPA. Using a single spherical lens, with a focal length of 600 mm, seed and MOPA beam profiles are imaged onto the chip of the pyroelectric camera with a magnification of 2.6×. The pump beam profile is taken using a silicon-based CCD camera (Ophir SP920) at a fixed position approximately 2 m after the OPA stage. Here, a spherical lens with a focal length of 300 mm is used to image the beam profile on the camera chip with a demagnification of 0.5×. All profiles in Fig. 1.6 share the same scaling factor and spatial coordinate grid to facilitate direct comparison.

Fig. 1.6(a) shows the profile of the seed beam at 2090 nm, as it is transported from the OPO to the second crystal within the OPA, 300 mm after the OPO and twofold expanded, without relay imaging. The seed beam has an asymmetric shape, significantly different from that of the pump beam profile. This asymmetry may be caused by walk-off and by the multiple modes supported by the OPO cavity. Fig. 1.6(b) shows the beam profile of the pump within the OPA for a set pulse duration of 27 ns. It resembles a flat-top beam distribution, with slight asymmetries characteristic to the pump-laser used. The fringes originate from the aperturing in the commercial Agilite laser system. The lower resolution of the pyroelectric camera is expected to significantly reduce the visibility of fringes in the signal beams (see below). Fig. 1.6(c–e) shows the signal beam of the MOPA for pump beam intensities of 70 MW/cm^2, 140 MW/cm^2, and 220 MW/cm^2.

The diameter of the MOPA beam profile increases from $1.7 \times 2.6\,\mathrm{mm}^2$ to $4.5 \times 5.1\,\mathrm{mm}^2$ with increasing pump intensity. At the lowest pump intensity, the MOPA profile deviates mostly from a flat-top beam profile, following the seed beam profile. For increasing pump intensity, the MOPA beam profile gradually approaches a flat-top beam profile following the pump beam profile. The percentage of the energy enclosed inside the FWHM contour of the MOPA beam profile increases from approximately 50% to 85% at the highest pump intensity. Ring-like structures in the outer regime of the MOPA beam profiles become apparent, following similar features of the pump beam profile. The spatial flattening is explained by the fact that the local seed and pump intensities vary across the spatial overlap of the beam profiles. Consequently, the local parametric gain of the OPA depends on the position in the beam profile. In the center of the beam, the local gain is higher than at the edges, due to the peaking seed intensity at the beam center. This non-uniformity in the local gain affects the local conversion efficiency, which is the efficiency of converting pump energy to signal energy contained within a certain area of the beam profile. Consequently, the local conversion efficiency first saturates at the center. This leads to a flattening of the beam for increasing pump intensities when the outer areas of the beam profile catch up in local intensity and approach saturation at higher overall pump intensities. The MOPA beam profiles do not show definitive signs of backconversion such as local depletion in MOPA intensity caused by converting 2-µm light back to 1-µm light.

1.4.3 Temporal profiles

Figure 1.7 shows various characteristic temporal pulse profiles of the MOPA for a setting of the pump pulse to a box-shaped profile of 27 ns duration. The temporal pulse profiles of the pump beam before and after depletion in the OPA stage, the seed beam, and the amplified 2-µm wavelength after the MOPA (referred to as MOPA pulse) are displayed for three different pump intensities, being $220\,\mathrm{MW/cm}^2$, $140\,\mathrm{MW/cm}^2$ and $70\,\mathrm{MW/cm}^2$. For an interpretation of the time axis, some synchronization technicalities should be considered. The pump pulse is optically delayed by approximately 4 ns before entering the OPA stage (see section 1.2) resulting in a delay of about 1 ns between the onsets of the pump pulse and the seed and MOPA pulses. By delaying the pump pulse, the seed pulse becomes centered with respect to the pump pulse inside the OPA stage. This also causes the low-intensity parts of the seed pulse to experience maximum pump intensity, leading to a longer effective pulse duration (see Fig. 1.9).

The central result of these studies on temporal profiles is that a MOPA pulse can be generated exhibiting a box-shaped profile of 24 ns, as shown in panel (a). Such a pattern can be achieved for a pump pulse of the highest intensity, at $220\,\mathrm{MW/cm}^2$, that

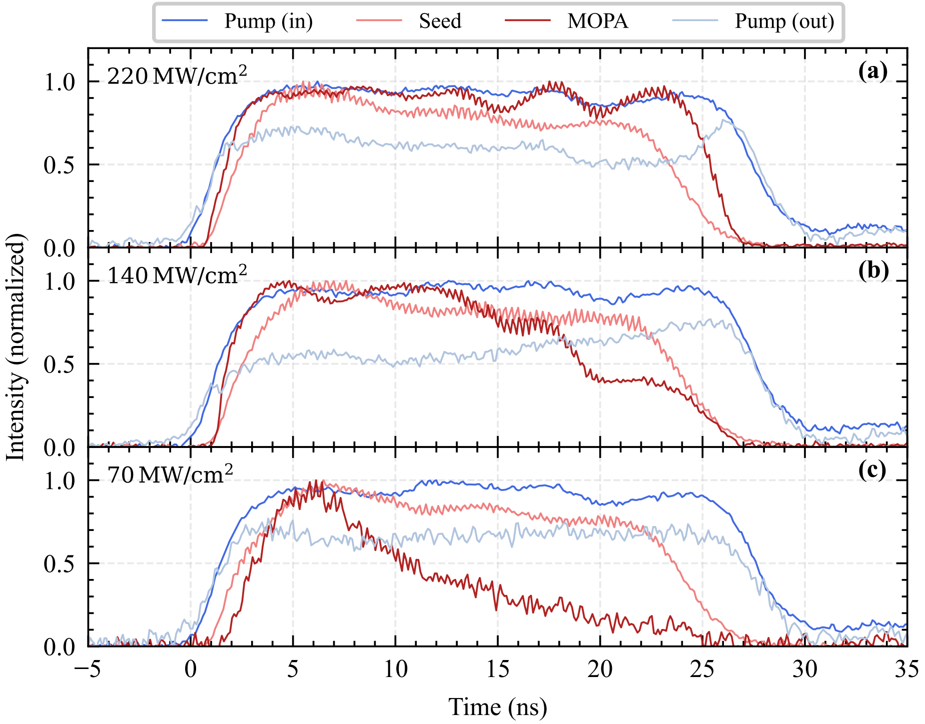

Figure 1.7: (a)-(c) Temporal pulse profiles for a 27 ns pump pulse duration setting for pump intensities as specified in panels. The pulses of the initial pump, the seed, the MOPA output, and the depleted pump after amplification are presented. All but the depleted pump profile are normalized. The pulse profile of the depleted pump is scaled so that the integral matches the percentage of the remaining pump energy to visualize the effect of pump depletion. The light detected beyond 30 ns is assumed to originate from light leakage at the Pockels cells controlling the duration of the pump pulse.

is also box-shaped. The box-shaped profile of the MOPA pulse is overlaid with a high-frequency oscillation, resulting from the longitudinal mode-beating pattern originating from the OPO seed (see Fig. 1.3). We note that the intensity at the beginning and end of the MOPA pulse inclines and declines more steeply than the intensity of the seed pulse. This behavior can be explained by a strongly non-linear, parametric amplification at lower seed intensities, whereas amplification is less strong at higher seed intensities due to saturation. The MOPA pulse increasingly deviates from the box shape of the pump pulse when moving to lower pump intensities, eventually becoming triangular in shape at the lowest intensities of 70 MW/cm^2. The measured pump profile after the OPA shows depletion of its energy in the form of a dip in the local pulse intensity at times coinciding with the MOPA pulse.

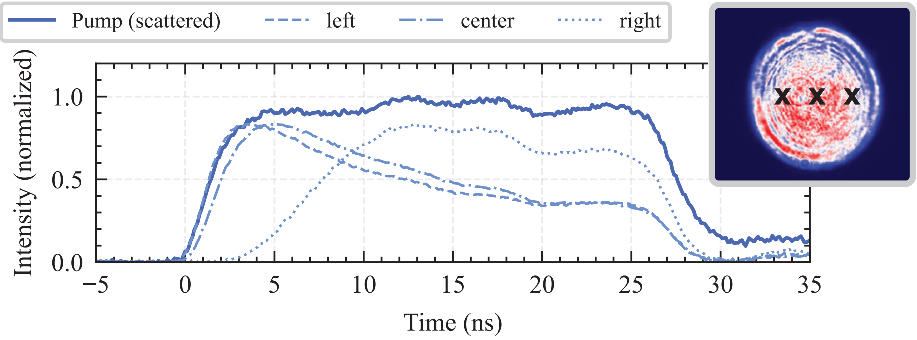

Figure 1.8: Temporal profile of the pump pulse resolved across the spatial beam profile. The blue solid line shows the temporal trace of the scattered light, i.e. representative of the full beam. The dashed/dotted lines show traces recorded with a 200 µm pinhole mounted in front of a photodiode to obtain spatially resolved traces at left, center, and right locations as indicated in the inset figure.

In order to explain the temporal deformation of the MOPA pulse at lower pump intensities, the intensity of the incoming pump pulse is spatially probed using a photodiode equipped with a 200 µm pinhole in front. Results of this local probing are presented in Fig. 1.8, showing that the temporal shape of the pump pulse is triangular at the center and left-hand side of the beam. In contrast, on the right-hand side, it shows a slow increase followed by a plateau region. This behavior may be explained by considering that for the lowest pump intensities, the center of the seed spatial beam profile, where the intensity is highest, undergoes the strongest parametric amplification [cf. Fig. 1.6(a) and (c)]. So, only the part of the pump beam profile spatially overlapping with the center of the seed beam profile contributes significantly to the parametric amplification at lower pump intensities. As a result, the temporal MOPA pulse profile follows the pump pulse profile at the position of the peak of the seed beam profile; the shape is more triangular-like [cf. Fig. 1.8 and Fig. 1.7 (c)]. When the overall pump intensity increases, gradually more parts of the pump beam profile, overlapping with low-intensity areas of the seed beam profile, contribute to the parametric amplification, while the part with the highest seed intensity starts saturating in local conversion efficiency (as discussed in section 1.4.2). When summing up these spatially dependent temporal pulse profiles, the overall MOPA pulse will resemble the overall temporal shape of the pump pulse, forming a superposition of local, different, pulse shapes. Currently it is unclear if spatio-temporal coupling (STC) of the pump is translated onto any signal STC, nor is there a model available to predict the impact of STC on the generation of EUV-emitting plasma. Further study is required to clarify these new topics, enabled by the laser system presented in this work. Fig. 1.9 shows temporal traces of the incoming pump pulse,

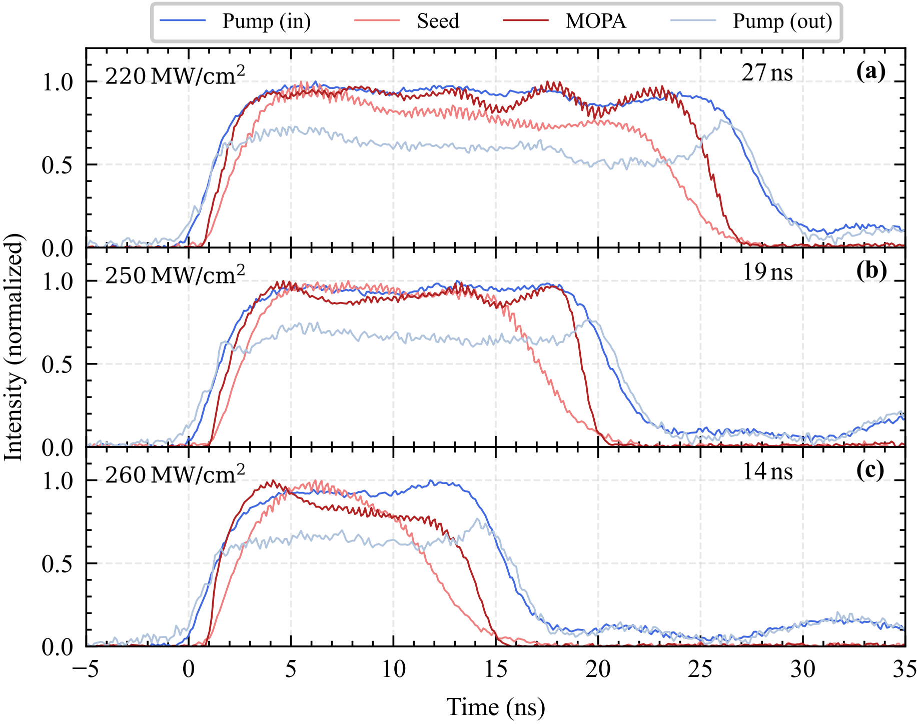

Figure 1.9: Measured temporal profiles of the initial pump beam, the OPO-seed beam, and the MOPA signal beam, and the depleted pump are shown for settings of the pump pulse for combinations of duration and intensity as specified in the legends.

the seed, the MOPA, and of the depleted pump, measured for different combinations of durations and intensities of the pump pulse: 27 ns and 220 MW/cm^2, 19 ns and 250 MW/cm^2, and 14 ns and 260 MW/cm^2, respectively. The resulting durations of the MOPA pulses under these conditions are 24, 17, and 12 ns, respectively. At the high pump intensities, all exceeding 220 MW/cm^2, the temporal box-shaped pulses of the pump could be converted into box-shaped MOPA pulses. Interestingly, the difference between the durations of the pump pulses and the corresponding MOPA pulses is only 2–3 ns, whereas the difference between OPO-seed and pump pulse duration, i.e. the build-up time, is 5.5 ns (see Fig. 1.3). This phenomenon is attributed to the amplification of low-intensity parts on the side flanks of the seed pulse.

In conclusion, it is demonstrated that box-shaped temporal profiles of the MOPA pulses can be produced in a controlled fashion for varying pulse durations between 12 and 24 ns.

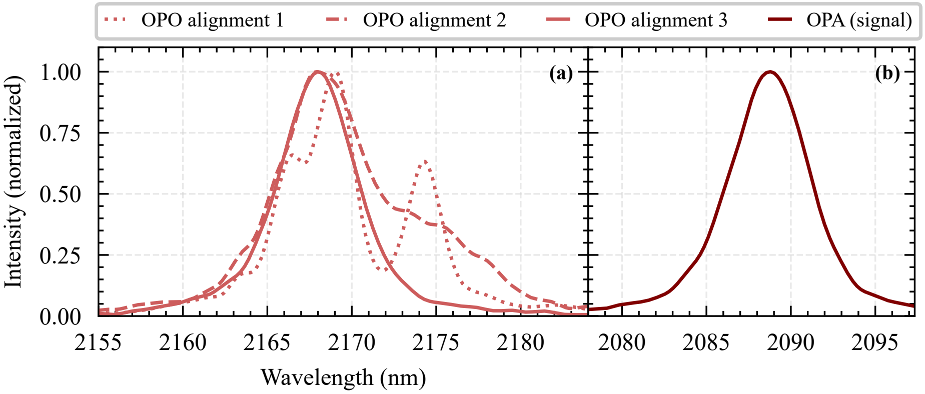

Figure 1.10: (a) Spectral analysis of the OPO idler output wave for three different cavity alignment conditions. (b) Spectrum of the signal beam of the OPO alignment 3 in (a) after amplification in the MOPA stage.

1.5 Spectrum and bandwidth

In this section, we discuss spectral measurements for the OPO output as well as the amplified MOPA output (for $\tau_p = 27$ ns) recorded using a High-Finesse WS5 IR-III wavelength meter. Fig. 1.10(a) shows OPO idler output spectra for different cavity alignment settings. The OPO idler wave, which has an orthogonal polarization to that of the signal wave, is separated by reflection from a thin film polarizer and is used for online monitoring, while the OPO signal wave output is transported towards the MOPA to seed the amplifier. At OPO cavity alignment-1, far from the output energy optimum, multiple spectral modes can be observed, which we attribute to multiple cavity modes simultaneously supported by the unstable resonator.

The spectral FWHM width of each mode is 2.6 nm while the crystal acceptance bandwidth for OPO operation is estimated to be 4.7 nm from the nonlinear optics code SNLO [38]. (The instrument limit of the spectrometer is not exactly known at this wavelength, thus our measurement provides an upper limit.) The narrower linewidth for the observed individual modes may be due to gain narrowing effects, where nanosecond OPO linewidths can be as narrow as 20% of the crystal phase matching bandwidth [36]. The mode separation of 3 nm can be used to estimate the angular deviation of 0.8 mrad for neighboring cavity mode paths, which is easily supported considering the pump beam size and cavity length. As the cavity alignment is optimized towards higher output energy, the spectral profile becomes more uniform with fewer spectral modes (alignments-2 and -3), suggesting that the optimal alignment condition favors higher gains for a smaller number of modes. For optimum alignment conditions (OPO alignment-3), the highest OPO output energy and narrowest composite spectral width are obtained, which also correlate with the highest energy- and spatial-beam profile stability.

In Fig. 1.10(b), the amplified signal wave spectra corresponding to OPO alignment-3 in Fig. 1.10(a) is shown. The OPA spectrum is taken when the amplifier is pumped with 1.7 J for a pump pulse duration of $\tau_p = 27$ ns, corresponding to an intensity of 220 $\mathrm{MW/cm^2}$. The FWHM width of the OPO alignment-3 spectrum in Fig. 1.10(a) is 5.0 nm, while the MOPA output FWHM width is marginally broader at 5.5 nm. The latter can be compared to the crystal phase-matching bandwidth for signal wave amplification in a single pass of 6.5 nm estimated using the SNLO code [38]. The SNLO code gives an OPO bandwidth that is narrower than the single-pass mixing bandwidth, with the same input parameters. It assumes that the signal and idler tune in equal amounts with respect to the fixed pump, hence it is the group velocity dispersion between signal and idler that is relevant. For amplification in the OPA, it is the dispersion of the group velocity between the seed (signal) and the pump that limits the phase matching. Note that for these spectral recordings, the OPO seed energy is about 1 mJ while the MOPA amplified output energy is around 400 mJ. The OPO and OPA spectral profiles demonstrate that even at high energy operation, the amplification process closely maintains the uniform and symmetric spectral characteristic of the seed radiation.

1.6 Conclusion

We built a parametric master oscillator power amplifier (MOPA) with an optical parametric oscillator (OPO) generating 2-µm wavelength light that is amplified by an optical parametric amplifier (OPA). This configuration allows for the generation of high-energy nanosecond pulses with a relatively good beam quality of $\mathrm{M}^2 \approx 5$. The MOPA is pumped by a seeded 1064-nm Nd:YAG laser that has temporal pulse shaping capabilities. The MOPA can generate box-shaped temporal pulses with a tunable pulse duration from 10–24 ns. We demonstrate a total pulse energy of 800 mJ, signal and idler combined, from 2 J of pump energy input when using four KTP-crystals in the amplifier.

The total conversion efficiency of 1-µm to 2-µm wavelength light, combining signal and idler, saturates close to 44%. Close to the saturation level, the spatial beam profile of the MOPA follows the flat-top shape of the pump beam. We find a similar behavior in the temporal domain, where the output pulse approaches a box-shaped temporal profile comparable to the input pump pulse for increasing pump intensities. The flat-top spatial and box-shaped temporal profiles are realized due to saturation effects of the conversion efficiency in the OPA stage.

Even at the highest output energies, the beam divergence is sufficient for imaging the beam to a highly intense flat-top profile below 100 µm diameter. Certain EUV plasma studies require highly energetic pulsed laser radiation to irradiate a sub-100 µm micro-droplet tin target with high intensities. Those high pulse energies are not only restricted to 2-µm wavelength since the output wavelength of a MOPA can in principle be tuned in a range from 1.4–3 µm by changing the phase-matching angle of the KTP crystals. Hence, our MOPA is an ideal laser source for EUV plasma studies and applications that require high pulse energies at good beam qualities in the mid-infrared range.

1.7 Acknowledgments

This work has been carried out at the Advanced Research Center for Nanolithography (ARCNL). ARCNL is a public-private partnership with founding partners UvA, VU, NWO-I and ASML, and associate partner RUG.

CHAPTER 2

EXTREME ULTRAVIOLET LIGHT FROM A TIN PLASMA DRIVEN BY A 2-μm-WAVELENGTH LASER

L. Behnke, R. Schupp, Z. Bouza, M. Bayraktar, Z. Mazzotta, R. Meijer, J. Sheil, S. Witte, W. Ubachs, R. Hoekstra, and O. O. Versolato

Optics Express **29**, 4475-4487 (2021).

An experimental study of laser-produced plasmas is performed by irradiating a planar tin target by laser pulses, of 4.8 ns duration, produced from a KTP-based 2-μm-wavelength master oscillator power amplifier. Comparative spectroscopic investigations are performed for plasmas driven by 1-μm- and 2-μm-wavelength pulsed lasers, over a wide range of laser intensities spanning 0.5–5 $\times$ 10^{11} W/cm^2. Similar extreme ultraviolet (EUV) spectra in the 5.5–25.5 nm wavelength range and underlying plasma ionicities are obtained when the intensity ratio is kept fixed at $I_{1\mu m}/I_{2\mu m}$ = 2.4(7). Crucially, the conversion efficiency (CE) of 2-μm-laser energy into radiation within a 2% bandwidth centered at 13.5 nm relevant for industrial applications is found to be a factor of two larger, at a 60 degree observation angle, than in the case of the denser 1-μm-laser-driven plasma. Our findings regarding the scaling of the optimum laser intensity for efficient EUV generation and CE with drive laser wavelength are extended to other laser wavelengths using available literature data.

2.1 Introduction

Extreme-ultraviolet (EUV) lithography has successfully entered high-volume manufacturing, enabling the continued miniaturization of semiconductor devices. The required EUV light is generated from mass-limited tin-microdroplet laser-produced plasma (LPP) [39–43]. Multiply charged tin plasma ions are the atomic sources of EUV radiation near 13.5 nm wavelength [43–50]. Currently, CO_2-gas lasers operating at $\lambda = 10.6\,\mu\mathrm{m}$ wavelength are used to drive the EUV-emitting plasma at a high conversion efficiency (CE) of laser energy into 'in-band' radiation, i.e. in a 2% wavelength bandwidth centered at 13.5 nm emitted into the half-sphere back towards the laser that is relevant for state-of-the-art EUV lithography. Solid-state lasers, operating at near- or mid-infrared wavelengths, may however become a viable alternative in the future. Such laser systems would potentially provide a smaller footprint, a significantly higher efficiency in converting electrical power to laser light, and may be scaled to much higher pulse energies and output powers which will enable even more powerful EUV light sources. However, the shorter drive laser wavelength of, e.g., the well-known Nd:YAG laser (1064 nm) is associated with large optical depths of EUV emitting plasmas[39]. Large optical depths may strongly limit the efficiency of such Nd:YAG-driven sources as opacity effects broaden the EUV spectrum well beyond the 2% wavelength acceptance bandwidth, thus reducing the spectral purity (SP) of the EUV plasma source [16, 51–57]. SP is defined here as the ratio of in-band EUV energy to the total energy emitted in the 5.5–25.5 nm range. Simulation efforts indicate that a global optimum of the efficiency of converting drive laser light into useful EUV radiation lies in between the well-known 1- and 10-µm cases[58]. In this range, thulium lasers, operating at 1.9-µm wavelength, appear promising[6]. The simulation efforts have produced predictions of CEs ranging from 1.2 times the CE of 1-µm-driven plasmas up to the much higher CEs achieved by 10-µm-driven plasmas (see below), depending on precise plasma conditions, when using such thulium lasers[58, 59]. However, no experimental studies of plasmas driven by lasers in the 1- and 10-µm range, under conditions relevant for EUV emission, are yet available.

The current search for an optimum laser wavelength between 1 and 10 µm for driving EUV emitting plasma can be put in a broader context. Nishihara et al. [60] produced an overview of the key physics issues for optimizing EUV sources also with respect to drive laser wavelength. They furthermore provided simulation results using a power balance model for optimal drive laser intensities with predictions for obtainable CE, shown in Fig. 2.1, for an ideal case of plasma of single optimal density and temperature. In Fig. 2.1, the obtainable CE is shown to rise with drive laser wavelength from ~1% for the shortest wavelength, to ~6% for the longest one. The optimum laser intensity decreases with increasing laser wavelength. Several other groups performed simulations to establish optimal conditions for EUV production from plasma. For example, White et al. [57] computationally studied the impact of laser wavelength and power density in a comparison of Nd:YAG (at its fundamental wavelength and its third harmonic) and CO_2 lasers. Their results strongly favor the latter drive laser for reaching the highest CE values. Achieving optimum plasma conditions for efficient in-band EUV emission at sufficient brightness under non-idealized conditions involves trade-offs, maintaining sufficiently high optical depth for in-band transitions and limiting optical depth for weaker out-of-band transitions [61, 62].

The conclusions from Nihishara et al. [60] are by and large supported by experiment. In the following, we present a brief literature review of experimentally obtained CE values and optimum laser intensities. The values reported are for planar solid pure-tin targets unless specified otherwise. The findings are summarized in Fig. 2.1. Starting at the shortest drive laser wavelength, Shevelko et al. [63] recorded a peak CE into a 1% bandwidth at 13.5 nm of 0.31% with a KrF laser pulse at 248 nm wavelength at a power density of 1×10^{12} W/cm^2. Kauffman et al. [64] achieved a CE of ∼1% (as reported by Hayden et al. [56]) using frequency-doubled Nd:YAG pulses at 532 nm. They observed that the CE was highly sensitive to the incident laser pulse intensity, to peak at $2{\times}10^{11}$ W/cm^2. Hayden et al. [56] demonstrated 2.2% CE using a pulsed Nd:YAG laser operating at its fundamental 1064 nm wavelength and an intensity of 2×10^{11} W/cm^2. Their findings are in line with those of Harilal et al. [65] who found a 2% CE value at 4×10^{11} W/cm^2 using the same drive wavelength. Tao et al. [66] studied the influence of focal spot size on in-band emission from Nd:YAG laser-produced Sn plasmas finding almost constant in-band conversion efficiency (at a ∼2% value, consistent with Coons et al. [67]) of focal spot sizes of 60 to 500 µm thereby contrasting the findings of Spitzer et al. [68] (also see Sec. 2.3 below). In this work we find (see Sec. 2.3) optimal SP and CE values at a Nd:YAG laser intensity of 3×10^{11} W/cm^2. Other studies (see Campos et al. [69] and references therein) showed that the optimum laser pulse parameters for obtaining the highest CE for CO_2 and Nd:YAG laser pulses are 6×10^9 W/cm^2 and 6×10^{10} W/cm^2, respectively. A much larger ∼5% CE value was reported by George et al. [70] at an intensity close to 1×10^{11} W/cm^2. For droplet pure-tin targets, CEs can be found with values ranging from 1.4% as reported by Giovannini et al. [71] to ∼3% reported in Schupp et al. [16] both at a Nd:YAG laser intensity of 2×10^{11} W/cm^2 but using different plasma recipes. A similar 3% CE was obtained by Shimada et al. [72] from spherical solid tin targets that were illuminated uniformly with twelve beams from the 1.05 µm-wavelength Gekko XII laser system.

Moving towards longer wavelengths, Tanaka et al. [55] estimated the maximum conversion efficiency for both CO_2 and Nd:YAG laser driven plasma to be 2% alike. Their work indicated an optimum drive laser intensity of 10^{10} W/cm^2 for the CO_2 driver and several 10^{10} W/cm^2 for the Nd:YAG driver. Using a CO_2 driver, Harilal et al. [73] found CEs approaching 4% when optimizing the focal spot size at a constant 6×10^9 W/cm^2 intensity (also see their more recent work [53]). Ueno et al. [74] found a similar value of 4% using a cavity target. More recently, a maximum CE of 5.8% was found by Amano et al. [75] using a CO_2 laser intensity of 5×10^{10} W/cm^2 and a relatively short 5 ns pulse duration. Using a CO_2 driver and droplet pure-tin targets, CE values of ~5% were reported by the company Gigaphoton by Mizoguchi et al. [76] and ~6% by ASML company as presented by Fomenkov et al. [77]. These high CE values were obtained using multiple laser pulses that shape the liquid droplet target for optimal interaction with the CO_2 main pulse beam. Conclusions could also be drawn from obtained relative CE values where no absolute information is available. For example, Yamaura et al. [78] characterized EUV emission for 266 and 1064 nm drive laser wavelengths finding that the EUV emission exhibits a laser-wavelength dependence in terms of angular distribution. Pronounced absorption dips appear in the EUV emission spectra in the case of the short-wavelength driver, indicating a reduced spectral purity which may lead to a lower obtainable CE. Freeman et al. [52] (also see the related work of Campos et al. [69]) showed highest in-band emission and spectral purity from the longest wavelength drive laser when comparing 1064, 532, and 266 nm wavelength experiments.

In this work we present a study of the EUV emission spectrum of a 2-µm-wavelength-LPP generated from a planar tin target, entering the territory of wavelengths in between 1 and 10 µm. We find highest SP and CE at 1×10^{11} W/cm^2. In a complementary study [32] our team finds that a similar intensity of 8×10^{10} W/cm^2 optimizes SP for pure-tin droplet targets using 2 µm wavelength drive laser light. Those droplet-target experiments however produced insignificant CE due to the poor geometrical overlap of laser pulse and target. This drawback is absent in the current work where complete laser-target overlap is guaranteed and relevant CE values can be obtained. Our current studies are not intended to maximize CE but rather to provide a meaningful comparison of 1- to 2-µm drive laser cases. The 2-µm laser light in this work is obtained from a master oscillator power amplifier (MOPA) based on a series of KTP crystals pumped by a Nd:YAG laser. This setup enables assessing the potential of thulium lasers without the expense of developing and building one. The obtained EUV spectra and CEs are compared to those obtained from Nd:YAG-LPP under otherwise very similar conditions.

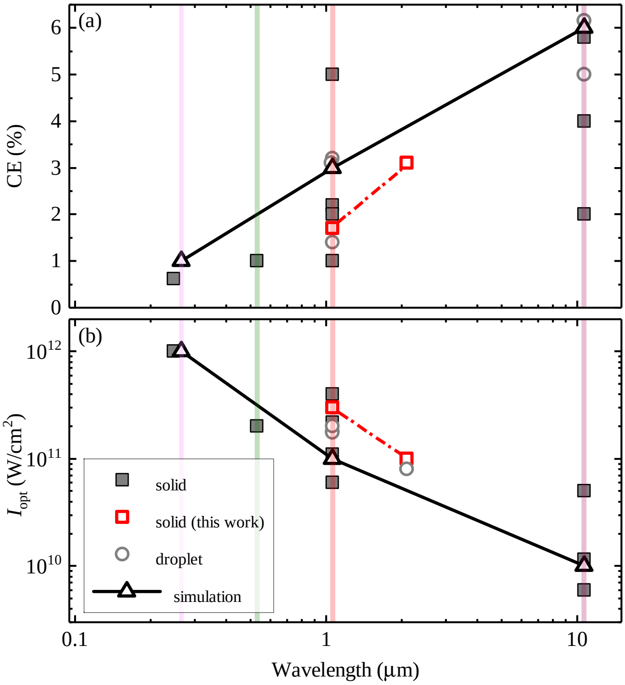

Figure 2.1: (a) Conversion efficiency (CE) and (b) optimum laser intensity (I_{opt}) values as a function of drive laser wavelength, as obtained from previous experiments on planar solid (full gray squares) and droplet (open gray circles) tin targets (data from Refs. [16, 32, 52, 53, 55, 56, 63–67, 69, 70, 72–78], see main text). Overlapping data points are shifted vertically for visibility. Simulation results [60] for plasma under optimal conditions are shown (open black triangles) connected by straight lines. The vertical lines, from right to left, indicate the wavelength of the CO_2 laser and that of the Nd:YAG laser and its second and fourth harmonics. The results of the current work are shown as open red squares. See main text for further details.

2.2 Experimental setup

In this work we present an experimental study of an LPP generated by illuminating a planar solid tin target of 99.995% purity with pulsed lasers having wavelengths of 1 µm and 2 µm. The target is mounted on a two-axis translation stage inside a vacuum chamber pumped to 1×10^{-6} mbar. The target is moved after two laser shots per position to prevent crater formation influencing the EUV emission. Spectral emission in the 5–25 nm range is recorded by means of a transmission grating spectrometer positioned at 60 degrees with respect to the incoming laser (see Fig. 2.2). The spectrometer is operated with a slit width of 25 µm and a 10 000 lines/mm grating. The dispersed light is collected on a back-illuminated charge-coupled device. The dispersive axis is calibrated using reference spectra comprising well-known Al^{3+} and Al^{4+} line features

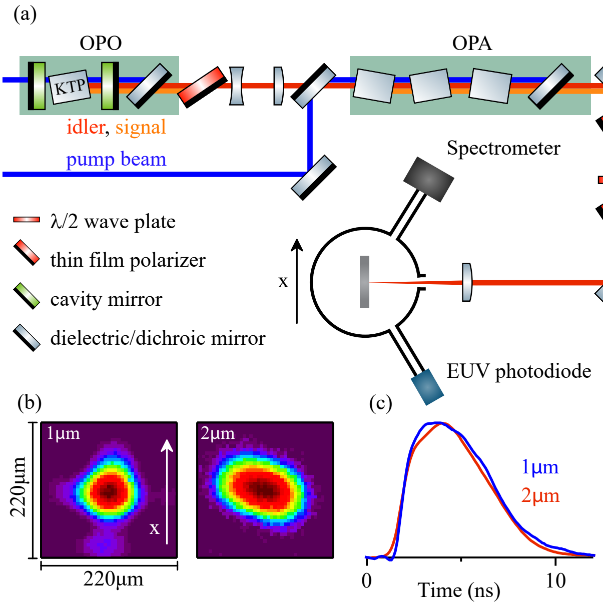

Figure 2.2: (a) Schematic representation of the experimental setup. A master oscillator power amplifier (MOPA) setup, comprising an optical parametric oscillator (OPO) and an optical parametric amplifier (OPA), is pumped by a Nd:YAG laser. The 2-μm idler beam from the MOPA is focused onto a planar tin target to create plasma. The EUV emission from the plasma is captured by a transmission grating spectrometer and a calibrated EUV photodiode. (b) Spatial profiles with Gaussian spot sizes of 66 × 66 μm FWHM for the 1-μm drive laser and 72 × 128 μm FWHM for the 2-μm drive laser. (c) Temporal profiles of the 1- and 2-μm drive lasers.

between 11 and 16 nm wavelength [79]. The spectra are corrected for second-order contributions above 11 nm wavelength by utilizing the tabulated second-order diffraction efficiency[80]. More details on the spectrometer and post-processing of the images are provided in Refs. [80] and [16]. To obtain the absolute amount of EUV radiation emitted in a 2% bandwidth around 13.5 nm, a calibrated EUV photodiode assembly[16] is used. It is installed at an angle of −60°, mirroring the alignment of the spectrometer cf. Fig. 2.2a. This photodiode assembly consists of a Mo/Si multilayer mirror that reflects the in-band radiation onto a photodiode. The photodiode is coated with a Si/Zr coating in order to block infrared light.

The 2-μm light source comprises a KTP-based MOPA operated in type-2 phase matching following the approach of Arisholm et al.[22]. The MOPA setup is pumped at a 10 Hz repetition rate by a seeded Q-switched Nd:YAG laser (QuantaRay 250-10 PRO) providing pulses of 10 ns duration (at full width at half maximum, FWHM). First, a 2170 nm idler seed beam of 1.8 mJ energy is created in a singly-resonant optical parametric oscillator (OPO). To create this seed beam, 18 mJ pump light is demagnified to a beam diameter of 1.5 mm and is coupled into the OPO which is operated in a collinear alignment. About 20% of the pump radiation is converted into a 2090 nm wavelength signal beam and a 2170 nm idler beam. At the exit of the OPO a dichroic mirror separates the signal and idler beams from the remaining pump radiation. The idler beam is subsequently expanded to 11 mm in diameter to seed the OPA, while the signal beam is removed through polarization optics. The OPO and OPA are pumped by the same laser. To achieve highest efficiency in the OPA, 1.3 J of the pump laser light is delayed by 1.3 ns and is reduced to a beam size of 10 mm in diameter. Seed and pump beams are overlapped on a dichroic mirror after which they pass three 18-mm-long KTP crystals. The crystal orientation is alternated to compensate for walk-off. A total energy of 260 mJ is achieved in signal and idler combined. Pump and signal beams are separated from the idler using a dichroic mirror and polarization optics, respectively. To adjust the idler beam energy a combination of a half-wave plate and a polarizer is installed before the focusing optics. The size of the focal spot on the target is 72 × 128 μm (FWHM). The asymmetry in the focal spot size is caused by the slightly higher beam quality on the horizontal, x-axis of the beam (cf. Fig. 2.2b). The pulse duration is 4.8 ns (FWHM); uncertainties in determining the pulse duration are at or below 0.5 ns. The pulse has a short rise time of $\sim$1 ns; its fall time is significantly longer and is seen to follow the pulse shape of the seed beam.

A seeded, in-house built Nd:YAG laser is used as the 1-μm laser light source to drive plasma [81]. The laser employs two electro-optical modulators to create temporal profiles of the desired shape. Here the temporal profile was shaped to match that of the idler of the MOPA (cf. Fig. 2.2c). A lens is used to focus the laser beam onto the tin target to a symmetric spot size of 66 μm (FWHM) closely matching the horizontal beam spot size of the idler beam in the measurement plane (cf. Fig. 2.2b).

2.3 Results

In the following, we assess the potential of a 2-μm-wavelength tin-plasma driver by studying the spectral characteristics with emphasis on EUV in-band radiation. Fig. 2.3a shows EUV spectra obtained when the beam intensity $I_{2\mu m}$ is varied in a 0.2–1.9 × 10^{11} W/cm^2 range. The intensity of 2-μm driver $I_{2\mu m}$ is given by the peak intensity in time and space by $I_{2\mu m} = (2\sqrt{2\ln 2/2\pi})^3 E_{2\mu m}/abt_p$. Here, $E_{2\mu m}$ is the laser energy, a and b are the Gaussian FWHM sizes along the major and minor axis of the elliptical beam, and t_p is the FWHM pulse duration. Spectral features belonging to Sn^{5+} to Sn^{15+} are observed in the studied spectral range [44, 46, 49, 82–84]. At the lower laser intensities, spectral features belonging to Sn^{5+} to Sn^{8+} are visible. At higher laser intensities, spectral features related to the higher charge states Sn^{10+} to Sn^{15+} are prominent. Spectral emission from these charge states also becomes visible

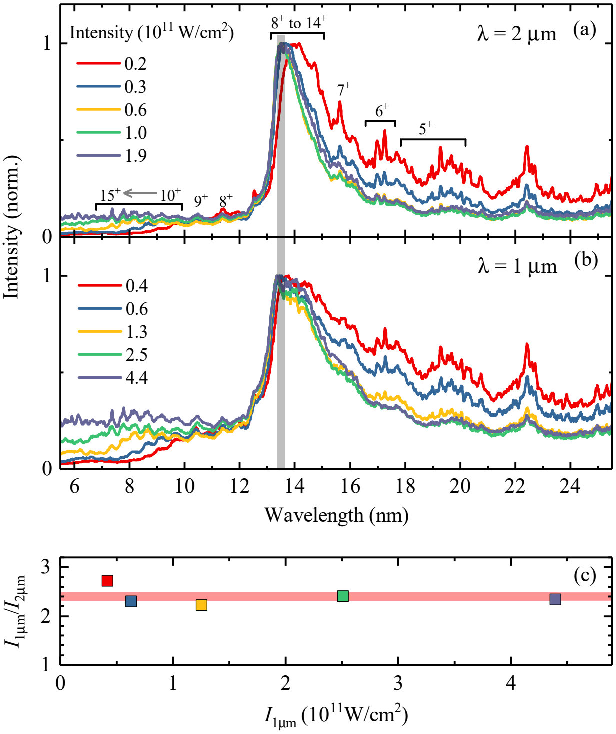

Figure 2.3: Spectra from plasma produced from a planar solid tin target irradiated with laser pulses at various intensities of the (a) 2-µm driver (4.8 ns pulse duration, Gaussian spot size of 72 × 128 µm). The emission features attributed to the various Sn ions are labeled by the respective charge state. (b) Spectra from tin plasma driven by a 1-µm-beam (4.4 ns pulse duration, Gaussian spot size of 66 × 66 µm). The gray vertical band indicates a 2% bandwidth centered at 13.5 nm. (c) Ratio of intensities of 1- and 2-µm drive laser beams needed to obtain spectra with matching short-wavelength features. The red line indicates the average ratio.

in the short-wavelength region of the spectra below 12 nm. The evolution of spectral features in this wavelength regime gives direct qualitative insight into the underlying charge state distribution as the contributions from the individual charge states can be identified[83].

For comparison, in Fig. 2.3b a set of spectra is presented that was obtained using the 1-µm-wavelength driver. Emission spectra are obtained for beam intensities $I_{1\mu m}$ ranging 0.4–4.4 × 10^{11} W/cm^2. $I_{1\mu m}$ is defined analogously to $I_{2\mu m}$. The beam intensities are selected such that similar short-wavelength features are obtained as in the respective 2-µm cases. The laser intensity at which any particular charge state distribution is obtained, is lower for the 2-µm case by about a factor two. The evolution of spectral features with laser intensity appears to be similar, comparing Fig. 2.3a and b.

To study this difference in more detail, pairs of intensities $I_{1\mu m}$ and $I_{2\mu m}$ were chosen such that the short-wavelength spectral features, ranging from 6 to 10 nm, in the respective emission spectra are best matching. In Fig. 2.3c, the ratio of thus selected pairs $I_{1\mu m}/I_{2\mu m}$ is plotted versus $I_{1\mu m}$. On average the 1-µm driver requires a constant factor 2.4(7) higher intensity to reach the same effective charge state distribution of the plasma when compared to the 2-µm case. The number in brackets in the ratio 2.4(7) indicates the overall uncertainty which is dominated by systematic uncertainty. This ratio is very similar to the one found, at a value of 2.1(6), for droplet-target experiments using the same drive laser [32].

From the simulation work of Nishihara et al. [60] presented also in Sec. 2.1 it is clear that the relation between the optimum laser intensity and the laser wavelength can be approximated from the product $I\lambda^{1.2}$ (rather than $I\lambda^2$) because the ion density n_i where the in-band emission mostly occurs is much lower than the critical density $n_\mathrm{c} \propto \lambda^{-2}$ for the relatively short-wavelength lasers. Studies on quasi-stationary ablation fronts [85] relevant for our current investigations support the findings of Nishihara et al. related to the scaling relations by pointing out that significant laser absorption occurs in the underdense coronal region, before the critical density surface. The theoretical scaling relations are fully in line with our current findings and with previous experiments as presented in our review in Sec. 2.1 and shed light on the physics origins of the plasma-emission of EUV light. Further radiation-hydrodynamic simulations (as presented in Ref. [32] and [86] for the droplet-target case) are however required for the current planar target case to investigate the details of the evolution of the relevant plasma conditions and their dependence on drive laser wavelength.

In Fig. 2.4a, CE is plotted versus drive laser intensity for the 1-µm and 2-µm cases. The measured in-band radiation is extrapolated from the measurement at 60° to the 2π steradian half-sphere facing the laser origin, assuming isotropic emission over this half-sphere. The open markers indicate data obtained from the spectra taken with the spectrometer under the same angle of 60°. Here, the measured spectral intensities integrated over the in-band range are calibrated by comparison to the in-band energies measured by the EUV photodiode. These in-band energies are measured simultaneously with the spectra. From literature, it is evident that the EUV emission from LPPs from planar solid targets is slightly anisotropic[87]. Several studies have indicated that the angular dependence of EUV emission is nearly independent on the focal spot size and the pulse duration[87–89]. Hence, remaining differences in laser beam characteristics, which were carefully matched in our experiments, are not expected to have a significant impact on our observations. Changing the drive wavelength for a tin-LPP on a planar solid target from 266 nm to 1 μm was found to lead to a reduced angular dependence of the in-band emission [78]. For droplet targets, a 10-μm-driven LPP was shown to exhibit only a slightly reduced anisotropy of the in-band emission in comparison to the 1-μm-driven LPP [90] and thus the relatively small step to 2-μm laser radiation is not expected to change the current EUV emission anisotropy significantly. We furthermore note that the observation under the current, relatively large angle of 60° constitutes a representative measure of the overall CE[16, 87–89]. Conclusions regarding final obtainable CE can be drawn only if also further laser parameters are varied and optimized. The laser focus size in particular is a sensitive parameter in the optimization. Spitzer et al. [68] presented a comprehensive database for source optimization by systematically varying parameters such as wavelength, pulse length, intensity, and spot size. The latter parameter was shown to have a significant influence on the obtainable conversion efficiency, a feature that was attributed to a changing dimensionality of the plasma expansion. Lateral heat conduction losses and multidimensional expansion losses reduce CE in the case of a small spot size [60]. Tao et al. [66] studied the influence of the focal spot size on in-band emission from Nd:YAG laser-produced Sn plasmas finding almost constant in-band conversion efficiency (at ∼2% value) with focal spot sizes ranging 60 to 500 μm contrasting the findings of Spitzer et al. [68]. Harilal et al. [65] and Koay et al. [91] also demonstrated high CE using Sn targets with small focal spot sizes of 60 and 35 μm, respectively, albeit for tin-doped spherical targets in the latter case. The findings are further corroborated by Yuseph et al. [92] who found that a shorter length scale plasma reabsorbs less EUV light, resulting in a higher conversion efficiency for the smaller focal spot when comparing 26 and 150 μm spot size cases. In the current experiments the spot sizes and the temporal pulse shapes of the two drive wavelength cases (cf. Fig. 2.2) have been carefully tuned to be as close as possible, such that a relative comparison is apt.

The CE of the 2-μm-LPP rises with beam intensity, up to a maximum value of 3.1% at a laser intensity of 1.0×10^{11} W/cm^2. When further increasing the laser

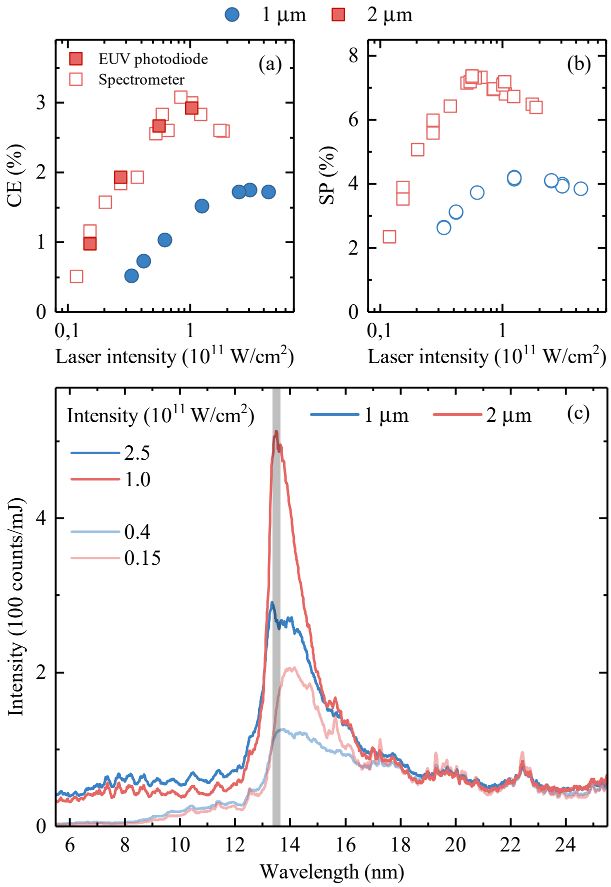

Figure 2.4: Comparison of tin plasma emission characteristics for the 1- and 2-µm drivers: (a) Dependency of conversion efficiency (CE) on drive laser intensity for both drivers. The plot shows CE directly captured by a calibrated EUV photodiode, mounted under a 60 degree angle (cf. Fig.2.2), as well as CE obtained from the absolute in-band measurements of the spectra, all assuming isotropic emission. (b) Spectral purity (SP) versus the intensity of the corresponding drive laser. (c) Juxtaposition of emission spectra. The intensity counts of the spectrometer are divided by the drive laser energy.

intensity CE decreases. For the 1-µm case, a similar rise of CE with increasing beam intensity is observed, with a maximum CE reaching 1.7%, i.e. only about half of that of the 2-µm case. The maximum CE for the 1-µm-LPP is reached at a laser intensity of 3.0×10^{11} W/cm^2. No decrease in CE is observed when moving to higher laser intensities, within the probed parameter space. Comparing the two drive laser cases, the relative difference in maximum CE amounts to a factor 1.8. The 1-µm-LPP requires significantly higher intensities to reach optimum CE. This is in line with the findings presented in Fig. 2.3c.

Fig. 2.4b shows the spectral purity of both the 1-µm and the 2-µm-LPPs as a function of laser intensities. Both SP data sets show a behavior that is similar to that of the corresponding CE curves. Note again that SP is here defined as the ratio of in-band EUV energy to the total energy emitted in the 5.5–25.5 nm range. The maximum SP of the 2-µm-LPP is at 7.4% a factor 1.8 larger than the value of the 1-µm-LPP with a maximum of 4.2%. This maximum SP is reached at a laser intensity of 1×10^{11} W/cm^2, very close to the value of 0.8×10^{11} W/cm^2 found for droplet-target experiments using the same drive laser [32]. The ratio of the maximum SPs is identical to the ratio of the maximum CEs. This indicates that the difference in conversion efficiency can be attributed to the decreased SP of the 1-µm-LPP. Figure 2.4c shows two pairs of matching emission spectra, i.e. plasmas having similar ionicities. The 2-µm-LPP spectra with the highest and lowest obtained CEs are shown. All spectra have been divided by the drive laser energy. The out-of-band features are seen to match well. It is apparent that a significant amount of spectral emission between 13 and 15 nm is missing in the 1-µm case compared to the 2-µm-LPP. This lack of emission in the unresolved transition array at 13.5 nm explains the reduced CE of the 1-µm-LPP.

To qualitatively explain the significant differences observed between the two drive laser cases, it is instructive to employ an intuitive two-zone radiation transport model. In this simple model, the emission from a hot plasma core zone ("zone 1") traverses a plasma zone ("zone 2") at a modestly lower density and temperature. Such a two-zone plasma approximates our experimental conditions where a laser beam with a Gaussian spatial intensity profile inhomogeneously heats the plasma. Further inhomogeneities are present along the laser beam propagation z-axis (see e.g. Ref. [85]). Our one-dimensional model captures only a rough average of the various sources of inhomogeneity. The second zone will contribute to the overall emission but will also partially absorb the light emitted from the first zone[93, 94]. Following Ref. [51], the spectral radiance L_λ of a homogeneous, one-dimensional plasma is given by $L_\lambda = B_\lambda\,(1 - e^{-\tau_\lambda})$. Here B_λ is the Planck function, assuming local thermodynamic equilibrium (LTE) conditions. The subscript λ indicates the wavelength dependency of L_λ. In the exponent, τ_λ is the wavelength-specific optical depth [43, 51]. The Planck function B_λ only depends on the wavelength and temperature and is independent of the ion density n_i [95]. The expected density and temperature values support our LTE approach (see, e.g., Ref. [43]) and small deviations from it do not meaningfully impact our qualitative analysis in the following. We now expand the model by adding a second layer of plasma. The first plasma layer emits the spectral radiance $L_{\lambda,1}$ over an optical depth $\tau_{\lambda,1}$. This light subsequently traverses a second plasma layer with an optical depth $\tau_{\lambda,2}$. The total spectral radiance $L_{\lambda,2}$ exiting the second layer of plasma is given by

$$L_{\lambda,2} = B_{\lambda,1}\,(1 - e^{-\tau_{\lambda,1}})\,e^{-\tau_{\lambda,2}} + B_{\lambda,2}\,(1 - e^{-\tau_{\lambda,2}})\,, \tag{2.1}$$

where $B_{\lambda,1}$ and $B_{\lambda,2}$ are the respective blackbody functions of the two plasma layers. Next, we take two spectra obtained from plasma driven by 2-μm-laser light. These two spectra serve as base spectra for the model's two plasma layers[51]. Both spectra are, for simplicity, assumed to be generated from a single density-temperature plasma layer with significantly high optical depth ($L \approx B$ at peak emission wavelength) of value $\tau_{\lambda,i} \cdot a_i$ ($i = 1, 2$ for zones 1,2) with a constant multiplication factor a_i accounting for differences in density or length scales following the approach of Schupp et al.[51]. The optical depth of the plasma is expected to be reduced by a factor of up to 2 when going from 1- to 2-μm driver [32]. Given the large optical depth in the 1-μm case, as shown e.g. in Ref. [51], a sufficiently large optical depth is still to be expected in the current 2-μm case to remain within the limit of large optical depth at peak opacity (which is sufficient for our model).

In the following, the base spectrum of the first zone is associated with the maximum CE (cf. Fig. 2.4c). The base spectrum for the second zone is chosen from a modestly lower laser intensity, corresponding to a modestly lower plasma temperature conform our model. Following Ref. [43] the effective temperature of the first zone is set to 32 eV associated with optimum plasma conditions for producing in-band EUV light at the here expected plasma densities[43]. The plasma temperature of the second zone is subsequently found by matching the relative intensity values of the two base spectra at 13.5 nm wavelength (as $L \approx B$ at peak emission wavelength given the large optical depths involved[43, 51] also for the 2-μm-driven base spectra). This results in a temperature of 29 eV for the second zone. The model fit function $L_{\lambda,2}$ is then given by

$$\begin{aligned} L_{\lambda,2} = a_0(&B_{\lambda,1}(T = 32\mathrm{eV})\,(1 - e^{-a_1\tau_{\lambda,1}})\,e^{-a_2\tau_{\lambda,2}} \\ &+B_{\lambda,2}(T = 29\mathrm{eV})\,(1 - e^{-a_2\tau_{\lambda,2}})). \end{aligned} \tag{2.2}$$

The multiplication factors a_i are used as free fit parameters, including an additional overall amplitude factor a_0. This amplitude factor a_0 is required because the measured

1-µm-driven spectrum cannot be normalized by the Planck function at peak emission wavelength, as in the case of the 2-µm-driven base spectra, since the observed self-absorption from a multi-(n_i, T) plasma voids the relation $L \approx B$ at peak emission wavelength. The a_0 fit value itself has no further physical meaning within the current context.

Fig. 2.5 shows the result of a least-squares fit of the model function Eq. (2.2) to the measured 1-µm-driven spectrum at a 2.5×10^{11} W/cm^2 laser intensity that reproduces the ionicity of the 2-µm-driven base spectrum (see Fig. 2.4c). The model is seen to excellently reproduce the data. The fit parameters obtained are $a_1 = 1.3$ and $a_2 = 0.7$, close to unity value such that the original base spectra are already representative of the emission of the two zones. A more quantitative interpretation of these fit values is not currently warranted given the qualitative nature of the model application. A comprehensive explanation of the generic effects of a two-zone plasma is provided in Ref.[93] albeit for hotter and denser plasma. EUV radiation, produced in the hottest part of the plasma, passes through regions of underheated plasma generated by the lower-intensity parts of the Gaussian laser intensity profile and the underheated plasma naturally present along the laser propagation, and rarefaction (z-)axis. The EUV emission in the case of the 1-µm-drive laser occurs at a higher plasma density than that of the 2-µm-driver and also its underheated plasma zone will have higher ion density. Hence, the 1-µm-LPP exhibits a higher EUV self-absorptivity (also see the work of Bouza et al. [96]) in the underheated zone making the 2-µm-LPP here the more efficient emitter of in-band EUV radiation. We note that self-absorption effects are absent in recent droplet-target experiments [32] in line with expectations given that the lower-intensity parts of the Gaussian-focus laser pulse do not interact with the small droplet target in that work.

2.4 Conclusion

In conclusion, efficiencies of converting laser energy into in-band EUV photons into a 2π-sr half-sphere (CEs) in excess of 3% have been achieved from a Sn plasma driven by a 2-µm-wavelength laser system assuming isotropic emission. It here outperforms plasmas driven by a 1-µm-laser by a factor of two. The difference between the two drive laser cases can furthermore be qualitatively explained from self-absorption effects. Our findings regarding the scaling of the optimum laser intensity for efficient EUV generation and CE with drive laser wavelength are in broad agreement with the available literature, here moving into the territory between 1 and 10 µm wavelength. Further increases in CE are to be expected when providing a homogeneous heating of the plasma, optimizing the spatio-temporal intensity profile of the drive laser. Investigations of the EUV emission anisotropy enable to fully capture the emission characteristics. Such

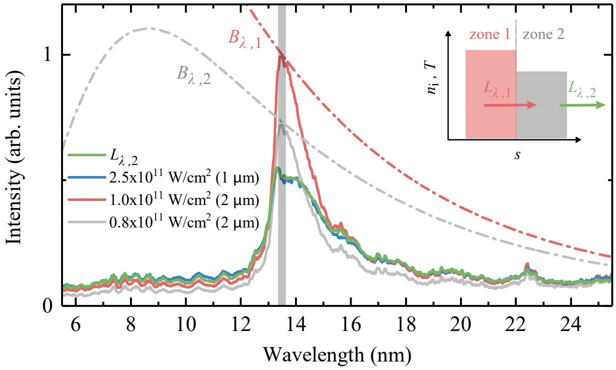

Figure 2.5: Tin spectra from plasmas driven by 1- and 2-µm-lasers. The blackbody functions $\boldsymbol{B}_{\lambda,1}$ and $\boldsymbol{B}_{\lambda,2}$ are divided by $\boldsymbol{B}_{13.5\,\mathrm{nm},1}$. The 2-µm-LPP spectra are scaled to be confined by their respective blackbody functions. The 1-µm-LPP spectrum is scaled according to the amplitude ratio of the respective spectra in Fig. 2.4c. The green curve depicts the fit result of Eq. (2.1) to the 1-µm-LPP spectrum (see main text). The inset schematically depicts the model.

future studies, preferably executed on mass-limited droplet targets, will further pave the way for the application of 2-µm drive lasers in industrial sources of EUV radiation powering tomorrow's nanolithography.

Acknowledgements

This work has been carried out at the Advanced Research Center for Nanolithography (ARCNL), a public-private partnership of the University of Amsterdam (UvA), the Vrije Universiteit Amsterdam (VU), the Netherlands Organisation for Scientific Research (NWO) and the semiconductor equipment manufacturer ASML. The used transmission grating spectrometer has been developed in the Industrial Focus Group XUV Optics at University of Twente, and supported by the FOM Valorisation Prize 2011 awarded to F. Bijkerk and NanoNextNL Valorization Grant awarded to M. Bayraktar in 2015.

CHAPTER 3

CHARACTERIZATION OF 1- AND 2-µm-WAVELENGTH LASER-PRODUCED MICRODROPLET-TIN PLASMA FOR GENERATING EXTREME ULTRAVIOLET LIGHT

R. Schupp, L. Behnke*, J. Sheil, Z. Bouza, M. Bayraktar, W. Ubachs, R. Hoekstra, and O. O. Versolato

Physical Review Research **3**, 013294 (2021).

Experimental spectroscopic studies are presented, in a 5.5–25.5 nm extreme ultraviolet (EUV) wavelength range, of the light emitted from plasma produced by the irradiation of tin microdroplets by 5-ns-pulsed, 2-µm-wavelength laser light. Emission spectra are compared to those obtained from plasma driven by 1-µm-wavelength Nd:YAG laser light over a range of laser intensities spanning approximately 0.3–5 × 10^{11} W/cm^2, under otherwise identical conditions. Over this range of drive laser intensities, we find that similar spectra and underlying plasma charge state distributions are obtained when keeping the ratio of 1-µm to 2-µm laser intensities fixed at a value of 2.1(6), which is in good agreement with RALEF-2D radiation-hydrodynamic simulations. Our experimental findings, supported by the simulations, indicate an approximately inversely proportional scaling $\propto\lambda^{-1}$ of the relevant plasma electron density, and of the aforementioned required drive laser intensities, with drive laser wavelength λ. This scaling also extends to the optical depth that is captured in the observed changes in spectra over a range of droplet diameters spanning 16–51 µm at a constant laser intensity that maximizes the emission in a 2% bandwidth around 13.5 nm relative to the total spectral energy, the bandwidth

---

* LB designed and set up the 2-µm laser, and equally contributed to planning, preparing and conducting experiments, and operation of lasers

relevant for EUV lithography. The significant improvement of the spectral performance of the 2-µm- vs 1-µm-driven plasma provides strong motivation for the development of high-power, high-energy near-infrared lasers to enable the development of more efficient and powerful sources of EUV light.

3.1 Introduction

Laser-driven microdroplet-tin plasma provides the extreme ultraviolet (EUV) light that is used in state-of-the-art EUV lithography [39, 40, 42, 44, 97–99]. Ever more powerful sources of EUV light are required for future lithography applications. This EUV light is generated from electronic transitions in multiply charged tin ions that strongly emit radiation in a narrow band around 13.5 nm [45–50, 82, 84, 100–102]. EUV-emitting plasma in an industrial nanolithography machine is driven by CO_2-gas lasers with a 10-µm wavelength. Such plasma achieves particularly high conversion efficiencies (CE) of converting drive laser light into EUV radiation in a 2-% wavelength bandwidth around 13.5 nm, the so-called in-band radiation, that can be transported by the available Mo/Si multilayer optics [103, 104]. Near- or mid-infrared solid-state lasers may however soon become an attractive alternative to the CO_2-gas lasers because such modern solid-state lasers are expected to have a significantly higher efficiency in converting electrical power to laser light. Furthermore, they may reach much higher pulse energies and output powers, in turn enabling more EUV output. Big Aperture Thulium (BAT) lasers [5, 6] represent a particularly promising class of novel, powerful laser systems that have recently drawn significant attention. These lasers would operate at 1.9-µm wavelength, in between the well-known cases of 1- and 10-µm drive lasers. Recent simulation work indicates that a global CE optimum lies within this range of 1- and 10-µm drive laser wavelength [58]. Briefly, such studies point out that the longer-wavelength drivers are associated with sub-optimal absorption of the laser energy by the plasma whereas shorter-wavelength drivers may exhibit severe opacity broadening of the EUV spectrum out of the 2-% acceptance bandwidth [51–53]. To date, no experimental studies of mass-limited, microdroplet-tin-based plasmas driven by lasers in this wavelength range are however available to verify these claims.

In this article a study of the EUV emission spectrum of 2-µm-wavelength-laser-driven tin-microdroplet plasma is presented. The laser light is obtained from a master oscillator power amplifier setup that comprises a series of KTP crystals pumped by a ns-pulsed Nd:YAG laser ($\lambda \approx 1$ µm), enabling one to gauge the potential of, e.g., thulium lasers without the effort of building one. The recorded spectroscopic data are compared to those obtained from a 1-µm-driven plasma under otherwise identical conditions, over a wide range of droplet sizes and laser intensities. Radiation-hydrodynamic simulations using the RALEF-2D code [105], are presented to support the experimental findings.

Following the recent work of Schupp *et al.* [51] on Nd:YAG-laser-pumped plasma, an analytical solution for radiation transport in an optically thick one-dimensional plasma is used to quantify the influence of optical depth on the broadening of the key emission feature at 13.5 nm.

3.2 Experiment

In the first set of experiments micrometer-sized liquid tin droplets are irradiated with high-intensity 2-µm-wavelength laser pulses produced in a master oscillator power amplifier (MOPA). Following the work of Arisholm *et al.* [22], the MOPA consists of a singly resonant optical parametric oscillator (OPO) in collinear alignment followed by an optical parametric amplifier (OPA). The latter comprises two 18-mm long KTP crystals operated in type II phase matching. The setup (see Fig. 3.1) is pumped by a seeded Nd:YAG laser with a spatially flat-top and a temporally Gaussian profile of 10 ns (FWHM). The OPO is pumped with 18 mJ of energy within a 1.5-mm-diameter beam resulting in an idler beam energy of 1.8 mJ at a wavelength of 2.17 µm. The OPO is operated slightly off its degeneracy point to minimize back conversion of signal and idler into the pump wavelength, a process which reduces beam quality of both beams. After the OPO the signal beam is removed and the idler beam expanded to 11 mm and amplified in the OPA. Using 1.3 J of pump energy within a beam diameter of 10 mm, 260 mJ of 2-µm radiation are obtained, summing signal and idler pulse energies. The pulse duration of both beams after amplification is 4.3 ns.

For the experiments the signal beam is removed via polarization optics and solely the idler beam is used. The idler beam is focused onto several ten-micrometer-sized liquid tin droplets created via coalescence of even smaller microdroplets from a tin jet in a vacuum chamber that is kept at or below 10^{-6} mbar. The diameter of the microdroplets is adjustable within a range from 16–51 µm. The focal spot is elliptical and has a size of 65×88 µm (FWHM) and laser intensities of up to 2.1×10^{11} W/cm^2 are obtained on the tin droplets. Data taken with this 2-crystal setup is used for Sec. 3.4 and is part of the data in Fig. 3.2(c). The intensity is defined as peak intensity in time and space and calculated to $I_\mathrm{L} = (2\sqrt{2\ln 2/2\pi})^3 E_\mathrm{L}/abt_\mathrm{p}$ with laser energy E_L, FWHMs a and b along the major and minor axis of the bivariate Gaussian and pulse duration t_p. The energy in the beam is adjusted by the combination of a half-waveplate and polarizer. The data displayed in Fig. 3.2(a) was taken in a later experiment and after installation of a third crystal in the OPA which increased the energy in signal and idler combined to 360 mJ while the pulse duration increased slightly to 4.7(3) ns (FWHM). The produced beam has a symmetric focal spot and measurements are obtained for three focal spot sizes of 106, 152 and 194 µm (FWHM) that are obtained using lenses of different focal

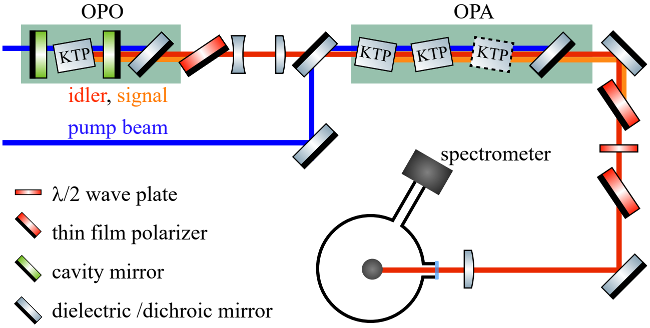

Figure 3.1: Schematic representation of the experimental setup. A master oscillator power amplifier (MOPA) setup, comprising an optical parametric oscillator (OPO) and an optical parametric amplifier (OPA), is pumped by a Nd:YAG laser (blue line). The signal beam is separated via polarization optics and the idler beam ($\lambda = 2.17\,\mu\mathrm{m}$) is focused onto tin microdroplets within a vacuum chamber. EUV emission is captured by a transmission grating spectrometer positioned at 60° with respect to the laser axis. An additional, third KTP crystal (dashed outline) was used in the OPA in a subset of the experiments.

distance length. The data obtained in the first and this later experiment is combined in Fig. 3.2(c).

To enable a direct comparison with plasmas driven by 1-μm wavelength laser pulses, light from the 1-μm pump laser is redirected before entering the MOPA and is focused onto the tin droplets instead. Again, a combination of a half-wave plate and polarizer allows for adjustment of the beam energy. The focal spot has a symmetric Gaussian shape of 86 μm (FWHM). The EUV emission from the tin plasma is collected by a transmission grating spectrometer [80] set up under a 60° angle with respect to the incoming laser beam. The spectrometer was operated with a 10 000 lines/mm grating, a 25 μm slit and without filter. The measured spectra are corrected for the grating's first and second order diffraction efficiency as well as for the quantum efficiency of the camera. The wavelength is calibrated in a separate experiment using atomic line emission from an aluminum plasma. Spectral purity (SP), defined as the ratio of spectral energy in a 2% bandwidth around 13.5 nm to the total EUV energy, is used to characterize the EUV light source. All SP values provided are calculated with respect to the measured spectral range of 5.5–25.5 nm.

3.3 Scaling of spectral features with laser intensity and wavelength

For defining development targets regarding power and pulse energy of future 2-μm lasers for use in EUV light sources, it is particularly relevant to know the laser intensity needed to obtain a tin charge state balance optimal for the production of 13.5-nm light. In this section the laser intensity on the tin droplet is scanned and the optimal laser intensity determined as the value at which SP is highest, given that SP is the ultimate limit of CE as follows from energy conservation CE<SP/2 for isotropic emission [16]. To better understand the relevant plasma temperatures and densities, we study the ratio of 1- and 2-µm laser intensities at which plasmas of equal temperatures are established. Plasma temperature is experimentally established via the shape and amplitude of charge state specific spectral emission features [83, 96, 106, 107]. These features are indicative of the plasma's charge state distribution which is predominantly dependent on plasma temperature [85]. The experimental results are then compared to computer simulations using the radiation-hydrodynamic code RALEF-2D as well as to previous analytic work [85].

Spectral dependencies on drive laser intensity

In the experiments, first the idler beam from the MOPA is focused onto a 30-µm-diameter droplet and spectra are measured using the 106-µm spot size at multiple intensities within a range of $0.1–2.2 \times 10^{11}$ W/cm^2 (see Fig. 3.2(a)). At the lowest laser intensity the plasma strongly emits around 14.5 nm and distinct $4d$–$4f$ transitions in Sn^{6+} are visible around 17 nm [96]. Emission between 18–20 nm can be mainly attributed to Sn^{5+}. At 15.7 nm, a strong emission feature from $4d$–$4f$ and $4p$–$4d$ transitions in Sn^{7+} is visible. Going up this "ladder" of charge states, emission from $4d$–$4f$ and $4p$–$4d$ transitions in Sn^{8+} is visible at 14.8 nm and from Sn^{9+} at 14.2 nm. With increasing laser intensity the average charge state of the plasma increases and emission from Sn^{10+} is evident in the 9.5–10 nm region [83]. Increasing laser intensity beyond 10^{11} W/cm^2, the plasma strongly emits at 13.5 nm. This emission originates from the $4d$–$4f$, $4d$–$5p$ and $4p$–$4d$ unresolved transitions arrays (UTAs) in Sn^{8+}–Sn^{14+} [44, 82]. With the strong emission at 13.5 nm, charge state specific features become visible between 7 and 12 nm. These features belong to the same Sn^{8+}–Sn^{14+} ions and here the $4d$–$5f$, $4d$–$6p$ and $4p$–$5s$ transitions contribute strongest [83, 106]. With increasing laser intensity SP rises to values of 15% at 0.8×10^{11} W/cm^2 where charge state balance is optimal for in-band EUV emission, before reducing again at even higher intensity values (see inset in Fig. 3.2(b)).

Second, plasma is created using laser light of 1-µm wavelength. Spectra for laser intensities within the range of 0.3×10^{11} W/cm^2 to 4.4×10^{11} W/cm^2 are shown in Fig. 3.2(b). When compared to the 2-µm drive-laser case the spectra show very similar shape, albeit at an apparent increased overall width. Again the same emission features of charge states Sn^{5+}–Sn^{9+} are visible at the lowest laser intensity but with somewhat less prominent emission features. This reduction in prominence is particularly noticeable

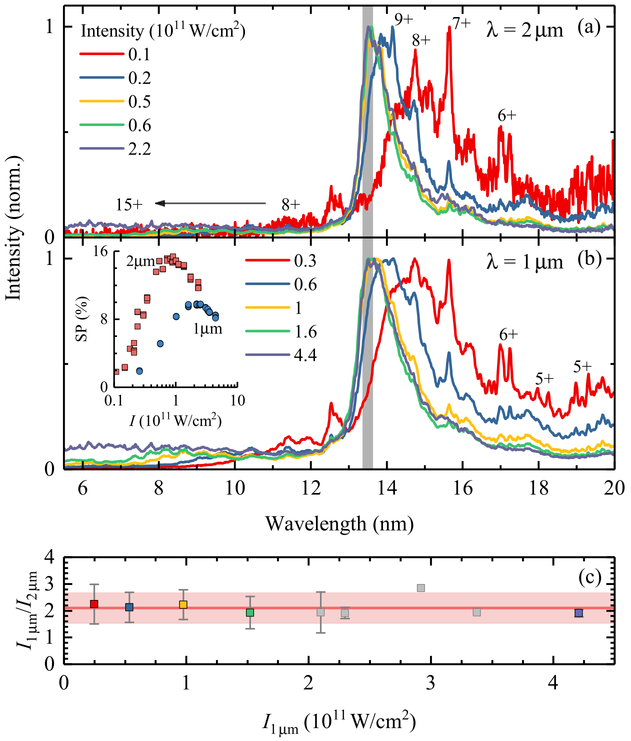

Figure 3.2: Spectra from tin droplet plasma observed at various intensities of the (a) 2-μm beam (4.7 ns pulse duration, 106 μm FWHM, 3 KTP crystals) and the (b) 1-μm Nd:YAG beam (10 ns pulse duration, 86 μm FWHM). The droplet size in both cases is 30 μm. (c) Ratio of the intensities of 1- and 2-μm drive laser beams needed to obtain spectra with similar spectral features. The data points represent the average intensity ratios from data taken with four different laser spot sizes of the 2-μm laser beam of 65×88, 106, 152 and 194 μm (FWHM), respectively. The error bars indicate the standard deviation per measurement. The red line represents the average over all data points and the shaded band the standard deviation of the average.

for the peaks of charge states Sn^{6+} and Sn^{7+} (between 14 and 16 nm). Further the Sn^{9+} peak at 14.2 nm is hardly visible (cf. $0.2 \times 10^{11}\ \mathrm{W/cm^2}$ in the 2-μm case). The SP rises until it reaches values of 9.7% around $2 \times 10^{11}\ \mathrm{W/cm^2}$ and subsequently decreases as the charge state balance becomes sub-optimal for emission of 13.5 nm light. The peak intensities used in this work agree well with previously published work, where the optimal SP was found at an intensity of $1.4 \times 10^{11}\ \mathrm{W/cm^2}$ using a temporally and spatially box-like laser profile to illuminate the tin droplets [16]. The higher intensity value found in this work is attributed to the fact that, because of their spatial extent, the droplets experience a slightly lower average intensity compared to the peak values stated.

To obtain the sought-for laser-intensity ratio $I_{1\mu\mathrm{m}}/I_{2\mu\mathrm{m}}$, each spectrum of the 2-μm laser case at intensity $I_{2\mu\mathrm{m}}$ is matched to a spectrum of the 1-μm case at intensity $I_{1\mu\mathrm{m}}$ for which the resemblance of the relative amplitudes and shape of spectral features is best matching. As the spectral features are characteristic of individual tin charge states [96, 107] this comparison provides access to the scaling of the plasma's charge state distribution (and hence temperature) with laser wavelength. For each match of laser intensities the ratio $I_{1\mu\mathrm{m}}/I_{2\mu\mathrm{m}}$ is calculated and plotted as a function of $I_{1\mu\mathrm{m}}$ in Fig. 3.2(c). The data points represent the average of comparisons made for multiple spot-size conditions and for two droplet size conditions. In all cases spectra were compared to the ones taken with the 1-μm wavelength laser beam size of 86 μm. More specifically, the comparison encompasses measurements with a 30-μm-diameter droplet for 2-μm case beam sizes of 65×88, 106×106, 152×152 and 194×194 μm and on a 19-μm-diameter droplet for the 65×88-μm beam. The red line shows the average $I_{1\mu\mathrm{m}}/I_{2\mu\mathrm{m}} = 2.1(6)$ of all measurements with the standard deviation (distribution width and not the error-on-the-mean) of the mean value as red shaded area. The depicted uncertainty is the standard deviation of the mean.

Theory and discussion

The temperature of a plasma can be expressed analytically if the equation of state (EOS) is sufficiently well known. The required EOS parameters will however depend on the location in the plasma where the laser light is absorbed. Two cases can be distinguished [85]. Case I: absorption of laser light dominantly occurs close to the critical surface where the plasma's electron density equals the critical density ($n_e \approx n_{\mathrm{crit}} \propto \lambda^{-2}$). This case is relevant for long wavelength laser light, e.g., from $\mathrm{CO_2}$ lasers. Case II: absorption is already significant in the underdense corona where the electron density is lower than the critical electron density. For laser absorption of 1- and 2-μm beams, case II applies and the tin plasma temperature can be written as [85]

$$T \propto \left(\frac{1}{R\lambda^2}\right)^{-0.19} [I(1-\phi_r)]^{0.44}, \tag{3.1}$$

with laser wavelength λ, laser intensity I, radiative loss fraction ϕ_r of the plasma and characteristic radius of the sonic surface R, defined as the contour at which the ion velocity equals the local sound velocity. The numerical values for the powers -0.19 and 0.44 originate from the EOS [85]. Differences in radiative losses of the plasmas are neglected in the following, as they may be small for similar density and temperature plasmas. The sonic surface R is only slightly wavelength dependent and the small difference can be neglected. From Eq. (3.1), an intensity ratio $I_i/I_j = (\lambda_j/\lambda_i)^{0.86}$ here $I_{1\mu\text{m}}/I_{2\mu\text{m}} = 1.8$ is calculated for $\lambda = 1$ and 2 µm plasmas exhibiting equal plasma temperatures. The predicted ratio of 1.8 agrees well with the experimental one of 2.1(6) and well approximates a scaling with λ^{-1}.

Alongside this analytical approach, the radiation hydrodynamic code RALEF-2D [105] is used to determine the laser intensity ratio yielding equivalent plasma temperatures. RALEF-2D was developed to simulate laser plasma interaction and solves the equations of fluid dynamics in two dimensions (assuming cylindrical symmetry around the laser beam propagation axis) while including necessary physical mechanisms such as laser absorption, thermal conduction and radiation transport. The latter is needed for accurate predictions of a strongly radiating plasma, which is true for the current case. An extensive set of simulations has been performed at conditions close to the experimental ones. A 30-µm-diameter droplet is irradiated by temporally and spatially Gaussian beams. The 1- and 2-µm beams have pulse durations of 10 and 4.3 ns (FWHM) and sizes of 80 and 100 µm (FWHM), respectively. Laser intensities in the range spanning 10^{10}–10^{12} W/cm^2 are simulated. The plasma's peak temperature is plotted in Fig. 3.3. For the given laser intensities the maximum temperature is consistently higher in the 2-µm case. We note that the different pulse durations (10 vs. 4.3 ns) have a minimal impact on temperature and density scales. The maximum temperatures are seen to follow Eq. (3.1) fitted as $T[\text{eV}] = a \cdot \lambda^{0.38}[\mu\text{m}] \cdot I^{0.44}[10^{11}\ \text{W/cm}^2]$, where a common amplitude $a = 43$ is determined by a global fit to all data. Eq. (3.1) captures the scaling of the peak plasma temperature over two decades in laser intensity.

Further shown in Fig. 3.3 are temperature and electron density lineouts along the laser axis away from the droplet at intensities relevant for the efficient emission of EUV light. The intensity of the 1- and 2-µm cases were chosen to have nearly identical peak electron temperature. This temperature strongly increases with distance from the droplet surface and peaks around 11 µm from the droplet surface before it reduces again at larger distances. The maximum temperature is obtained at a factor of 2.0 lower density in the 2-µm case. The point of highest temperature is much closer to

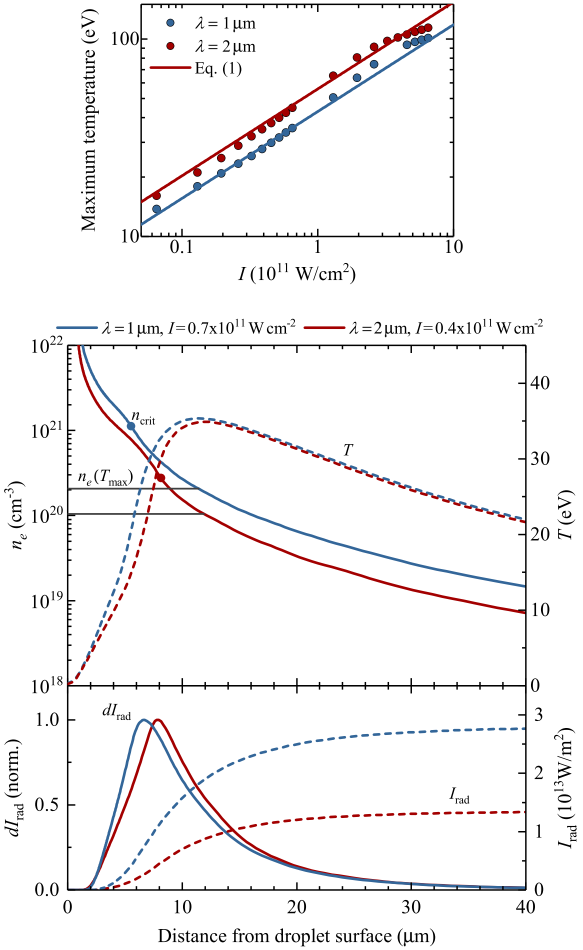

Figure 3.3: Top: maximum temperature of a tin plasma for various laser intensities calculated with the two-dimensional-radiation transport code RALEF-2D. A 30-µm-diameter droplet is illuminated with temporally and spatially Gaussian-shaped laser pulses of wavelengths 1 and 2 µm. Center: temperature and electron density lineout along the axis of the incoming laser beam. Bottom: frequency-integrated local radiation field intensity I_{rad} of the plasma and its normalized derivative dI_{rad}. The radiation field intensity is calculated from Eq (3.3) using the density and temperature lineouts depicted in the center panel. For more detail see text.

the critical density in the 2-μm case indicating that the absorption of laser light occurs closer to critical density while the conditions for laser absorption of case II are still met. Following Ref. [85], and references therein, the scaling of the relevant plasma electron density with wavelength can also be approximated invoking a constant absorbed fraction of the laser light, $k_L R = \text{constant}$. Inserting the Kramers' absorption coefficient for laser radiation k_L we obtain [85, 108]

$$(R\lambda^2)\rho^2\bar{z}^3T^{-3/2} = \text{constant}, \tag{3.2}$$

with the mass density ρ and the plasma's average charge state $\bar{z}$. Considering that mass density ρ and ion density n_i follow the ratio of electron density and average charge state $\rho \propto n_\mathrm{i} = n_e/\bar{z}$, where $\bar{z} \approx 22.5T^{0.6}[\text{heV}]$ (note that T is input here in units of 100 eV) [85], it becomes clear that the ratio of the electron densities lineouts displayed well approximates the ratio of mass density between the two laser wavelength cases. All other factors remaining constant in Eq. (3.2), a reciprocal scaling of mass density ρ and wavelength λ becomes directly apparent. The difference in mass density can thus be attributed to the difference in absorptivity of the laser radiation from Kramers' law [109]. This inversely proportional scaling of density with wavelength is the root cause of the observed intensity ratio.

The bottom panel of Fig. 3.3 shows the radiation field intensity I_rad and its normalized derivative dI_rad. The frequency-integrated radiation field intensity is calculated from

$$I_\text{rad}(s) = I_0 e^{-\int_{s0}^{s}\alpha(s')ds'} + \int_{s0}^{s}\alpha(s')B(s')e^{-\int_{s'}^{s}\alpha(s'')ds''}ds' \tag{3.3}$$

with the Planck mean absorptivity $\alpha_p[\text{m}^{-1}] = 3.3\times10^{-7}\cdot\rho[\text{g/cm}^3]\cdot T^{-1}[\text{eV}]$ using the temperature and electron density information in Fig. 3.3. For more information see Ref. [110]. The normalized derivatives dI_rad peak at 6.5 and 8 μm distance from the droplet surface for the 1- and 2-μm cases, respectively. They show that the typical length scales of emission are similar in both wavelength cases. This finding is in line with the similarity in length scales and indeed profiles of plasma temperature and density (shown in the center panel of Fig. 3.3). The point of largest change in radiation field intensity is located slightly closer to the droplet surface than the point of maximum temperature. The significantly higher density more than compensates for the drop in temperature. The point of largest change in the radiation field intensity of the 1-μm-driven plasma occurs relatively far from the critical density, whereas in the 2-μm-driven plasma this point lies close to the critical density, an observation explained by the distances between the respective maximum temperatures and critical densities. The radiation field intensity at large distances from the droplet surface is approximately a factor of two higher in the 1-µm case because of the factor of two higher (emitter) density compared to the 2-µm case.

3.4 Scaling of optical depth

The scaling of mass density with drive laser wavelength $\rho \propto \lambda^{-1}$ at similar length scales, as established by our simulations, indicates that the optical depth of the plasma, being a product of atomic opacity, mass density and path length, should scale similarly. If optical depth indeed reduces proportionally with drive laser wavelength, the step to a 2-µm laser system could be particularly beneficial. In the following, we perform an analysis of the optical depth associated with the EUV spectra by varying plasma size following the work of Schupp *et al.* [51]. This is accomplished by irradiating droplets having diameters in the range 16–51 µm.

Scaling of peak optical depth with droplet size and drive laser wavelength: examples

In our experiments the droplet diameter is changed in controlled steps from 16–51 µm and a constant laser intensity is used for both laser wavelength cases. First, droplets are illuminated with 2-µm laser light with an intensity of 1.1×10^{11} W/cm^2, close to optimal SP. The spot size is 65×88 µm. In Fig. 3.4 spectra for the smallest and largest droplet diameter are shown for both drive-laser cases. With increasing droplet diameter the main emission feature at 13.5 nm widens and more intense short-wavelength radiation is emitted relative to the 13.5-nm peak. Second, the same scan is repeated with 1-µm laser light at 2.4×10^{11} W/cm^2, an intensity chosen based on the intensity ratio in Fig. 3.2(c). Again, the main emission feature at 13.5 nm widens with increasing droplet diameter and more intense short wavelength radiation is emitted relative to the 13.5-nm peak. For the 1-µm driver these effects however are much stronger.

In the following, the spectra are analyzed regarding their optical depth similar to the analysis in Ref. [51]. The wavelength-dependent optical depth $\tau_\lambda := \int \kappa_\lambda \rho dx$ is defined as the spatial integration over the product of the plasma's opacity κ_λ and mass density ρ. In the instructive case of a one-dimensional plasma [60] in local thermodynamic equilibrium (LTE), the spectral radiance is given by $L_\lambda = B_\lambda(1 - e^{-\tau_\lambda})$, where B_λ is the Planck blackbody spectral radiance. We note that our high-density, strongly collisional 1- and 2-µm-driven plasmas are reasonably well approximated by LTE [110]. At equal temperatures, and thus average charge state (recall $\bar{z} \sim T^{0.6}$ [85]), this equation enables each measured spectrum $\sim L_{\lambda,i}$ to be well approximated by any other spectrum $\sim L_{\lambda,j}$ when taking into account the ratio of the corresponding

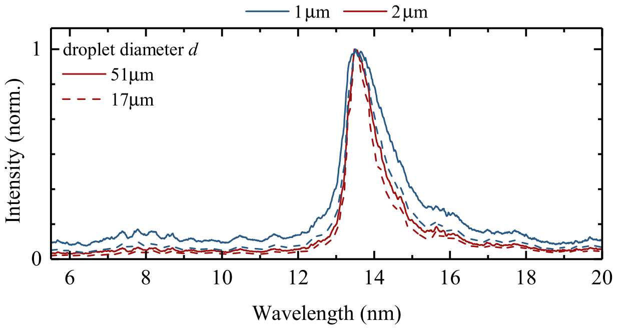

Figure 3.4: Spectral emission from tin plasmas produced with 1- and 2-μm laser wavelength for small and large droplet diameters at laser intensities of 2.4 and 1.1×10^{11} W/cm^2, respectively.

peak optical depths $a = \tau_{p,i}/\tau_{p,j}$ as a single parameter independent of wavelength (see Ref. [51] and the Appendix for further details). Subsequently, if any peak optical depth $\tau_{p,j}$ is known in absolute terms, the optical depth of any other spectrum can be deduced. To be able to correct for systematic errors that could possibly occur for relatively low optical depth $\tau \lesssim 1$ we have suitably modified the equation used in Ref. [51] as is detailed in the Appendix.

As a reference spectrum, the spectrum measured at 1-μm laser wavelength, 10-ns pulse duration and 30-μm droplet size is chosen. The peak optical depth of this spectrum is determined by comparison of its 13.5-nm feature to opacity calculations in Ref. [110]. More specifically, radiation transport is applied to the opacity spectrum calculated in Ref. [110] for a here relevant mass density of $\rho = 0.002\,\mathrm{g/cm^3}$ and electron temperature of $T_e = 32\,\mathrm{eV}$. The difference between radiation transported opacity spectrum and experimental spectrum is then minimized by changing the optical depth parameter τ_p in a least-square fit routine. This procedure leads to an absolute peak optical depth of $\tau_{0,p} = 4.5$ for our reference spectrum.

Using Eq. (3.7) the peak optical depth $\tau_{i,p}$ of all spectra is fitted with respect to the reference spectrum. As expected, inserting the relative optical depth obtained from the fits into Eq. (3.6) leads to an excellent reproduction of the main emission feature, as is shown in Fig. 3.5 for a typical example spectrum (30-μm droplet with a 2-μm driver). A further reasonable reproduction of the 7–12 nm features is established with the 2-μm driver outperforming the model spectrum with respect to the amount of radiation emitted out-of-band. Figure 3.5 also shows a spectrum from an industrial plasma produced by a 10-μm CO_2 driver which represents the limiting case of low optical depth. The step from a 1-μm to a 2-μm driver clearly significantly enhances the spectrum.

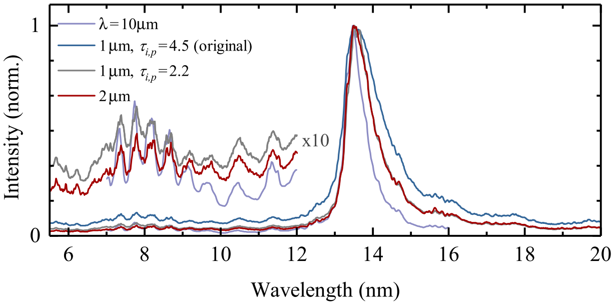

Figure 3.5: Spectrum produced with 2-µm laser light (red line) compared to the radiation-transported reference spectrum for a peak optical depth value of $\tau_p = 2.2$ (gray line, barely distinguishable from the red line). Reference and 2-µm-driven spectra were both obtained using a droplet diameter of 30 µm. Also shown is a spectrum obtained using a 10-µm CO_2 laser that represents the case of small optical depth (reproduced from Ref. [111]).

Scaling of peak optical depth with droplet size and drive laser wavelength: all results

Having demonstrated the ability of the model function to accurately reproduce spectra from a single reference spectrum, we show in Fig. 3.6(a) the fitted values for all spectra of the droplet size scans for 1- and 2-µm laser wavelength. In all cases the peak optical depth $\tau_{i,p}$ appears to linearly increase with droplet diameter and to strongly depend on the laser wavelength. Indeed, the peak optical depth of the 2-µm-driven plasma lies roughly a factor of 2 below that of the 1-µm one at largest droplet size, which may be expected from the lower plasma density (cf. Section 3.3). However, the 1-µm results were obtained with 10-ns-long pulses and are here compared to the results from approximately 5-ns-long, 2-µm pulses, and optical depth is known to increase with pulse length [16, 51]. To provide a comparison on more equal footing, we further compare in Fig. 3.6(a) our results to previous data [51], obtained using a 1-µm wavelength laser with a 5 ns temporally box-shaped laser pulse. One of these data sets is taken with a spatially flattop laser profile of 96-µm diameter [16, 51] while the other one is taken with a Gaussian laser beam profile of 66 µm FWHM which more closely resembles the experimental conditions for the 2-µm driver case. The spatial intensity distribution of the 1-µm laser beam is seen to impact the effective optical depth (see also Ref. [16]). On comparison of the spectra for the 2- and 1-µm cases at the most comparable temporal and spatial beam conditions, the clear reduction in peak optical depth parameter is maintained. This reduction, up to a factor 1.6 in optical depth, becomes more pronounced at larger droplet diameters. The small deviation from the factor of ~2 from the $\rho \propto \lambda^{-1}$ scaling may originate from differences in plasma length scales, plasma temperature, or from the finite laser intensity gradient over the

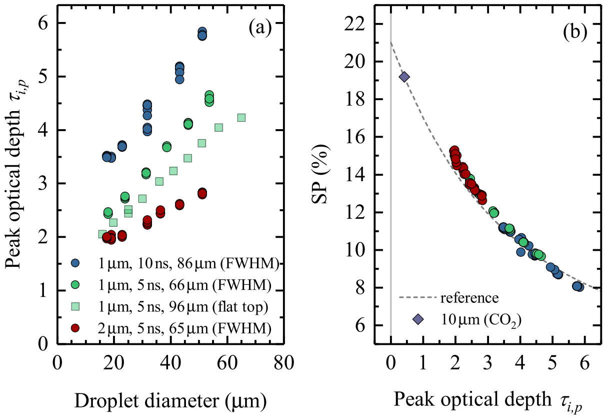

Figure 3.6: (a) Dependency of peak optical depth $\tau_{i,p}$ on droplet diameter for 5- and 10-ns laser pulse duration at 1-μm wavelength and for 4.3-ns pulse duration at 2-μm wavelength. Circles indicate Gaussian spatial laser profile and boxes indicate a homogeneous ’flattop’ laser beam profile. Peak optical depth is fitted with respect to the spectrum obtained at 1-μm wavelength, 10-ns pulse duration and 30-μm droplet diameter with optical depth of $\tau_{0,p} = 4.5$. (b) Experimental values for spectral purity (SP) versus peak optical depth. The dashed line represents SP as calculated from the radiation-transported reference spectrum. The diamond symbol indicates the SP value of the radiation-transported reference spectrum for a peak optical depth value $\tau_{i,p} = 0.4$, obtained from comparison of the reference spectrum with the emission of the CO_2-laser-driven plasma spectrum illustrated in Fig. 3.4.

plasma length scale. Nevertheless, a very significant reduction in optical depth of up to 40% is demonstrated when using a 2-μm laser to drive the plasma.

With peak optical depth being the pertinent scaling parameter of 1- and 2-μm-driven tin plasmas the corresponding spectral purity of the emission spectrum is related to it in Fig. 3.6(b). All experimental SP values, calculated over the range of 5.5–25.5 nm, collapse onto the gray dashed curve obtained by calculating the SP of the radiation-transported reference spectrum. The 2-μm case is slightly offset towards higher SP values because of the reduced emission in the 7–12 nm wavelength band compared to the radiation transported reference spectrum (cf. Fig. 3.5) that is not captured by the model with the same accuracy as that of the main emission feature at 13.5 nm. This difference between model and experiment may point to a small overestimation of the optical depth of the 2-μm-laser-produced tin plasma, which would explain both the observed overestimation of the short-wavelength out-of-band emission by the model as well as the offset in Fig. 3.6(b). This small overestimation of the optical depth may in turn be due to a broader charge state distribution in our measurements of the 2-μm case caused by, e.g., laser intensity gradients or the slightly lower beam pointing stability compared to the 1-μm case. This observation leads us to expect an even lower optical depth in the 2-µm case and brings our scaling ratio even closer to the expected factor of 2 from the λ^{-1} scaling. More importantly, it indicates that there are further opportunities for narrowing the charge state distribution by providing a more homogeneous heating of the plasma in time and space. Such a narrowing of the charge state distribution around the optimum charge states Sn^{11+}–Sn^{14+} would lead to further improvements of SP and thus CE.

3.5 Conclusions

In conclusion, the effects of optical depth, plasma density, and laser intensity on the emission spectra of a 2-µm-LPP source of tin microdroplets are investigated. The results are compared to the case of a 1-µm-driven plasma. It is found that the laser intensity required to maintain a common plasma temperature, scales approximately inversely with laser wavelength in going from a 1- to a 2-µm drive laser, a result that will help defining development goals for future 2-µm drive lasers for LPP light sources. The reciprocal scaling with laser wavelength ($\propto\lambda^{-1}$) has its origin in Kramers' law of inverse bremsstrahlung, the main laser absorption mechanism in the tin plasmas investigated. Because of its reduced plasma density, the optical depth of the 2-µm-driven plasma is significantly reduced, allowing for efficient out-coupling of 13.5-nm radiation from the plasma even at larger plasma sizes. In future experiments it will be of interest to use large, preformed targets and investigate the full CE potential of a 2-µm source in a setting more similar to the current industrial one. Our results indicate that there are further opportunities for narrowing the charge state distribution by providing a more homogeneous heating of the plasma in time and space which would lead to further improvements of SP and thus CE. Looking further, it is of interest to experimentally investigate plasma generation using even longer-wavelength laser systems between 2 and 10 µm to find the mid-infrared wavelength optimally suited to drive EUV light sources at 13.5 nm.

Acknowledgements

We thank Mikhail M. Basko for providing us with the RALEF-2D code and his advise aiding the simulation work presented in the paper. Further we thank the authors of Ref. [111] for providing us with the data for the CO_2 spectrum shown in Fig. 3.5. This work has been carried out at the Advanced Research Center for Nanolithography (ARCNL), a public-private partnership of the University of Amsterdam (UvA), the Vrije Universiteit Amsterdam (VU), the Netherlands Organisation for Scientific Research (NWO) and the semiconductor equipment manufacturer ASML. The used transmission grating spectrometer has been developed in the Industrial Focus Group XUV Optics at University of Twente, and supported by the FOM Valorisation Prize 2011 awarded to F. Bijkerk and NanoNextNL Valorization Grant awarded to M. Bayraktar in 2015. This project has received funding from European Research Council (ERC) Starting Grant number 802648 and is part of the VIDI research programme with project number 15697, which is financed by NWO.

3.A Appendix

Radiation transport model

To determine peak optical depth in this work, the recorded spectra are analyzed in a manner similar to that presented in Ref. [51]. In the following, the method from Ref. [51] is first outlined briefly and is subsequently generalized for use with plasmas that are optically thin. The wavelength-dependent optical depth $\tau_\lambda := \int \kappa_\lambda \rho dx$ is defined as the spatial integration over the product of the plasma's opacity κ_λ and mass density density ρ. The spectral radiance L_λ of an extended one-dimensional plasma can be calculated by means of its optical depth as [60]

$$L_\lambda = S_\lambda \left(1 - e^{-\tau_\lambda}\right). \tag{3.4}$$

In local thermodynamic equilibrium (LTE), where collisional processes drive atomic level populations, the source function S_λ equals the Planck blackbody function B_λ. Rearranging Eq. (3.4), the optical depth of the recorded plasma spectrum can be obtained from its relative spectral radiance L_λ / B_λ

$$\tau_\lambda = -\ln\left(1 - \frac{L_\lambda}{B_\lambda}\right). \tag{3.5}$$

The optical depths of two plasmas of similar temperatures, but with modestly different densities and length scales, may differ (in first approximation) only by a single wavelength-independent multiplicative factor a_i, relating the plasmas' optical depths via $\tau_{\lambda,i} = a_i \, \tau_{\lambda,0}$. Here τ_0 and τ_i are the two wavelength-dependent optical depths of the reference spectrum and any other spectrum i, respectively. The relative spectral radiances of these two plasmas can be related to each other via Eq. (3.5)

$$\frac{L_{\lambda,i}}{B_\lambda} = 1 - \left(1 - \frac{L_{\lambda,0}}{B_\lambda}\right)^{\tau_i/\tau_0}. \tag{3.6}$$

In order to apply Eq. (3.6) to the spectra measured, the relative spectral radiance of the spectra must be known. To obtain the relative spectral radiance, the ratio of observed spectrum O_λ (meaning the spectrum as recorded with the spectrometer) and blackbody function is normalized to the peak value at 13.5-nm wavelength (subscript p) by replacing L with $\tilde{L}_\lambda = O_\lambda B_p / O_p$. The normalized ratio $\tilde{L}_\lambda / B_\lambda$ is then multiplied by the amplitude factor $1 - e^{-\tau_p}$ obtained from Eq. (3.5)

$$\frac{\tilde{L}_{\lambda,i}}{B_\lambda} = \frac{1 - \left(1 - \frac{\tilde{L}_{\lambda,0}}{B_\lambda}(1 - e^{-\tau_{0,p}})\right)^{\tau_{i,p}/\tau_{0,p}}}{1 - e^{-\tau_{i,p}}}. \tag{3.7}$$

Note that the wavelength-dependent optical depth values ($\tau_{0,\lambda}$) from Eq. (3.6) have been exchanged by their peak values ($\tau_{0,p}$). This generalized equation allows for determination of peak optical depth in optically thin plasmas in LTE if the peak optical depth of one of the spectra is known. In the current analysis the use of Eq. (3.7) results in optical depth values that are mostly very similar, but some of which are up to 25% lower for the smallest optical depths cases ($\tau \sim 2$), than when using Eq. (3.6). Using Eq. (3.7) the peak optical depths $\tau_{i,p}$ of all spectra are fitted with respect to a reference spectrum of known peak optical depth (see main text).

CHAPTER 4

CHARACTERIZATION OF ANGULARLY RESOLVED EUV EMISSION FROM 2-µm-WAVELENGTH LASER-DRIVEN SN PLASMA USING PREFORMED LIQUID DISK TARGETS

R. Schupp, L. Behnke*, Z. Bouza, J. Sheil, M. Bayraktar, W. Ubachs, R. Hoekstra, and O. O. Versolato

Journal of Physics D: Applied Physics **54**, 365103 (2021).

The emission properties of tin plasmas, produced by the irradiation of preformed liquid tin targets by several-ns-long 2-µm-wavelength laser pulses, are studied in the extreme ultraviolet (EUV) regime. In a two-pulse scheme, a pre-pulse laser is first used to deform tin microdroplets into thin, extended disks before the main (2 µm) pulse creates the EUV-emitting plasma. Irradiating 30- to 300-µm-diameter targets with 2-µm laser pulses, we find that the efficiency in creating EUV light around 13.5 nm follows the fraction of laser light that overlaps with the target. Next, the effects of a change in 2-µm drive laser intensity (0.6–1.8×10^{11} W/cm^2) and pulse duration (3.7–7.4 ns) are studied. It is found that the angular dependence of the emission of light within a 2% bandwidth around 13.5 nm and within the backward 2π hemisphere around the incoming laser beam is almost independent of intensity and duration of the 2-µm drive laser. With increasing target diameter, the emission in this 2% bandwidth becomes increasingly anisotropic, with a greater fraction of light being emitted into the hemisphere of the incoming laser beam. For direct comparison, a similar set of experiments is performed with a 1-µm-wavelength drive laser. Emission spectra, recorded in a 5.5–25.5 nm wavelength range,

---

[*] LB designed and set up the 2-µm laser, and equally contributed to planning, preparing and conducting experiments, and operation of lasers

show significant self-absorption of light around 13.5 nm in the 1-µm case, while in the 2-µm case only an opacity-related broadening of the spectral feature at 13.5 nm is observed. This work demonstrates the enhanced capabilities and performance of 2-µm-driven plasmas produced from disk targets when compared to 1-µm-driven plasmas, providing strong motivation for the use of 2-µm lasers as drive lasers in future high-power sources of EUV light.

4.1 Introduction

Laser-produced plasmas containing highly charged tin ions are the light source of choice for state-of-the-art extreme ultraviolet (EUV)lithography [39, 40, 42, 44, 53, 71, 97–99, 112, 113]. Tin is used because no less than five of its charge states (Sn^{10+}–Sn^{14+}) strongly emit, with large amounts of atomic transitions clustered in so-called unresolved transition arrays (UTAs) [114], in a narrow band around 13.5 nm [45–50, 82, 84, 100–102] that matches the peak reflectivity of available multilayer optics [103, 104]. These emission characteristics enable a high conversion efficiency (CE) of drive laser light into *in-band* radiation into the backward hemisphere towards the laser origin, with in-band radiation defined as radiation in a 2% bandwidth centered at 13.5 nm. The tin ions are bred in a hot (~30–60 eV) and dense (10^{19}–10^{21} e^-/cm^3) plasma. Starting from mass-limited tin-microdroplets, a low intensity *pre-pulse* (PP) deforms the droplets into a shape better suited for interaction with a second high-intensity *main pulse* (MP), used to create the EUV-emitting plasma. This two-step process is crucial for reaching source efficiencies and power levels that allow for the industrial utilization of EUV lithography [61, 77, 115, 116]. Currently, 10.6-µm-wavelength CO_2 gas lasers are used to drive the plasma, achieving CE values of up to 6% [40]. Recent simulation studies however have drawn significant attention to the use of a 2-µm main pulse, a wavelength at which high-power solid-state lasers may soon become available [59]. These simulation results show that CE values of the 2-µm driven plasmas may be on par with the ones of 10-µm driven plasmas, at which point the expected higher wall-plug efficiency [58] of near- to mid-infrared solid state over gas lasers may make for an overall more efficient EUV source using the shorter 2 µm wavelength.

Shorter drive laser wavelengths have the additional advantage of a higher coupling efficiency of laser light with the tin plasma. The scaling of the here relevant inverse bremsstrahlung absorption coefficient $k_\mathrm{L} \propto \lambda^2 n_e^2$, with wavelength λ and electron density n_e indicates that shorter wavelength light is absorbed less efficiently at equal plasma density but because of the higher critical electron density ($n_\mathrm{c} \propto \lambda^{-2}$), the shorter wavelength laser light can penetrate into denser plasma regions leading to an overall increased absorption of the laser light, with the aborption taking place in regions of higher emitter and absorber density. This may benefit the obtainable source brightness but an associated increase in optical depth [32, 51] leads to increased broadening of spectral features outside the in-band region relevant for EUV lithography. This broadening may limit the obtainable CE. Limitations on the spectral performance of EUV sources imposed by optical depth have been studied in detail for plasmas driven by 1-µm Nd:YAG lasers [16, 51, 54]. A 2-µm wavelength, between the widely investigated 1 and 10 µm, is an interesting candidate providing intermediate plasma densities and hence optical depth. In addition to 2-µm systems based on difference frequency generation [15, 22, 32], high-power Big Aperture Thulium (BAT) laser systems, operating at 1.9-µm wavelength, are currently under development [5, 6].

Despite its importance for EUV lithography, literature on the production of in-band radiation from mass-limited, pre-pulse deformed targets remains rather scarce, with the majority of studies to-date focusing on $\lambda = 10\,\mu\mathrm{m}$ main pulses (see, e.g., [116–119]). A broad body of literature has investigated experimentally the emission from undeformed liquid tin droplet targets [16, 71, 89, 120], coated spheres [72] or solid-planar targets [52, 87, 88, 121] using 1-µm solid-state lasers. First results from experiments using 2-µm laser light driving plasma from solid-planar tin targets [15] as well as from undeformed liquid tin droplet targets [32] have recently been presented. Both works demonstrate the potential of the 2-µm drive wavelength, showing a doubling of the obtainable CE over the 1-µm driver, to a 3% level for the solid-planar tin target. At this 3% level the overall conversion efficiency of wall plug power to in-band EUV may be at par with the current CO_2-driven industrial solutions. Literature on industrially-relevant mass-limited deformed targets interacting with either 1- or 2-µm main pulse beams at high CE is however not yet available.

In this publication, EUV light production from mass-limited tin targets, suitably shaped by a 1-µm laser pre-pulse, is investigated using 1- and 2-µm main pulse laser systems to drive the plasma. First, plasma produced with a 2-µm laser beam is investigated for three different laser intensities and three laser pulse durations. For each laser parameter set a wide range of target diameters (30–300 µm) is investigated and the resulting angular distribution of in-band emission, the efficiency of converting laser light into in-band EUV radiation and overall EUV radiation, as well as the spectral performance of the plasma, are characterized. Secondly, plasmas generated by 1- and 2-µm drive laser light are characterized and compared.

4.2 Method

In the experiments, micrometer-sized liquid tin droplets are first irradiated with a relatively low intensity ($\sim 10^9\,\mathrm{W\,cm^{-2}}$), 1-µm wavelength PP (see Fig. 4.1(a)) from an Nd:YAG laser. The PP propels the droplets and deforms them into extended, disk-like targets of diameter d_T [122–125] with typical radial expansion speeds of $\sim 90\,\mathrm{m\,s^{-1}}$.

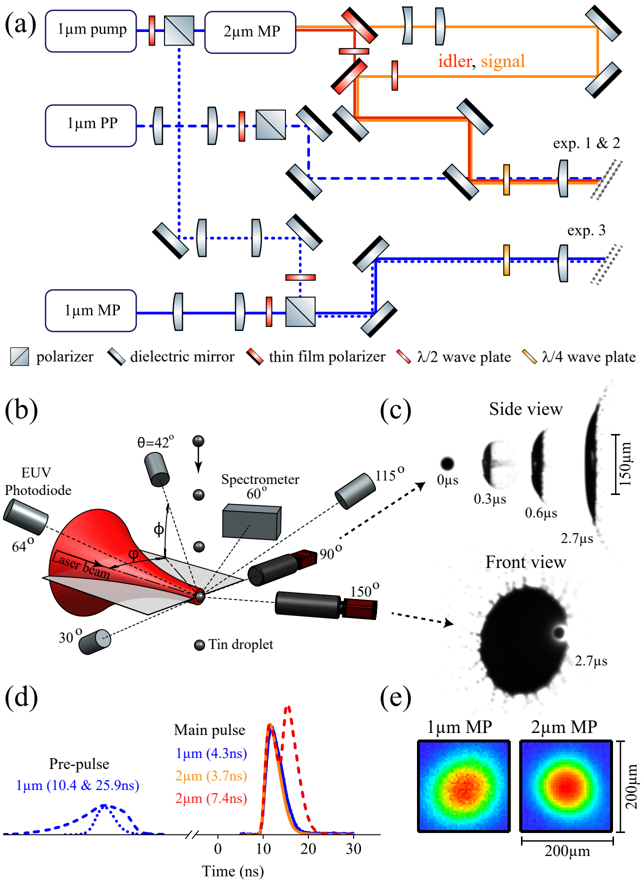
(a)
1µm pump
2µm MP
idler, signal
1µm PP
exp. 1 & 2
exp. 3
1µm MP
polarizer
dielectric mirror
thin film polarizer
λ/2 wave plate
λ/4 wave plate
(b)
θ=42°
EUV Photodiode
64°
Spectrometer 60°
115°
90°
150°
30°
ϕ
φ
Laser beam
Tin droplet
(c)
Side view
0µs
0.3µs
0.6µs
2.7µs
150µm
Front view
2.7µs
(d)
Main pulse
1µm (4.3ns)
2µm (3.7ns)
2µm (7.4ns)
Pre-pulse
1µm (10.4 & 25.9ns)
0
10
20
30
Time (ns)
(e)
1µm MP
2µm MP
200µm
200µm

Figure 4.1: (a) Schematic representation of the laser beam setups for experiments 1 & 2 and experiment 3 with pre-pulse (PP) and main pulse (MP) lasers shown. (b) Continuation from (a) showing the locations and angles of the detectors. All angles θ are calculated with respect to the laser-beam propagation axis, with $\cos\theta = \cos\phi\cos\varphi$. (d) Selection of front and side view shadowgraphs of the tin targets used for plasma generation, recorded by the two cameras indicated in (b). (d) Temporal and (e) spatial profiles of the laser beams. For more detail see text.

The target diameter is precisely controlled via the time delay between pre- and main pulse, which ranges 0–3 µs. In all measurements concerning 2-µm main pulses, the spatial beam profile of this PP laser is Gaussian with a size of 120 µm at full width at half maximum (FWHM) and a FWHM duration of 25.9 ns (see Fig. 4.1(d)). A constant PP energy of 8.4 mJ is used throughout the experiments. We use circular polarization, to ensure that the produced targets are radially symmetric [124, 126]. The produced tin targets are observed under angles of 90° (side view) and 150° (front view) with respect to the laser beam using combinations of CCD cameras and long-distance microscopes (see Fig. 4.1(b)). Temporal resolution is achieved by back-lighting the tin targets with spatially and temporally incoherent 560-nm-wavelength pulses of 6 ns duration. Examples of typical targets are shown in Fig. 4.1(c).

After a set time delay the targets are irradiated with high-intensity 2-µm-wavelength laser pulses. The pulses are produced in a master oscillator power amplifier (MOPA) [15, 32] that was built following the work of Arisholm *et al.* [22]. Signal and idler pulses having energies up to 180 mJ each are produced at wavelengths of 1.9 and 2.1 µm, respectively. Depending on the precise experimental conditions, the pulse duration of the MOPA system can vary between 3.7 to 4.6 ns, and the exact, measured pulse durations are stated for each measurement in the following.

For the first set of experiments, the signal beam is removed via polarization optics and only the idler beam of the MOPA is focused onto the tin targets while scanning laser intensity and target size. The focal spot of the idler beam is Gaussian and has a FWHM of 106 µm (see Fig. 4.1(e)).

In a second set of experiments, the pulse duration of the 2-µm beam is varied between 3.7 ns (idler only) and 7.4 ns (idler and signal) at equal laser intensity. To achieve the longer pulse duration, the signal beam, which is separated from the idler via a thin film polarizer (TFP), is sent into an optical delay line of 1.2 m length. The focusing conditions of the delayed signal beam are matched to those of the idler by adjustment of beam size and collimation via a telescope within the delay line, resulting in a Gaussian focal spot size of 106 µm FWHM for both beams. After collimation adjustment the beams are combined again with a second TFP. The signal energy is adjusted via a $\lambda/2$-waveplate before this second TFP.

To enable a direct comparison of plasmas driven by 1- and 2-µm-wavelength laser pulses, a separate and final set of experiments is conducted where the 1-µm beam of a third laser system is used as MP (lower part of Fig. 4.1(a)). This 1-µm MP laser is a seeded Nd:YAG laser with arbitrary temporal pulse-shaping capabilities [81] that are used to reproduce the temporal profile of the 4.3 ns and the 7.4 ns 2-µm beam. The pump laser of the MOPA is used for pre-pulsing in this third set of experiments. The PP parameters are tuned to obtain similar radial expansion speeds as in experiments 1 and 2 and no significant change in EUV emission is observed when using either

PP. Using telescopes, 1-µm PP and MP are adjusted in size and collimation. For the MP a symmetric, 90-µm-sized focal spot is achieved close to the dimensions of the 2-µm MP. The PP has a spot size of 100 µm and a pulse duration of 10.4 ns. PP and MP are combined via a polarizing beam cube at which their pulse energy is adjusted via a preceding $\lambda/2$-waveplate. Consecutively, the combined beams are steered onto the droplet, passing a $\lambda/4$-waveplate just before the final focusing element. The latter changes the polarization of the beams from linear to circular, ensuring a symmetric deformation of the tin droplets by the PP laser as before. Laser intensity is calculated with respect to its peak in space and time according to $I_\mathrm{L} = (2\sqrt{2\ln 2/2\pi})^3 E_\mathrm{L}/abt_\mathrm{p}$, where E_L is the laser energy, a and b are the major and minor axis of the slightly elliptical beam given as FWHM, and t_p is the pulse duration.

The spectral emission from the plasma is recorded using a transmission grating spectrometer [80]. The spectrometer is mounted at an angle of 60° with respect to the laser axis (see Fig. 4.1(b)) and is operated with a 25 µm slit and a 10 000 lines/mm grating. Subsequent to recording the spectra with a CCD camera, a dark exposure is subtracted from the images in order to account for thermal and readout counts on the CCD. Next, spectra are corrected for second order diffraction from the grating, the grating's first order diffraction efficiency and the quantum efficiency of the CCD.

The absolute amount of in-band radiation is measured with four photodiode assemblies installed under angles of $\theta = 30, 42, 64$ and $115°$ with respect to the target's surface normal. The photodiode assemblies use a multilayer mirror near normal incidence to reflect the in-band light onto the photodiode detectors. Remaining optical radiation is filtered by an EUV-transmissive Si/Zr coating on the photodiodes. Next, following the approach of Ref. [16] (and analogously to [87] and [78]) the measured in-band energy values are corrected for the respective solid angle and fitted with the monotonous smooth function

$$f(\theta) = (\alpha - \beta)\cos(\theta/2)^\gamma + \beta, \tag{4.1}$$

with amplitude α, offset β and power γ. We note that this function differs from the fit function $\sim\cos(\theta)^\gamma$ used in Schupp *et al.* [16]. The adaption is needed to capture the emission under angles $\theta > 90°$ also in cases $\gamma < 1$. The resulting fitted curves, using either fit function, are found to be indistinguishable over the backward hemisphere where $\theta < 90°$. The integral amount of in-band radiation over the hemisphere around the incoming laser beam is then calculated by integration of Eq. (4.1)

$$E_{\mathrm{IB},2\pi} = 2\pi \int_0^{\pi/2} f(\theta)\sin\theta d\theta. \tag{4.2}$$

Using this value, CE is defined as $E_{\mathrm{IB},2\pi}/E_\mathrm{L}$. We further define an anisotropy factor of the in-band emission to gauge which fraction of in-band light is emitted into the backward hemisphere via $E_{\mathrm{IB},2\pi}/E_{\mathrm{IB},4\pi}$, where $E_{\mathrm{IB},4\pi}$ is obtained by changing the upper integration boundary in Eq. 4.2 to π, hence integrating over all angles. A large anisotropy factor is favorable for industrial application as light-collecting optics typically cover the backward hemisphere.

A second measure for source performance is the spectral purity (SP), defined as the ratio of in-band energy to the total EUV energy. All SP values provided in the following are calculated with respect to the spectral range of 5.5–25.5 nm measured under a 60 degree angle. A third measure, the radiative efficiency η_{rad} of the plasma is defined as the ratio of CE over SP following Ref. [16] and yields the total amount of EUV light emitted in the 5.5–25.5 nm wavelength band per incoming laser energy. In the current work, and in contrast to Ref. [16], η_{rad} is defined using the values measured at 60°, i.e., using the in-band EUV energy emitted per steradian under an angle of 60° (this value is subsequently multiplied with 2π), meaning $(E_{\mathrm{IB},60^\circ}/E_{\mathrm{L}})/\mathrm{SP}$, instead of using CE that is defined over the entire laser-facing hemisphere. This is undertaken because the spectra and hence the SP values are expected to show strong angular dependence for expanded targets [56, 88], a dependence that is further expected to be influenced by the target diameter.

4.3 EUV generation using 2-μm light on preformed targets

In the following, the influence of target diameter, laser intensity and laser pulse duration on CE, SP, η_{rad}, $E_{\mathrm{IB},2\pi}$ and $E_{\mathrm{IB},2\pi}/E_{\mathrm{IB},4\pi}$ are investigated. Further, the spectral emission and angular distribution of the in-band emission are discussed.

4.3.1 Target diameter

To investigate the influence of target size, tin targets of various sizes as produced from pre-pulse-impacted 27-μm-diameter droplets are irradiated with laser pulses having an intensity of 0.6×10^{11} W cm^{-2} and a pulse duration of 4.5 ns (downward triangles in Fig. 4.2). Data recorded using higher laser intensities and different pulse lengths are also shown but will be discussed in Sections 4.3.2 and 4.3.3, respectively. Starting from an undeformed droplet target, CE has a low value of approximately 0.15% that almost linearly increases with target diameter (see Fig. 4.2(a)). At diameters of 170 μm and above, CE starts to plateau at a value of approximately 2.6%. This plateau sets in where the target is roughly a factor of 1.5–2 larger than the FWHM size of the beam. A similar result was observed for 1-μm-driven plasmas from tin coated glass spheres by Yuspeh *et al.* [127].

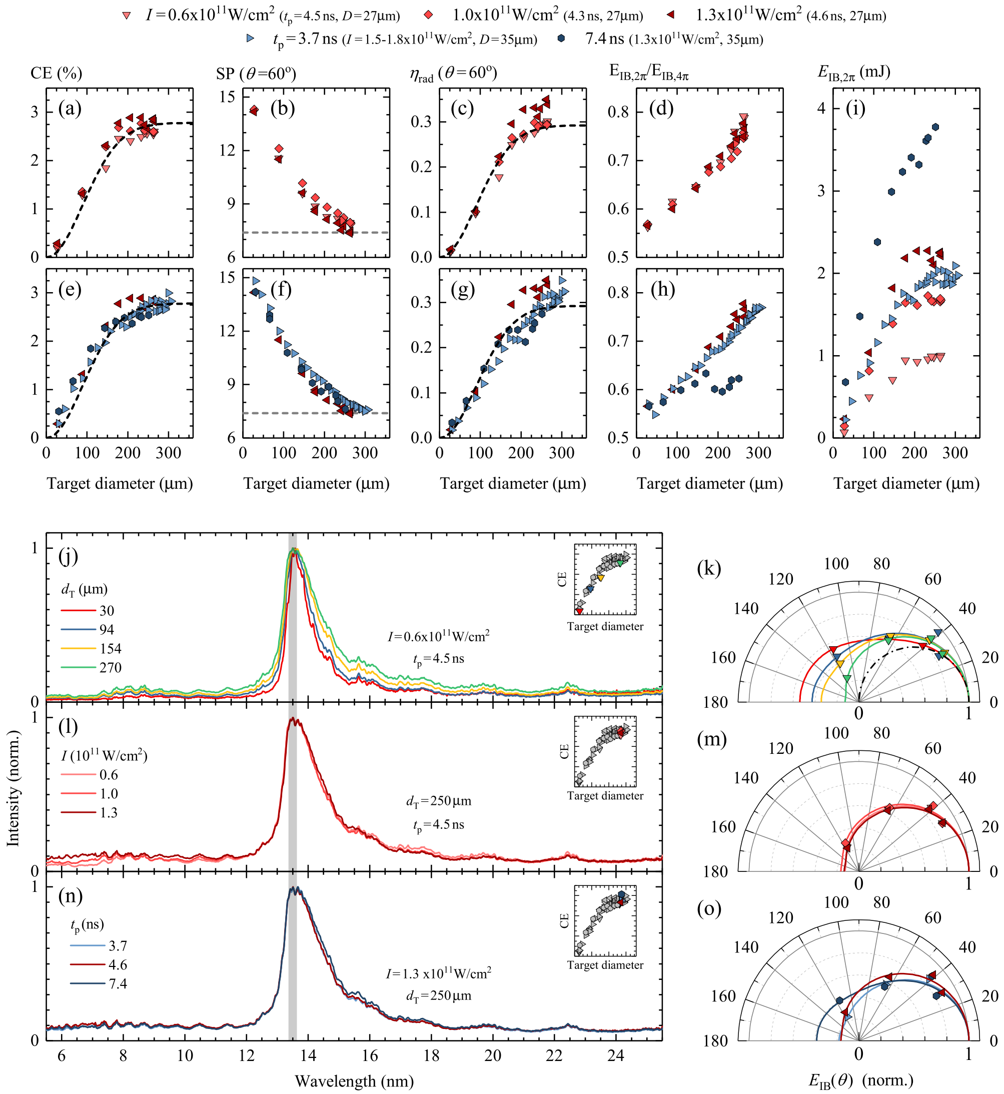

Figure 4.2: Results obtained with a 2-µm drive laser wavelength. Panels (a), (e) depict CE; (b), (f) SP; (c), (g) η_{rad}; (d), (h) anisotropy factor $E_{\text{IB},2\pi}/E_{\text{IB},4\pi}$; and (i) $E_{\text{IB},2\pi}$, as function of target diameter, for three different intensities and laser pulse durations. SP and η_{rad} are obtained from measurements of the spectrum and in-band energy under a 60° angle. During the intensity scans the idler beam had a slightly longer pulse duration of 4.5 ns (cf. 3.7 ns during pulse duration scan) and the 1.3×10^{11} W cm^{-2} scan is shown in the pulse duration scan also. The dashed lines in panels (a), (c), (e), and (g) represent the results of a fit of the geometrical overlap of laser beam and target (EoT). The gray dashed lines in (b) and (f) indicate the SP values from measurements on planar-solid tin targets obtained from [15]. Also shown are normalized spectra versus (j) target size, (l) laser intensity and (n) pulse duration. The corresponding angular dependence of in-band emission, normalized at 0°, is shown in panels (k), (m) and (o). The solid lines depict fits of Eq. (4.1) to the data; the dash-dotted line in (k) indicates the cos(θ) dependence of the Lambert cosine law.

An increase in CE with target diameter is expected as an enlarged target diameter increases the geometrical overlap of laser beam and target. This overlap fraction is referred to as energy-on-target (EoT, following the definition in Refs. [122] and [123]). We note that there is a near complete absorption of laser light by the efficient inverse bremsstrahlung mechanism for this wavelength laser light at the here-relevant intensities [123], where laser light geometrically overlaps with the target. For a circular spot, EoT is given by the function $A(1-2^{-d_\mathrm{T}^2/d_\mathrm{L}^2})$ which is an excellent approximation for the current focal spot shapes (cf. Fig. 4.1(e)), where $d_\mathrm{L}=(a+b)/2$ and a and b are similar to within a few percent. The free fit factor A, the amplitude of the EoT curve, is obtained from a global fit to the asymptotic CE value of all data presented in Fig. 4.2(a) and 4.2(e). The observed dependence of CE on target size is seen to be well approximated by the geometric overlap function (dashed line in Fig. 4.2(a)).

All CE values are calculated from angular-resolved measurements of the plasma's in-band emission and all data points represent the mean over 300 individual laser shots. The angular dependence of the measured in-band energies (see Fig. 4.2(k)) is first fitted with Eq. (4.1) and the CE value is subsequently calculated using the integration result from Eq. (4.2). For better visibility, all curves in Fig. 4.2(k) are normalized at 0°. Eq. (4.1) is seen to accurately describe the angular dependence of the in-band EUV emission. The increase of in-band light observed at a target diameter of 94 μm and under an angle of 42° is however not fully captured by the fit function and this data point may in fact be an outlier.

The reduced emission in the propagation direction of the laser at 180° with increasing target size may be caused by the one-sided heating of the expanded tin target by the laser beam. Plasma emission in this direction is shielded by the target (which is still thought to be present in liquid form during the laser pulse) and only plasma formed on the edge of the target presumably contributes to in-band emission under angles larger than 90°. The dashed line in Fig. 4.2(k) shows Lambert's cosine law for the angular emission from a planar surface. With increasing target diameter the in-band emission starts to converge to this $\cos(\theta)$ dependence, however without fully reaching it. This might be expected because of the 3-dimensional extent of the plasma, causing departure of the emission characteristics from a Lambert-type distribution. Furthermore, emission will always exist at angles larger than 90° from the edge of the plasma unless $d_\mathrm{T} \gg d_\mathrm{L}$.

Next, the angular in-band distribution is quantified via an anisotropy factor, defined as the ratio of $E_{\mathrm{IB},2\pi}/E_{\mathrm{IB},4\pi}$, meaning the fraction of *all* in-band energy that is emitted into the backward hemisphere of the incoming laser beam, relevant for EUV lithography applications. The anisotropy factor starts at a value of 0.57 for the droplet target, where 0.5 indicates an equal split between both hemispheres (see Fig. 4.2(d)). The anisotropy factor then linearly increases with target diameter up to a value of 0.79, meaning that an ever-larger fraction of the in-band EUV is emitted into the backward hemisphere.

The in-band energy emitted in the 2π hemisphere towards the laser (obtained from multiplying the CE with the laser pulse energy) is shown in Fig. 4.2(i). Naturally, the same trends are observed as in the case of CE. A maximum of ~1 mJ of in-band EUV energy is produced (per laser shot) for this lowest intensity case.

Fig. 4.2(j) depicts spectra from the lowest intensity case for a succession of four target diameters. For visibility and ease of comparison the spectra are normalized to their respective maximum values. Similar to previously published work, where a 2-µm laser was used to produce plasma from spherical, undisturbed droplet targets [32], all spectra show a strong emission feature at 13.5 nm originating from transitions in Sn^{8+}–Sn^{14+} ions [44]. Transitions in these charge states further lead to the radiation observed in the 6–12 nm wavelength region [83]. With increasing target diameter, the feature at 13.5 nm widens significantly from 0.8 to 1.5 nm (FWHM). These are values between those of 1-µm-driven low-density plasmas from planar SnO_2 targets of 0.5–1.5 nm [121, 128] and plasmas from solid-planar tin targets of typically 2–3 nm [56]. In Ref. [16] a FWHM of 0.9 nm was reached in the case of a 1-µm-driven plasma on a tin microdroplet target. 10-µm laser-driven tin plasmas typically have a narrower 13.5-nm feature, reaching 0.6 nm (FWHM) [111]. The 2-µm-driven plasma is thus seen to produce spectra with spectral widths typically in between those produced with 1- and 10-µm laser-driven pure tin plasmas.

In contrast to the scaling of CE, SP has its maximum at the smallest target diameter. The highest value shown in Fig. 4.2(b) is 11.5% at a 90 µm diameter down from a maximum value of ~14% for the case of an undeformed droplet. SP for the undisturbed droplet target for this lowest intensity case is omitted from Fig. 4.2(b) due to the low signal-to-noise ratio in the recorded spectrum. With increasing target diameter SP is observed to decrease monotonously, an effect previously observed for 1-µm beams on droplet targets [16]. Above 200 µm diameter the decrease in SP plateaus towards a value of 7.5% at a 260 µm diameter. These SP values are consistent with Ref. [15], where the SP for planar-solid tin target plasmas was measured at 7.4% (dashed line in panel (b)).

Using these SP values as input, a monotonic increase of η_{rad} with target diameter is observed up to a value of ~0.3 at a 260 µm target diameter (cf. Fig. 4.2(c)). Also indicated is the dependence of EoT on target size, now with an amplitude fit value of 0.29 (dashed curve). The here measured maximum radiative efficiency at 60° is slightly lower than a value of approximately 0.4 measured for an extended solid-planar target [15]. This difference originates from the slightly higher in-band emission at 60° measured on the planar target and may be explained by the smaller beam-spot size in the planar target case that allows for the in-band emission to escape more freely. Over the entire range of target diameters, the radiative efficiency qualitatively follows the

EoT trend.

At this point, it is worthwhile to consider the fact that both overall CE and η_{rad} qualitatively follow the EoT curve, describing the increasing geometrical overlap between an enlarging target and laser beam spot. However, we also note that the SP, which serves as input for calculating η_{rad}, monotonically decreases with increasing target size. This apparent contradiction is resolved when considering the angular dependence of the plasma emission, with the increasing anisotropy factor serving to offset the decrease in SP with increasing target size (cf. Fig. 4.2(b) and 4.2(d)).

4.3.2 Laser intensity

Next, target diameter scans are performed for two higher laser intensities of 1.0 and $1.3{\times}10^{11}$ W cm^{-2}. The CE curves for all three laser intensities show a trend very similar to the 0.6×10^{11} W cm^{-2} intensity case presented in Sec. 4.3.1 (see Fig. 4.2(a)). For all target diameters, CE values are found to be slightly higher at higher laser intensities. The maximum CE value at large target diameters increases modestly from 2.6 to 2.9%. The angular distribution of in-band emission is observed to be independent of laser intensity within the scanned range (cf. Fig. 4.2(m)). Given the constant maximum CE values, the amount of in-band radiation increases linearly with increasing laser intensity, with up to 2.3 mJ of in-band light obtained for the highest intensity case (see Fig. 4.2(i)).

In Fig. 4.2(l) normalized spectra for a target diameter of 250 μm are shown. For all spectra, the 8–25 nm region looks remarkably alike. The most prominent difference between the spectra is seen in the 5–8 nm region where the amount of radiation is observed to increase with increasing laser intensity. This emission could stem from charge states Sn^{14+} (and above) as well as from an increased fraction of light being emitted from electronic states having higher excitation energies. The corresponding SP values are shown in Fig. 4.2(b). All laser intensity cases follow the same trend. The maximum SP value for the two higher intensities is 14.5% and is reached at the smallest target diameter, i.e., the undeformed droplet target. SP steadily decreases with increasing target size, and levels off at a value of up to 8% depending on intensity. Even though the differences in SP are small, we do note that optimum SP values are observed for an intermediate intensity of 1.0×10^{11} W cm^{-2}.

Given the similar scaling of CE and SP with target diameter for the three laser intensities, the radiative efficiency in Fig. 4.2(c) closely follows the 0.6×10^{11} W cm^{-2} results, with a slightly higher value of 0.35 obtained for the highest intensity case.

No significant changes are thus observed in the scaling of emission characteristics with target size when changing laser intensity and in-band EUV emission is seen to exhibit a linear dependence on laser energy.

4.3.3 Pulse duration

Lastly, the laser pulse duration is varied from 3.7 to 7.4 ns (blue markers in Fig. 4.2) by combining signal and idler beams while delaying the signal with respect to the idler pulse. To obtain identical focal spot conditions for both beams, the beam size of the signal beam is carefully matched to that of the idler beam by means of a telescope. The energy of both beams is individually controlled via combinations of $\lambda/2$-plates and TFPs. Signal and idler beams are set to have equal energies. The resulting temporal pulse profile is shown in Fig. 4.1(d). Measurements are taken with 35-µm-diameter droplets, slightly larger than those used during the laser intensity scan. We note that no dependence of CE on the initial droplet diameter is observed for target size scans performed for a range of droplet diameters from 19–45 µm diameter as long as the target thickness is sufficient to supply tin throughout the laser pulse. As an additional data set for the laser pulse duration we add the high-intensity (1.3×10^{11} W cm^{-2}) scan from the previous Sec. 4.3.2 that had slightly longer idler pulse duration of 4.6 ns due to slightly different settings of the MOPA system.

Again, CE is found to follow the same trend with increasing target diameter as described in Sec. 4.3.1. A slightly higher maximum CE value of 2.9% is observed for the short and intermediate pulse durations, compared with a value of 2.6% obtained for the longest pulse duration. We note that the small observed changes in CE may lie within the systematic uncertainties of the experiment. The rather small changes in CE with pulse duration, as well as laser intensity, imply a near-linear scaling of in-band energy with laser energy. The in-band energy (Fig. 4.2(i)) indeed almost doubles when doubling the laser pulse duration, and up to 3.8 mJ of in-band energy are measured per pulse. The angular distributions of in-band EUV emission are all similar up to an angle of 64° from which point the 7.4-ns case shows increased emission. The anisotropy factor in this 7.4-ns case (see Fig. 4.2(h)) roughly follows the one of the short and medium pulse duration cases up to a target diameter of 180 µm, after which it remains roughly constant at values around 0.6. This observed difference may be attributed to an increased EUV emission volume (which increases with pulse duration), partially extending beyond the liquid disk target, which enables radiating into the forward hemisphere. Another factor contributing to this difference may be a slight tilt of the disk target due to finite drift of the alignment of the laser to the droplet [129].

The recorded spectra, shown in Fig. 4.2(n), are remarkably similar when comparing the different laser pulse lengths. The only minor visible difference is the slightly wider main emission feature in the 7.4 ns case. SP also remains virtually independent of laser pulse duration and follows the same trend as discussed as in Sec. 4.3.1. We note that the small decrease in wavelength from idler to signal may contribute to the observed spectral broadening at the 7.4 ns pulse duration. However, the influence on the spectral emission is expected to be rather limited as the change in wavelength is small. Instead, we expect a larger spatial extent of the plasma at longer pulse durations, which causes larger optical depth and, hence, further spectral broadening. For the longest pulse duration case, we note that the decrease in SP with increasing target size is no longer fully compensated by increases in the anisotropy factor and this is reflected in slightly lower overall CE values.

No major changes were thus observed in the scaling of emission characteristics with target size when changing laser pulse length, besides a levelling off of the anisotropy factor for the longest pulse length. In-band EUV emission is also here seen to follow linearly the input laser energy.

4.4 EUV generation using 1- and 2-μm laser light

In a separate, third set of experiments, plasma is produced using the 1-μm laser beam at an intensity of $1.9(4) \times 10^{11}$ W cm^{-2}. This choice of laser intensity yields identical emission features in the 5–12 nm region compared to the $1.0(2) \times 10^{11}$ W cm^{-2} intensity at 2 μm. Equivalent spectral features ensure a similar charge state distribution of the plasma as each feature is charge-state specific. The factor of 1.9 difference in relative intensity is in agreement with the intensity ratio of 2.1(6) observed for droplet targets [32] and 2.4(7) for planar-solid targets [15].

As shown in Fig. 4.3(a), CE is found to increase monotonically with increasing target size in the 2-μm case until the laser beam reaches full overlap with the target, as described in Sec. 4.3. In line with the findings in Ref. [130] CE is virtually identical for both laser wavelength cases for small target sizes. With increasing target diameter, the 2-μm CE values exceed the ones of the 1-μm case however significantly. The 1-μm CE is found to increase in a near-linear fashion until it plateaus at a value of close to 1.8% above ~150 μm target diameter. In the case of planar-solid targets (effectively infinitely extended disk targets), very similar CE values of 1.7% were inferred from measurements performed at a representative angle of 60° for a comparable 4.8 ns pulse duration and a slightly smaller circular 66-μm-diameter (FWHM) spot [15]. In the 2-μm case, CE values measured on planar-solid targets reach up to 3.1%, only slightly higher than the here-observed values of up to 2.8%.

The angular dependence of the in-band EUV emission for the droplet target (see Fig. 4.3(g)) is very similar for both drive lasers and is consistent with previous studies where a 1-μm laser was used to drive the LPP from a droplet target [16, 78, 120]. The similarities in the angular distributions is in line with a previous study by Chen *et al.* [131] where only minor changes in emission anisotropy were found between 1- and 10-μm-driven droplet plasmas. Similarly to Sec. 4.3, the in-band emission decreases

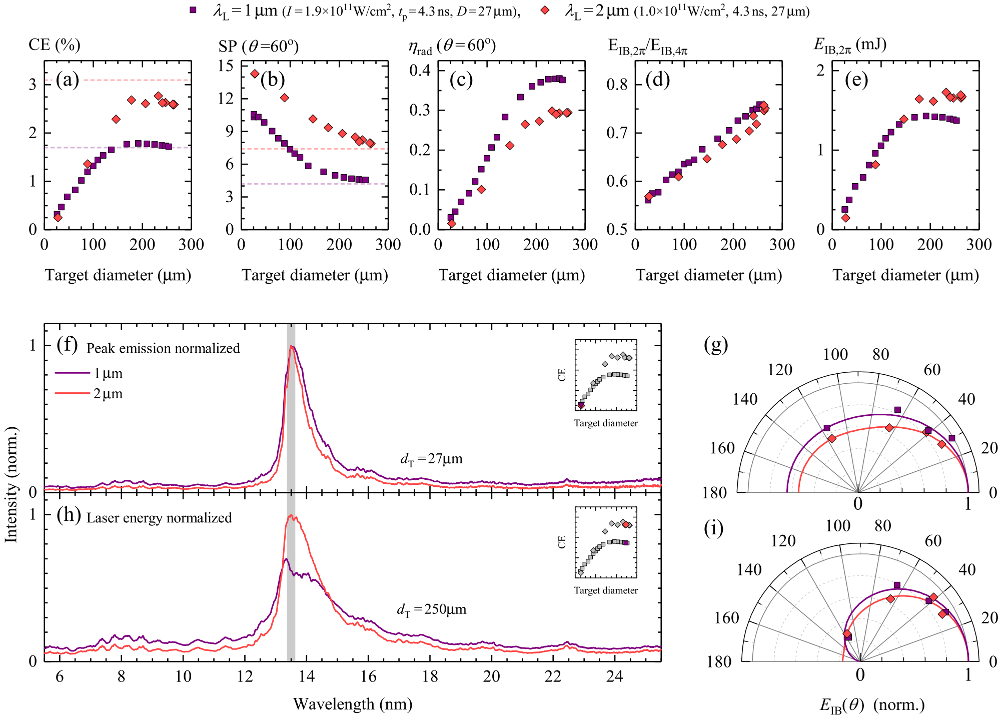

Figure 4.3: Comparison of results for drive laser beams of 1- and 2-μm wavelength at intensities of 1.9 and 1.0×10^{11} W cm^{-2}, respectively. (a) CE, (b) SP, (c) η_{rad}, (d) anisotropy factor $E_{\mathrm{IB},2\pi}/E_{\mathrm{IB},4\pi}$ and (e) $E_{\mathrm{IB},2\pi}$, as function of target diameter. The dashed lines in (a) and (b) indicate the CE and SP values from planar-solid tin targets, respectively [15]. The spectral emission of plasmas for a target diameter of (f) 27 μm (droplet target) and (h) 250 μm (disk target) are shown normalized to their respective peak intensities. The 1-μm spectrum shown in (h) is normalized to laser energy with respect to the 2-μm one. The at 0° normalized angular dependencies of the in-band EUV emission, corresponding to the spectra shown in (f) and (h), are shown in (g) and (i), respectively. Solid lines depict fits of Eq. (4.1) to the data.

more strongly with increasing angle, in particular for the angles $\gtrapprox$90°, for the 250 µm target diameter than for the undeformed droplet target case (see Fig. 4.3(i)).

For the droplet target the anisotropy factor attains a value of 0.57, identical for both laser wavelength cases (see Fig. 4.3(d)). In both laser wavelength cases, the anisotropy factor increases linearly with increasing target diameter as discussed above in Sec. 4.3.2. Uncertainties related to the slightly worse fit of the anisotropy function to the 1-µm disk-target data, which unexpectedly converges to 0 at 180°, may lead to a minor systematic overestimation of the anisotropy factor.

The in-band energy values displayed in Fig. 4.3(e) trivially follow the scaling of CE. In the 1-µm case, values of approximately 1.4 mJ per pulse are achieved while reaching approximately 1.7 mJ in the 2-µm case. The relative difference in the in-band energy values is slightly smaller than for the CE values because of the lower laser energy used in the 2-µm case (viz. 62 vs 80 mJ pulse energy). Despite this smaller laser energy more in-band energy is produced by the 2-µm pulses at target diameters above 160 µm demonstrating here the significant advantage of the 2x longer drive laser wavelength.

For undeformed droplet targets, the spectra for the 2-µm case show a much narrower main emission feature and, relative to the 13.5-nm peak, less out-of-band radiation is emitted in the 2-µm case (see Fig 4.3(f)). These observations are consistent with earlier results [16, 32]. With increasing target diameter the differences in the spectral emission between the two drive laser wavelengths become even more pronounced. In the 2-µm case, the main emission feature simply broadens with target diameter (see Fig. 4.2(h)), in line with expectations from an associated increase in optical depth [51]. In the 1-µm case, the shape of the main emission feature changes drastically due to strong self-absorption, causing the emission maximum to shift to shorter wavelength. These absorption effects become even stronger for increased laser pulse duration, redistributing even more light into other energy channels (see Appendix 4.A). This 'missing' emission in the main feature in the 1-µm case is qualitatively well explained by absorption of in-band radiation from a hotter plasma zone by a colder less emissive plasma zone [15, 93].

SP is found to decrease monotonously with increasing target diameter for both wavelength cases (see Fig. 4.3(b)). In the 1-µm case, the SP for small target diameters is on the order of 10%, and is observed to decrease more rapidly than its 2-µm counterpart down to 4.5% at a 250 µm diameter. This value is consistent with the marginally lower SP value of 4% obtained from measurements on planar-solid tin targets which may be taken as the asymptotic value of SP towards infinite target size [15]. SP in the 2-µm case levels off at a higher value of about 8%, in part explaining the higher CE values observed using this drive laser wavelength.

Radiative efficiency, measured at an angle of 60°, follows a very similar trend in both wavelength cases (see panel (c)) with a larger amplitude in the 1-µm case due to the significantly lower SP values in this laser wavelength case.

No major differences between the anisotropy factors are observed. Comparing the two drive laser wavelength cases, the differences in CE are largely attributable to the decrease in SP. This link between CE and SP further supports the findings of Behnke *et al.* [15], where experiments on solid tin targets demonstrated that plasmas driven by 1-μm laser light exhibit strong EUV self-absorption which is absent in the 2-μm spectra. This makes 2-μm-driven plasmas the more efficient emitter of in-band EUV radiation. We note that conversion efficiencies of up to 3% can in fact be achieved for the 1-μm drive laser case for a homogeneous heating of undeformed droplet targets with several 10-ns-long, spatially flattop-shaped laser pulses [16]. Thus, on one hand, the current limitations to CE for the 1-μm drive laser case for extended disk targets may be eased using alternate target and illumination designs. On the other hand, even larger CE values for the 2-μm drive laser case may be obtained from optimally shaped targets homogeneously heated by a long, flattop laser pulse.

4.5 Conclusions

We have studied plasmas produced from laser pre-pulse preformed liquid tin disk targets with diameters ranging 30–300 μm using 1- and 2-μm drive laser systems. For the 2-μm driver, the conversion efficiency of laser energy to EUV radiation closely follows the fraction of the laser energy absorbed by the tin target and CE values of up to 3% are obtained for the largest targets. Conversion efficiency (CE), spectral purity (SP), radiative efficiency (η_{rad}), and spectral emission are found to be nearly independent of laser intensity and laser pulse duration in the here-studied parameter range. Consequently, a linear increase of in-band radiation towards the backward hemisphere with laser energy is observed when increasing either parameter and further scaling of in-band output per tin target with laser intensity and pulse duration may be possible at little to no cost regarding CE.

Direct comparison of the emission characteristics of 1- and 2-μm-driven plasmas reveals significantly lower CE values for the 1-μm driver under the current experimental conditions when using extended disk targets. The lower 1-μm CE is explained by the particularly strong self-absorption of the emitted EUV radiation in the 1-μm-driven plasma. Comparing here measured CE values of 3% to ones of current state-of-the-art EUV light sources driven by 10-μm CO_2 gas lasers (CE≈6%), CE values of the 2-μm driven plasma are lower by a factor of two. However, comparing overall source efficiency of converting electrical energy to in-band photons, the 2 μm driven source may already exhibit higher overall efficiencies because of the expected significantly higher wall plug efficiency of 2-μm solid state laser technology compared to 10-μm CO_2 gas laser technology. Further, more improvements in terms of CE may be obtainable by homogeneous heating of suitably shaped tin targets with longer laser pulses leading to full evaporation of the then truly "mass-limited" tin target. Such future studies should include research on the influence of laser pulse duration, intensity and laser wavelength on any possible fast ionic or liquid debris that may harm nearby optics elements in possible future industrial EUV light sources based on 2-µm-laser-driven tin plasmas.

Acknowledgements

This work has been carried out at the Advanced Research Center for Nanolithography (ARCNL), a public-private partnership of the University of Amsterdam (UvA), the Vrije Universiteit Amsterdam (VU), the Dutch Research Council (NWO) and the semiconductor equipment manufacturer ASML. The used transmission grating spectrometer has been developed in the Industrial Focus Group XUV Optics at University of Twente, and supported by the FOM Valorisation Prize 2011 awarded to F. Bijkerk and NanoNextNL Valorization Grant awarded to M. Bayraktar in 2015. This project has received funding from European Research Council (ERC) Starting Grant number 802648. This publication is part of the project New Light for Nanolithography (with project number 15697) of the research programme VIDI which is (partly) financed by the Dutch Research Council (NWO).

4.A Appendix

EUV generation using longer pulses of 1- and 2-µm wavelength — long pulse duration

In addition to the comparison between 1- and 2-µm-driven plasmas for the short-pulse case in Sec. 4.4, more data is obtained using longer 1-µm pulses that mimic the temporal profile of the 7.4 ns case in Sec. 4.3.3. The parameters of CE, SP, η_{rad}, $E_{\mathrm{IB},2\pi}/E_{\mathrm{IB},4\pi}$ and $E_{\mathrm{IB},2\pi}$ show similar trends compared to the short-pulse data in Sec. 4.3.3.

The only significant change in comparison with the short-pulse data is observed in the spectral emission of the two drive-laser wavelength cases for disk-targets in Fig. 4.4(h). Here, the spectral emission of plasmas produced with the 1-µm laser beam show even stronger self-absorption of emission at and around 13.5 nm. This stronger absorption manifests itself in slightly lower SP values. The slight deviation in the trend of η_{rad} above 160 µm target diameter in the 2-µm case was already discussed in the main text.

In summary, good spectral performance of the plasma and high CE values are continued to be observed when increasing laser pulse duration of the 2-µm driver. In contrast, increasing the pulse duration of the 1-µm-wavelength driver, self-absorption effects increase significantly and lead to an even larger unwanted redistributing of in-band radiation into other energy channels than in the short-pulse case.

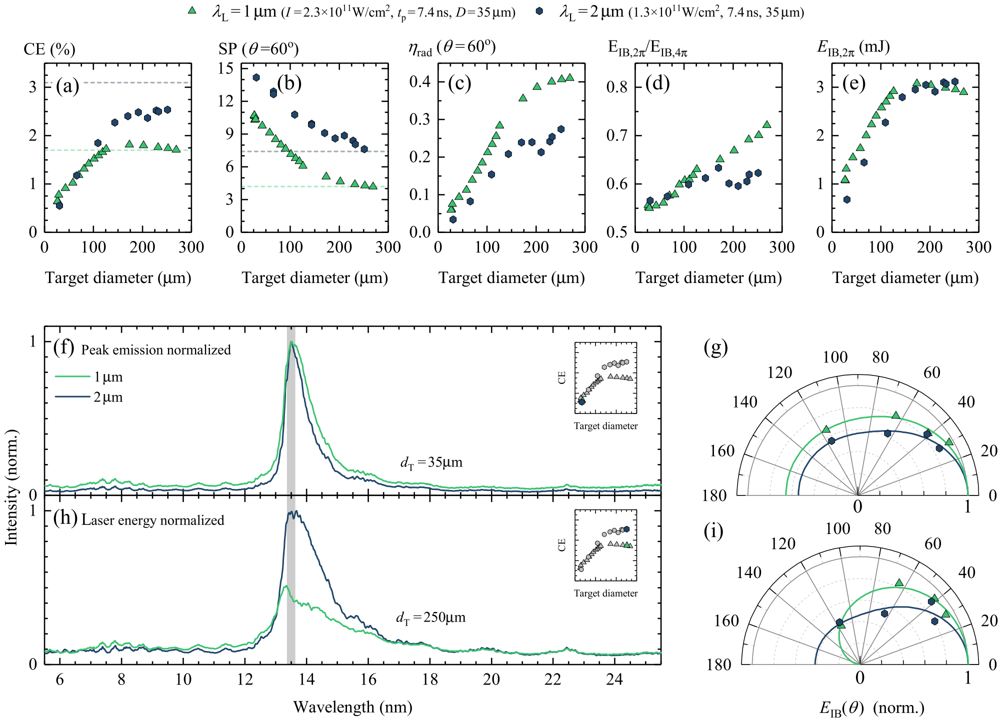

Figure 4.4: Comparison of results for drive laser beams of 1- and 2-µm wavelength at intensities of 2.3 and 1.3×10^{11} W cm^{-2}, respectively, but for a longer pulse duration of 7.4 ns. (a) CE, (b) SP, (c) η_{rad}, (d) anisotropy factor $E_{\text{IB},2\pi}/E_{\text{IB},4\pi}$ and (e) $E_{\text{IB},2\pi}$, as function of target diameter. The dashed lines in (a) and (b) indicate the CE and SP values from planar-solid tin targets, respectively [15]. The spectral emission of plasmas for a target diameter of (f) 35 µm (droplet target) and (h) 250 µm (disk target) are shown normalized to their respective peak intensities. The 1-µm spectrum shown in (h) is normalized to laser energy, instead of its peak emission. The at 0° normalized angular dependencies of the in-band EUV emission, corresponding to the spectra shown in (f) and (h), are shown in (g) and (i), respectively. Solid lines depict fits of Eq. (4.1) to the data.

CHAPTER 5

HIGHLY EFFICIENT GENERATION OF EUV LIGHT USING 2-µm-WAVELENGTH DRIVE LASER LIGHT

(this Chapter will form the basis of a publication)

We experimentally investigate the emission properties in the extreme ultraviolet (EUV) regime of tin plasmas created by irradiating preformed liquid tin targets by 2-µm-wavelength laser pulses. Spatially flat-top (ranging from 70 to 144 µm in diameter) and temporally box-shaped (adjusted from 10 to 31 ns duration) laser pulses are used to homogeneously drive the plasma. Key performance indicators — including the conversion efficiency (CE) of producing in-band energy near 13.5 nm from laser energy, the spectral purity (SP) of the EUV emission, and the angular distribution of the in-band EUV emission — are investigated. We present high CE values of up to 4.7%, outperforming the CEs of plasma driven by lasers with Gaussian beam profiles by about 60%. In addition, the scaling of EUV plasma performance indicators with laser intensity, pulse duration, and laser spot diameter is investigated to explore the in-band energy scaling potential of 2-µm-wavelength driven plasma sources. Whereas increasing laser intensity beyond the optimum value of 0.7×10^{11} W/cm^2 causes a moderate drop in CE, the pulse duration and the spot size have no significant impact on CE and SP within the explored parameter space, allowing achieving in-band energies of nearly 13 mJ at a 31 ns pulse duration with a CE of 4.2%. We demonstrate promising in-band energy scaling capabilities at high conversion efficiencies of 2-µm-driven plasmas, strongly motivating its application in future high-power EUV sources, with the 2-µm-driver significantly outperforming plasmas driven by 1-µm lasers to rival the state-of-the-art 10.6-µm-driven sources.

5.1 Introduction

In previous Chapters 2,3,4, we demonstrate that 2-µm wavelength driven tin plasmas reach conversion efficiencies (CE) of 3% from laser energy to usable "in-band" EUV radiation at 13.5 nm. Those CE values are obtained using Gaussian-shaped spatial beam profiles and are significantly higher than the CEs achieved by 1-µm wavelength-driven plasmas under comparable conditions. Chapter 3 explains in detail how the 2-µm case benefits from a reduced plasma density that leads to a significantly lower optical depth, allowing for a more efficient out-coupling of in-band radiation from the plasma. But studies irradiating tin microdroplet targets with a 1-µm wavelength laser pulse with a spatially uniform flat-top distribution of the laser intensity show CEs (up to 3.2%) [16] that are much larger than the Gaussian-focus experiments, which reached 1.8% (see Chapter 4). It is hypothesized that the more uniform intensity distribution of the beam profile provides optimum heating across the entire surface of the laser beam. It is known from our studies in Chapters 2,3,4, and also, e.g., from the theoretical investigations by Hemminga et al. [7], that the plasma requires a certain laser intensity to efficiently drive the EUV emitting plasma. We expect that irradiating targets with a flat-top 2-µm wavelength laser pulse will lead to a similarly large increase in CE as it did in the 1-µm case. In this Chapter, we provide the first experimental studies with tin plasmas driven by 2-µm wavelength laser pulses with spatially flat-top and temporarily box-shaped profiles. These studies are made possible by our 2-µm laser system providing high-energy laser pulses that can be imaged down to sub-100 µm beam diameters, as presented in Chapter 1.

Besides the sought-after increase in CE, it is crucial for application as an EUV source in industrial nanolithography machines to upscale the total in-band EUV energies from the single mJ level of the previous Chapters to the level of several 10 mJ. The latter EUV pulse energy levels are required to obtain sufficient EUV power (several 100 Watts) at a manageable repetition rate (several 10 kHz) in an industrial setting. The challenge here is to increase the laser pulse energy without incurring significant losses in CE, to achieve high in-band energies. The laser pulse energy can be increased by (i) increasing laser intensity, (ii) increasing the laser spot size, or (iii) increasing laser pulse length. First, the laser intensity can be increased within a certain range while maintaining a plasma temperature favorable for producing Sn^{11+}–Sn^{15+} which contribute to the in-band emission [44, 82, 84]. Second, increasing the laser spot size (along with the target size) would potentially enable the efficient use of more laser energy at optimal intensity, and to obtain more in-band radiation from a plasma that is increased in size. Third, the duration of the laser pulse could be extended, leading to a temporally prolonged plasma with more in-band radiation [7]. The aforementioned studies of 1-µm wavelength-driven tin plasmas show that CE would drop significantly if one would attempt to reach high in-band energies by either increased plasma size or longer pulse durations due to the relatively large optical depth in the case of the 1-μm wavelength-driven tin plasma [51]. 2-μm wavelength-driven tin plasmas are expected to be less limited by optical depth since the plasma is less dense and Chapter 4 already shows promising upscaling of in-band energies by for instance increasing the pulse duration from around 4 to approximately 7 ns. It is yet an open question how far the in-band EUV energies can be scaled up for a 2-μm driver when imaged to provide an optimal, homogeneous heating of the plasma.

In this Chapter, we will demonstrate record-high CEs from 2-μm wavelength-driven tin plasmas based on the application of flat-top beam profiles. The performance of flat-top beam-driven plasma is comprehensively compared with those driven by Gaussian-like beam profiles. Furthermore, we will demonstrate the upscaling potential of in-band energy by systematically investigating the effect of laser intensity, pulse duration, and beam size on key plasma parameters. These efforts ultimately lead to record-high usable in-band energies beyond 10 mJ in a 2π sr solid angle in the backward hemisphere for a preformed sheet-like target.

5.2 Experimental details

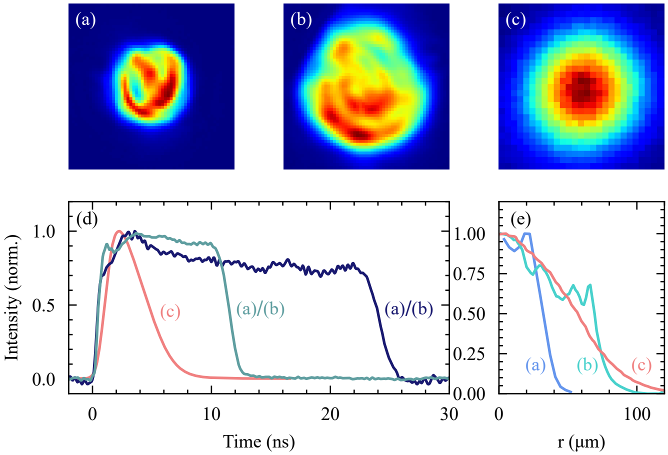

Figure 5.1: Panels (a), (b) and (c) list different 2-µm wavelength spatial profiles of the beam that were used in the experiments; panel width and height equal 200 µm. Panel (a) shows a flat-top main pulse (MP) profile with an average diameter of 70 µm, (b) shows a flat-top beam with a larger diameter of 144 µm, and (c) shows a Gaussian MP beam profile with a diameter of 140 µm (FWHM). Panel (e) depicts the radially averaged line-outs of the beam profiles presented in the upper panel, and (d) represents the different temporal pulse shapes. Both of the flat-top MP beams (a), (b) have boxed-shaped temporal pulses with a pulse duration set to either 10 or 23 ns (FWHM). The red line is the temporal profile of the Gaussian profile (c) with a pulse duration of 7.4 ns.

The experiments are similar to the experiments presented in Chapter 4 with key differences highlighted in this section. Similarly to previous experiments, liquid tin microdroplets are irradiated by two consecutive laser pulses. First, the droplets are irradiated by a pre-pulse (PP) at a relatively low intensity ($\sim 10^{10}\,\mathrm{W/cm^2}$) at 1-µm wavelength. The PP is focused onto the droplet, resulting in a Gaussian spatial profile with a diameter of 71 µm at full width at half maximum (FWHM). Its temporal shape is Gaussian and fixed at a FWHM pulse duration of ∼10 ns. The PP energy is chosen to be either 1 mJ or 8 mJ depending on the particular experiment. The impact of the PP leads to the expansion of the microdroplet to a thin, radially symmetric sheet with a diameter d_T (called the target diameter) that continues to expand up to 500 µm over time until it retracts due to surface tension [122, 124, 132]. Fig. 4.1(c) shows an exemplary selection of front and side shadowgraphy images (see, e.g., Chapters 3 and 4,) of the so-called tin target after PP impact. The PP is followed by a 2-µm wavelength main pulse (MP) that has high intensities ($\sim 10^{11}\,\mathrm{W/cm^2}$) for igniting the EUV emitting tin plasma. By choosing the delay time between pre- and main-pulse we can precisely control d_T.

The MP is generated by a master oscillator power amplifier (MOPA) that is introduced and comprehensively characterized in Chapter 1. This laser system provides a signal wavelength of 2090 nm and pulse energies up to 400 mJ. In contrast to the experiments presented in Chapter 4, the 2-µm (here: signal) beam is not focused (leading to a Gaussian profile) but imaged onto the tin target to achieve a flat-top beam profile of the MP onto the target. For this purpose, the MOPA output is imaged and demagnified by a two-stage relay imaging system to flat-top beam profile with beam diameters ranging from 70 µm to 144 µm at full width at 30% from the maximum as depicted in Fig. 5.1(a) and (b). All main-pulse diameters in this Chapter are given in full width at 30% from the maximum, a value that is found to provide a robust ellipsoidal description of the beam profile (see below). A more detailed description of the imaging system can be found in Chapter 1. Fig. 5.1(c) shows the Gaussian 2-µm wavelength spatial main-pulse profile (referred to as Gaussian MP) with a beam diameter of 140 µm (FWHM) used in the experiments in Chapter 4. We note that the camera used to record profile (c) has larger pixel size than the one used for profiles (a,b). In the following, experimental data from Chapter 4 are used to compare the performance of tin plasmas driven with a flat-top MP versus a Gaussian MP. Fig. 5.1(e) depicts radially averaged line-outs of the three beam profiles in the upper panels (a), (b), and (c), demonstrating the differences in the intensity distribution between the flat-top and the Gaussian profiles. The flat-top beam profiles show a significantly steeper decline in intensity at the edges than at the edges of the Gaussian one. Steep edges of the beam and flattening of the intensity distribution in the center of the beam lead to an increase in enclosed energy E_{encl} compared to the Gaussian beam profile. Here, we define E_{encl} to be the energy enclosed within a contour drawn at a 50% value of the maximum intensity value of the profile. In the following it is expressed as a fraction of the full laser pulse energy entering the vacuum system E_{L}. This fraction may be used as a measure for the amount of laser light that can be efficiently used to heat plasma. The enclosed energy fraction is as high as 70% for a flat-top beam profile, whereas the Gaussian profile only achieves 50%. Not only the spatial profiles, but also the temporal MP profiles differ from the experiments in Chapter 4 in shape and duration. Due to the temporal pulse shaping capabilities of the MOPA, the MP has a box shape with variable pulse duration from 10 to 23 ns (additional data from a 31 ns pulse length case is also presented in this work) as shown in Fig. 5.1(d). This pulse duration exceeds the pulse duration of the non-box-like Gaussian MP of 4.7 ns that is also depicted in Fig. 5.1(d).

The spectral emission of the EUV plasma driven by the MP is captured by the same transmission grating spectrometer as in Chapters 2,3,4 [80]. Again, the spectrometer is mounted at an angle of 60° with respect to the laser axis (see Fig. 4.1). A more detailed description of the spectrometer and its alignment can be found in Chapter 3. We measure the absolute amount of in-band radiation with five photodiode assemblies that are identical to the photodiode assemblies used in Chapters 2,3,4. These assemblies utilize a multilayer mirror near normal incidence to reflect in-band light on the photodiode detectors, and they are calibrated to obtain absolute energy values. A wide angular range of in-band emission is captured with the photodiode assemblies installed at angles of $\theta = 30, 42, 64, 90$, and 115° with respect to the target's surface normal (see Fig. 4.1; an additional photodiode assembly at 90° was installed later and is used in the current work).

The total in-band emission $E_{\mathrm{IB},2\pi}$ covering the entire 2π-hemisphere around the incoming laser beam is obtained by following the same procedure detailed in Chapter 4. Using the value for in-band emission, the conversion efficiency CE is defined as $E_{\mathrm{IB},2\pi}/E_{\mathrm{L}}$, with the laser pulse energy E_{L}. The uncertainty in the CE measurements is in part set by the uncertainty in calibrating the EUV photodiode assemblies. Each photodiode assembly is calibrated individually by comparing it to a synchrotron-calibrated EUV photodiode assembly. The accuracy of the calibration is limited by the signal-to-noise ratio, which depends on the sensitivity of each individual photodiode assembly. We perform a weighted angular fit according to Eq.4.1 where we assign weights per photodiode assembly based on their respective sensitivities. All photodiode assemblies are roughly similarly weighted, except for the photodiode assembly at 42° angle to which a 20 times lower weight is assigned due to its low sensitivity caused by a small aperture leading to a small signal-to-noise ratio. The lower accuracy explains the deviation of the in-band energies measured at 42° angle compared to the remaining photodiode assemblies (cf. 5.2(g)). To estimate the overall uncertainty of the measured in-band energy and thus CE, we vary the fit parameters by their respective error, using all possible permutations, to gauge the effect on the in-band energy obtained after integration of the fitted anisotropy function. Quadratically adding the fit uncertainty contribution to the overall uncertainty of 6% that comes from the systematic uncertainty of the individual calibrations, we conservatively estimate 11% to be the total relative uncertainty on our in-band energy measurements. The uncertainty of the CE is obtained by quadratically adding another 2% uncertainty from the laser energy measurement resulting in a total uncertainty of 11%. Statistical errors are negligible, with every CE measurement being averaged over at least 100 samples, with good signal-to-noise. The total in-band emission $E_{\mathrm{IB},4\pi}$ over the entire 4π-sphere is estimated according to Chapter 4, and is used to gauge the fraction $E_{\mathrm{IB},2\pi}/E_{\mathrm{IB},4\pi}$ of in-band light that is emitted toward the backward hemisphere. This fraction is called the anisotropy factor in the following. Another important measure for source performance is the spectral purity (SP), defined as the ratio of the in-band to the total EUV energy. All SP values are calculated with respect to the spectral range of 5.5–25.5 nm measured at an angle of 60° by the spectrometer. We further define radiative efficiency η_{rad} as the ratio of CE and SP gauging the efficiency of generating EUV light in the spectral range of

5.5–25.5 nm per incoming laser energy E_{L} (cf. Chapter 4). Unlike the work in Chapter 4, we divide CE $= E_{\mathrm{IB},2\pi}/E_{\mathrm{L}}$, accounting for anisotropy, by SP to estimate η_{rad}, instead of using the "local" CE value from the measurement at 60 degrees. We thus account for anisotropy to obtain a better approximation for the fraction of laser energy contributing to the highly anisotropic EUV energy emission.

5.3 Results

In the following, the scaling of the plasma parameters CE, SP, η_{rad}, $E_{\mathrm{IB},2\pi}/E_{\mathrm{IB},4\pi}$ and $E_{\mathrm{IB},2\pi}$ with laser intensity, target diameter, pulse duration, and laser spot diameters are examined. Additionally, we compare the performance of plasmas irradiated by a flat-top beam profile to that of plasmas driven by a Gaussian MP, and the influence of the enclosed energy is discussed.

5.3.1 Intensity and Pulse length scaling

Fig. 5.2(a)–(e) shows a compilation of relevant plasma parameters plotted as functions of the MP laser intensity I. The laser intensity is defined as $I = E_{\mathrm{L}}/ab\pi t_{\mathrm{p}}$, where a and b are the major and minor axes (of the 30% intensity contour) of the slightly elliptical beam profile and t_{p} is the FWHM pulse duration. By changing the laser pulse energy E_{L} of the MP, the laser intensity I is controlled. All results in Fig. 5.2 are obtained from plasmas irradiated by a flat-top MP with a spot diameter of 70 µm as presented in Fig. 5.1(a). We compare plasmas driven by the two different pulse durations 10 ns (upward triangles in Fig. 5.2) and 23 ns, where both temporal pulses possess box-like temporal shapes, as shown in Fig. 5.1(d). All data in Fig. 5.2 are obtained from expanded tin sheet targets with a target diameter of 116 µm, produced using a 1 mJ PP, and the initial droplet diameter is 52 µm. These target conditions are chosen to avoid "burn-through" (i.e. the target rarefying to a point where the laser light is no longer absorbed but is transmitted leading to CE loss) at higher laser intensities while ensuring full geometrical overlap between plasma and MP. All data points presented in Fig. 5.2(a), (c,d,e), and (g) represent the mean over 100 individual laser shots. Spectral data used in panels (b,f) were averaged typically over 50 shots given the longer exposure and readout times of the spectrometer camera. The angular dependence of the measured in-band emission is first fitted by Eq. (4.2) (see Fig. 5.2(g)), and in-band energies are extracted by integration as described in Chapter 4.

CE shown in Fig. 5.2(a) experiences a sharp rise when increasing I from 0 to 0.7×10^{11} W/cm^2, where it reaches a maximum CE of 4.7%. At higher intensities, CE drops moderately to 4% at intensities around 1.5×10^{11} W/cm^2. Both 10 and 23 ns pulse durations have virtually identical CE values at same laser intensities. We find a

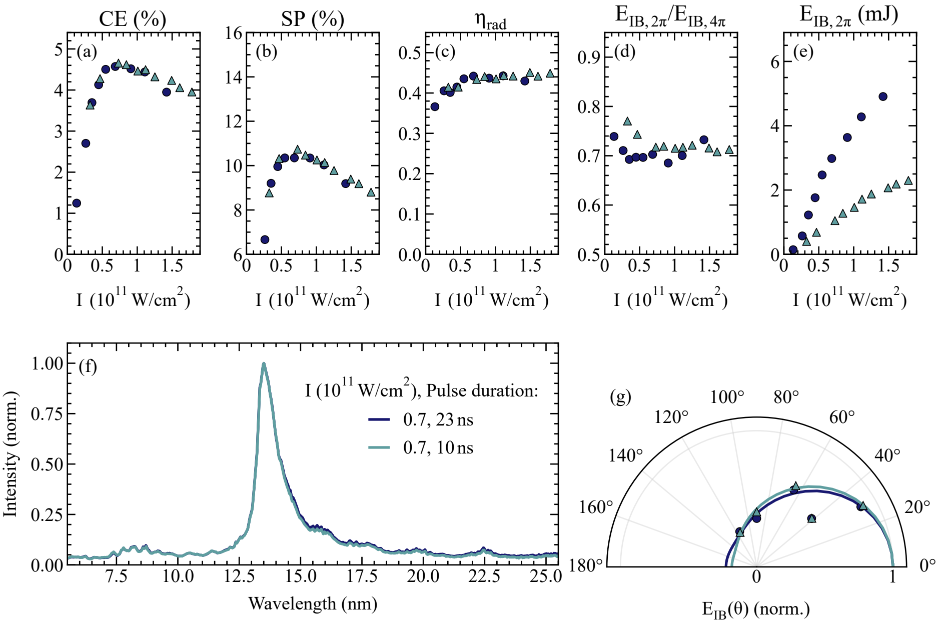

Figure 5.2: Results obtained from tin plasmas driven by a spatial flat-top beam profile of 70 µm diameter as presented in Fig. 5.1(a) with a pulse duration of 23 ns (●) and 10 ns (▲) as shown in Fig. 5.1(d). The diameter of the preformed target is 116 µm with an initial droplet diameter of 52 µm. Panels depict (a) CE, (b) SP, (c) η_{rad}, (d) anisotropy factor $E_{\mathrm{IB},2\pi}/E_{\mathrm{IB},4\pi}$, and (e) $E_{\mathrm{IB},2\pi}$ as function of laser intensity I. Panel (f) shows the peak-normalized spectra for the two pulse durations, both at a laser intensity of $0.7 \times 10^{11}\ \mathrm{W/cm^2}$, where the CE reaches a maximum of 4.7%. The corresponding angular dependence of the in-band emission, with the fit function results (and underlying data) normalized to the value at $\theta = 0°$, is shown in (g).

similar behavior for the SP in Fig. 5.2(b), which shows a sharp rise at low intensities up to $I = 0.7 \times 10^{11}$ W/cm^2 where SP reaches a maximum of around 10.5% for both pulse durations. The SP declines for higher intensities, following a trend that is very similar to that of the CE. This correlation between CE and SP is explained by the fact that both values depend on the emission around 13.5 nm which is influenced by the charge-state distribution of the tin plasma, where mainly Sn^{11+}–Sn^{15+} contribute to in-band emission [44, 82, 84]. Since the population of corresponding charge states depends on the laser intensity, CE and SP are affected similarly by the variation in intensity. A more detailed discussion of how the laser intensities affect the spectral emission properties of tin plasmas can be found in Chapter 4. Both CE and SP trends indicate an optimum charge-state balance for the highest in-band emission at a laser intensity around 0.7×10^{11} W/cm^2. This finding is similar to those in previous Chapters suggesting optimal plasma heating at around 1×10^{11} W/cm^2 peak laser intensity. Note that the laser intensity in previous Chapters is defined as the peak intensity of a laser beam with Gaussian spatial profile and a Gaussian-shaped temporal pulse in contrast to the here studied flat-top beam profile with a box-shaped temporal pulse. Those discrepancies naturally lead to minor differences in the estimated intensity associated with optimum heating. The actual emission spectra for both compared pulse durations are shown in Fig. 5.2(f) at optimum laser intensity of 0.7×10^{11} W/cm^2. Both pulse durations give identical spectra in the spectral region of 5.5–25.5 nm, which indicates that the charge-state balance is not affected by the change in pulse duration.

Fig. 5.2(c) shows the radiative efficiency η_{rad} as a function of the laser intensity, where it shows a slight increase from 0.37 to plateauing at around 0.42 above a laser intensity of 0.7×10^{11} W/cm^2. Since η_{rad} is defined as the ratio of CE to SP, its apparent very minor dependence on laser intensity again demonstrates the correlation between CE and SP. The radiative efficiencies exceeding 0.4 are significantly higher than those found in the Chapter 4 that are well below 0.3 and based on Gaussian MPs, because of the long Gaussian intensity wings leading to underheated plasma which has a low contribution to the emission in the 5.5–25.5 nm spectral regime (we reflect on this point below). A constant η_{rad} with intensity is also found in Chapter 4 and in simulation based studies [7].

Fig. 5.2(c) shows a relatively constant progression of the anisotropy factor $E_{\text{IB},2\pi}/E_{\text{IB},4\pi}$, averaging around a value of 0.7, with laser intensity, apart from a slight drop below the intensities of 0.5×10^{11} W/cm^2. There is no significant difference between the two pulse durations. The indifference of anisotropy between the two pulse durations is also visible in the Fig. 5.2(g) presenting the angular-resolved in-band emission, including the fit function based on Eq. (4.2), at an intensity of 0.7×10^{11} W/cm^2. It illustrates that 70% of the in-band radiation is radiated at angles θ pointing to the backward hemisphere. Values for the anisotropy factor of around 0.7 and higher are an indication that the target dimensions are sufficient to fully capture and block the incoming MP so that most of the EUV light is directed back towards to the incoming laser pulse. This observation-based relation is discussed in Sec.5.3.2 in more detail.

Fig. 5.2(c) shows the monotonous increase of the in-band energy $E_{\mathrm{IB},2\pi}$ with laser intensity. In the 23 ns case $E_{\mathrm{IB},2\pi}$ reaches 5 mJ at an intensity of 1.4×10^{11} W/cm^2 corresponding to a MP energy of around 125 mJ. The maximum in-band energy of the shorter 10 ns MP is accordingly lower with a value of around 2.3 mJ at a MP energy of approximately 60 mJ. The difference between the 10 and 23 ns cases reflects the MP energy scaling with pulse duration of ca. 2× while keeping the intensity fixed, since the CE remains unchanged. Evidently, $E_{\mathrm{IB},2\pi}$ can be proportionally scaled by prolonging the pulse duration from 10 to 23 ns since the CE remains unaffected. In addition, the in-band energy output can be scaled by scaling the laser intensity (constant spot size and pulse duration) beyond the optimal intensity of 0.7×10^{11} W/cm^2, where CE reaches a maximum of 4.7%. Since CE drops only by 0.7 percentage points thereafter, the in-band energy can be increased by 60% from 3 to 5 mJ for the highest MP energy used. Pulse-duration scaling and laser intensity scaling both appear to be viable methods to scale the total in-band energy output of EUV sources within the shown parameter frame.

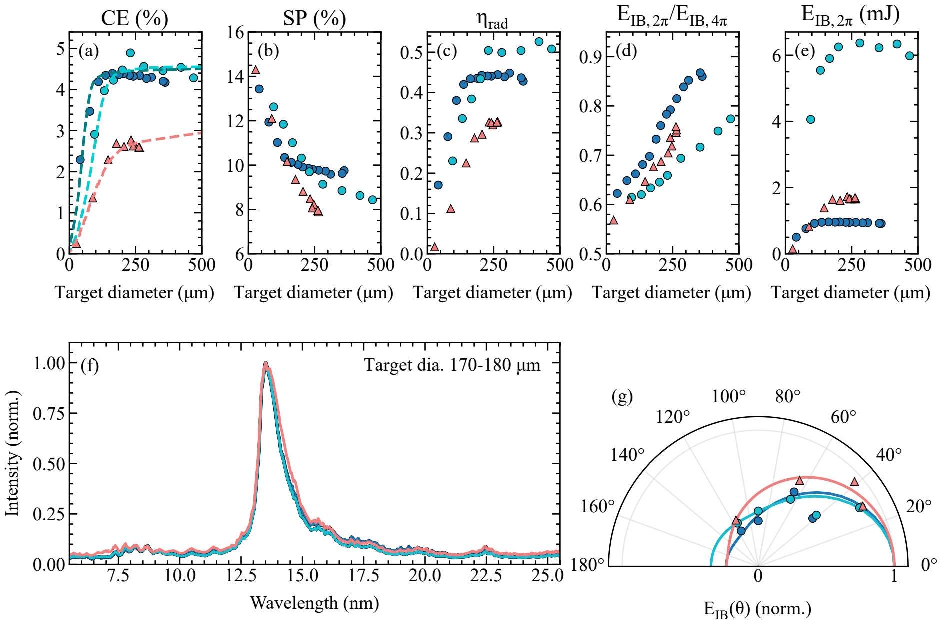

Figure 5.3: Key plasma parameters as a function of varying target sizes for different MP beam profiles: (●): flat-top beam with spot diameter 70 μm with a pulse duration t_p = 10 ns, (●): flat-top beam 144 μm with t_p = 23 ns, (▲): Gaussian beam with spot diameter 140 μm with t_p = 4.7 ns (all beam profiles depicted in Fig. 5.1(a–c) and temporal profile are shown in Fig. 5.1(d)). (a) CE for the different spot sizes, dashed lines show energy fraction on target fore respective beam profiles. (b) spectral purity SP, (c) radiative efficiency η_{rad}, (d) anisotropy factor $E_{IB,2\pi}/E_{IB,4\pi}$, (e) in-band energy $E_{IB,2\pi}$, (f) emission spectra of the three beam profiles at a target diameter of about 170–180 μm, and (g) the corresponding angular dependence of the in-band emission, with the fit function results (and underlying data) normalized to the value at $\theta = 0°$.

5.3.2 Target size scaling

In the following, we investigate the influence of the target diameter and examine the differences between MPs with a flat-top beam profile and those with a Gaussian beam profile. In the case of flat-top MPs, pulse durations of 10 and 23 ns with box-like temporal shape as shown in Fig. 5.1(d) are used, with beam spot diameters of 70 μm (●) and 144 μm (●). The flat-top beam profiles are comparable to those shown in Fig. 5.1(a). Various target sizes are produced by PP impact on 41 μm diameter tin droplets with a PP energy of 8 mJ and a Gaussian temporal pulse of 10 ns duration (FWHM). The targets are irradiated by an MP laser intensity of 0.7×10^{11} W/cm^2 in the 10 ns, 70 μm case (●) and 0.4×10^{11} W/cm^2 in the 23 ns, 144 μm case (●). The intensities (0.4–0.7×10^{11} W/cm^2) were set to produce similar spectral out-of-band features (Fig. 5.1(f)); uncertainties in the estimation of the spot size may contribute to the apparent large difference in the reported intensity values. For Gaussian MP, all data are based on the experiments in Chapter 4. More specifically, the data are from Fig. 4.2 with 4.7 ns FWHM MP duration. The temporal shape of the MP is not box-like but resembles a skewed Gauss as shown in Fig. 5.1(d). The initial droplet diameter is 35 µm being shaped to the various target diameters using a PP of 8.4 mJ. We note that the pulse duration and the spot diameter of the PP are, with 25.9 ns and 116 µm (both FWHM), respectively, different from those used for the flat-top MP case. However, we expect that these changes play but a minor role in the target morphology cf. [133].

All results are shown in Fig. 5.3, in an analogous fashion to Fig. 5.2 of Sec.5.3.1, but with the target diameter as the variable parameter. Fig. 5.3(a) displays the CEs as a function of the target diameter for the 10 ns flat-top (●), 23 ns flat-top (●), and Gaussian MP (▲). Starting from the base droplet diameter, the CE of the flat-top MP has a value of around 2.5% and reaches a maximum of ca. 4.5% at a target diameter of 120 µm in the case of the 70 µm beam size, and 200 µm in the case of the 144 µm beam size. CE values for the two cases remain remarkably constant even after another 3× increase in target diameter. The rise in CE partially originates from the increase in the geometric overlap between the beam and the expanding target, leading to more laser energy-on-target (EoT) available for driving the EUV-emitting plasma. An increasing EoT fraction (as defined w.r.t. E_L) is also observed and discussed in Chapter 4, where a Gaussian MP is used. The Gaussian MP shows an CE that begins at 0.5% and increases to a maximum of around 2.8% with the growing target diameter, where it begins to plateau beyond a diameter of 180 µm. In contrast to Chapter 4, instead of modeling the (there Gaussian) beam profile, we here estimate the relative EoT by integrating the respective measured MP beam profiles (shown in Fig. 5.1(a–c)) over a circle centered with respect to the beam profile representing the target, and divide the result by the integral over the entire beam. The assumption of a circular target is a good approximation of the real disc-shaped tin target, as shown in Fig. 4.1(c). Integration is carried out in the overlap region for effective target diameters ranging from 0 to 500 µm, and we obtain the relative EoT fraction on a circular target as a function of the effective target diameter. Note that the target diameters used in the plots in Fig. 5.3(a)–(e) are the diameters of the liquid tin targets before the MP arrives at the target. In less than 5 ns after impact of the MP on the target, the plasma however attains a steady state with a steady critical plasma surface that absorbs the incoming MP laser light well away from the liquid surface [7]. This critical surface remains at a near constant distance from the liquid surface of the target, effectively extending the dimensions of the target also in the lateral direction and, thus, increasing the effective target diameter — by approximately 20 µm in the case of 2-µm-driven tin plasmas driven by similar intensities [7]. This estimate of the lateral extension of the critical surface is based on a simulation of a droplet target half the diameter of the incoming MP beam. We correct for plasma expansion by subtracting 20 µm from the effective target diameter from our estimate of the relative EoT to obtain the relative EoT as a function of the target diameter of the liquid tin target, as used in the curves shown in Fig. 5.3. Although the correction is based on simulations for a droplet target, it is a valid first-order approximation because the correction only has an effect for sheet targets smaller than or close to the MP beam diameter, where the plasma can wrap around the target and extend at the edges of the target, similar to the droplet target scenario in [7].

The calculated relative EoT is normalized to the respective maximum CE and is plotted in Fig. 5.3(a) (dashed lines), where it shows good agreement with the measured CEs. It appears that EoT attributes the increase in CE with increasing target diameter mostly to an increased geometrical overlap, with ever more laser energy contributing to the in-band emission. Moreover, it becomes evident that the specific beam profile of the MP has a significant impact on the EoT. The steeper incline of CE in the case of flat-top MP (●) is due to the smaller spot size of the MP of around 70 µm reaching full geometric overlap at smaller target diameters than the 144 µm spot size of the larger flat-top MP (●) and the larger Gaussian MP (▲). Compared to flat-top MPs, the transition from an incline to a plateauing CEs seems more continuous in the Gaussian case, and the EoT keeps increasing at larger target diameters. This difference is due to steeper beam profile edges of a flat-top beam compared to the Gaussian beam, where the intensity extends further outward (cf. Fig. 5.1(e)). Thus, a flat-top beam profile with steep edges reaches maximum EoT at smaller target diameters at a given spot size. The maximum CE in the Gaussian case is significantly lower than in the flat-top case, which is mainly attributed to the reduced enclosed energy of the Gaussian beam profile of ca. 50% compared to enclosed energies of about 70% in flat-top cases. We discuss the effect of enclosed energy on CE in Sec.5.3.3.

Fig. 5.3(e) shows the total in-band energy emitted to the back hemisphere and shows a very similar trend to CE in panel (a), since $E_{\mathrm{IB},2\pi}$ equals CE times the laser pulse energy E_{L} . The in-band energy for the 4.7 ns Gaussian reaches a maximum of 1.8 mJ, while the 10 ns flat-top reaches 1 mJ, and the 23 ns flat-top goes up to 6.3 mJ. The in-band energy of the 23 ns flat-top MP (●) is relatively high because it has with $E_{\mathrm{L}} \approx 170$ the highest laser pulse energy of the three cases due to its large spot size of 144 µm. Out-of-band emission in the spectral region below 12 nm shown in Fig. 5.3(f) indicates a plasma of comparable plasma temperatures (cf. Ref. [83, 107]) in the cases of the two flat-top beams and a very modestly overheated plasma in the case of the Gaussian beam (cf. Chapter 4). But as concluded in the previous Section 5.3.1, any such overheating in this regime has only a minor impact on the reported plasma output characteristics.

Next, the anisotropy factor that quantifies the angular distribution of in-band light emitted is shown in Fig. 5.3(d). In the case of a 10 ns flat-top beam (●), the anisotropy factor starts at approximately 0.63 for the undeformed droplet and increases steadily to 0.87 at larger target diameters. The 23 ns flat-top beam (●) shows significantly lower anisotropy factors at a similar upward trend. The Gaussian case (▲) shows a similar monotonous incline with target diameter, at anisotropy factors of 0.57 up to 0.79. All cases show a increasing fraction of in-band radiation being emitted toward the backward hemisphere, where it is usable for EUV lithography applications. The decrease in radiation to the $\theta = 180°$ direction for enlarging target diameters may be caused by one-sided heating of the expanded target by the MP, as the plasma may be shielded by a still liquid tin phase, as pointed out in Chapter 4. A generally lower anisotropy factor in the case of 23 ns flat-top beam (●) may be explained by the larger spot diameter of 144 µm and the longer pulse duration of 23 ns compared to the other cases, leading to a further extending EUV emitting plasma wrapping around the target, even at larger target diameters. We note that the anisotropy factor is ≥ 0.67 for full geometric overlap in all cases, and all the anisotropy factors in Fig. 5.2(d) are larger than 0.67 indicating full geometric overlap for maximum in-band emission throughout the intensity scans.

Fig. 5.3(b) depicts the decrease of the SP values with increasing target diameter, where all data decrease from a common ∼14% value for the case of an undeformed droplet, to lower SPs at increased target diameters. The decline of flat-top SP-data exhibits a flattening that starts at those target diameters at which full geometric overlap is established. The SP of the Gaussian MP in contrast continues its gradual decrease to a value of 7.5% at the largest 300 µm target diameter for which data is available.

Radiative efficiencies shown in Fig. 5.4(c) plateau in both flat-top cases when full geometric overlap is established. For the 10 ns case this plateau lies at $\eta_{\mathrm{rad}} = 0.44$, with the 23 ns case η_{rad} plateauing at a relatively similar (given the differences in intensity, beam profiles, etc) value of 0.5. For the Gaussian MP, η_{rad} shows no clear plateauing behavior and increases steadily to 0.33.

A general decline in SP with target diameter that contrasts with the incline in CE is also reported in previous Chapter 4 and in 1-µm-wavelength-driven plasma studies [16, 51]. This general incline can be attributed to an increase in the plasma's optical depth, which scales with growing target diameter before reaching full geometric overlap[51]. An increase in optical depth leads to spectral broadening around the spectral emission feature at 13.5 nm resulting in lower values for SP. The increase in optical depth does not seem to be directly caused by the increasing lateral plasma expansion, because increasing the MP spot size on large enough targets does not affect the SP as demonstrated in Fig. 5.4(b). Apparently, the change in optical depth is related to the evolution of a more three-dimensional plasma expansion in the case of target sizes smaller than the spot size to a more one-dimensional plasma expansion towards the incoming laser beam for targets larger than the laser spot size. Recall that the SP is probed at a fixed angle of $\theta = 60°$ meaning that we can only speculate about the angular variation of optical depth. The SP flattening in the decline of the flat-top cases occurs because, after establishing full geometric overlap, the plasma is not expected to change significantly with further increasing target diameter since the liquid tin phase exceeds the plasma in lateral dimension. This means that larger target diameters simply create excess liquid tin that would not fuel the plasma and, therefore, would not increase its size. The fact that the SP still drops, even though less steeply, might be due to secondary, underheated plasmas (cf. Chapter 2). The SP from the Gaussian MP keeps dropping at a more constant rate since the laser energy extends more outward with respect to the center of beam, as indicated by the line-out in Fig. 5.1(e). Therefore, even at a target diameter greater than 200 µm EoT increases, as shown in Fig. 5.3(a), but this additional energy is at low intensities, adding an underheated plasma that leads to absorption of in-band EUV light originating from hotter plasma, as discussed and quantified in Chapter 2. The long Gaussian wings make that the reduction in SP due to self-absorption effects is much more noticeable as compared to the flat-top illumination case above.

5.3.3 Scaling with spatial beam properties

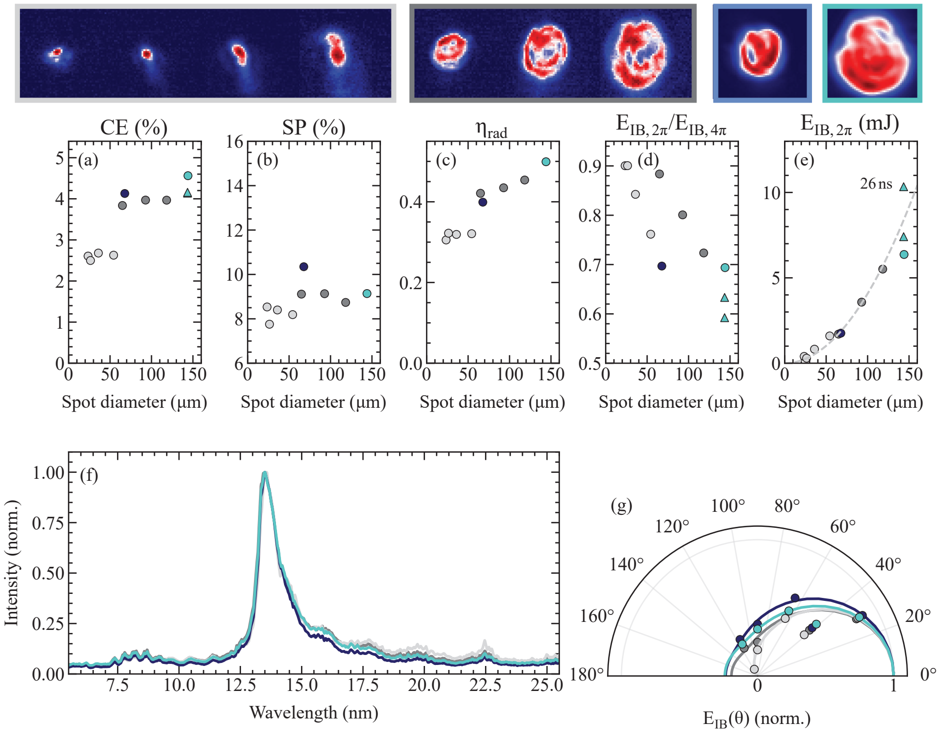

Figure 5.4: Key plasma output parameters obtained irradiating tin sheet targets with various MP beam profiles as depicted in the upper panel. The left-most box with light gray frame shows beam profiles closest to the focus; the center box with dark gray frame depicts beam profiles closer to and/or after the image plane that appear more flat-top-like; and the two right-most boxes represent the image planes with 70 and 144 μm diameter. Frame colors match corresponding symbol color in the panels below. The laser intensities are set to 0.5–0.6×10^{11} W/cm^2, except for the smallest beam spots that have intensities ranging from 1–1.6×10^{11} W/cm^2 (●) and the 144 μm flat-top MP (●) with 0.4×10^{11} W/cm^2. Data with 144 μm spot diameter and intensities in the range of 0.5–0.6×10^{11} W/cm^2 are marked with (▲) to distinguish them from the lower intensity case (●). Note that the laser intensity variations in this range have only a minor impact on the plasma parameters discussed except for the in-band energy. The pulse duration ranges from 22–23 ns, except for one 144 μm flat-top MP (▲) with a pulse duration of 26 ns as shown in panel (e). Panels depict (a) CE for the different spot sizes, (b) spectral purity SP, (c) radiative efficiency η_{rad}, (d) anisotropy factor $E_{IB,2\pi}/E_{IB,4\pi}$, (e) in-band energy $E_{IB,2\pi}$, dashed line shows quadratic scaling of the in-band energies with spot size (details in text), (f) emission spectra of the four spot categories, and (g) the corresponding angular dependence of the in-band emission, with the fit function results (and underlying data) normalized to the value at $\theta = 0°$. Note that the target diameter for the 70 μm flat-top (●) is 116 μm and deviates from the target diameters of 270–280 μm associated with other data points.

In this section, we compare key emission properties from plasma driven by a variety of MP spot sizes and shapes. Fig. 5.4 shows these properties as obtained from a series of scans in which the position of the final imaging lens (see Fig. 1.1) is adjusted so that the imaging plane is shifted with respect to the target along the beam propagation direction. This method enables us to create plasma with beam diameters ranging from 24 to 118 µm by changing the distance between the target and the lens, placing the target in different places along the beam caustic after the imaging lens; this procedure is referred to as the caustic scan in the following. In addition to the diameter of the target beam on the target, the intensity profile of the beam also changes, as shown in the upper panel of Fig. 5.4 (boxes in gray frames). The beam profiles on the left side (light gray box in Fig. 5.4) are from positions in front of the imaging plane closer to the beam focus, with smaller beam diameters from 20 to 55 µm and a more Gaussian appearance. In contrast, beam profiles taken closer and/or after the image plane are more flat-top-like in appearance and have larger spot diameters of 64 to 118 µm (dark gray box in Fig. 5.4). In addition to this selection of different beam profiles based on the caustic scan, results are shown from plasmas irradiated in the image planes as introduced in Fig. 5.1(a) and (b) with spot diameters of 70 and 144 µm. The pulse duration is 22–23 ns, except for one 144 µm flat-top MP (▲) with a pulse duration of 26 ns (as indicated in Fig. 5.4(e)). The laser intensities are set to 0.5–0.6 $\mathrm{W/cm^2}$, except for the smallest beam spots that have intensities ranging from 1–1.6 $\mathrm{W/cm^2}$ (○) and the 144 µm flat-top MP (●) with 0.4 $\mathrm{W/cm^2}$. The data with 144 µm spot diameter and intensities in the range of 0.5–0.6 $\mathrm{W/cm^2}$ are marked with (▲) to distinguish them from the lower intensity case (●). The target diameter is 270–280 µm with the exception of the 70 µm flat-top beam depicted by (●) in Fig. 5.4. We avoid corrupting data by burn-through and/or insufficient geometric overlap by choosing optimum target dimensions and carefully monitoring the EUV emissions. All MP energies are set to produce similar spectral features in the 5–12 nm spectral range to obtain plasmas with comparable charge-state balances; the respective spectra are shown in Fig. 5.4(f).

Fig. 5.4(a) shows CEs for different spot diameters, with CEs ranging from 2.5–2.7% for the smaller spots that deviate the most from a flat-top profile, and CEs of 3.8%–4.6% for spots resembling flat-top profiles. When comparing CE values within one of the two beam profile categories, CE appears to be not affected by spot diameter. Looking at the anisotropy factor in Fig. 5.4(d), the light gray dots show a decline from 0.9 to 0.76 and the dark gray dots show a decline from 0.89 to 0.72, which is not reflected in the trend of the corresponding CE, indicating that *additional* in-band radiation is produced toward the front hemisphere. The general decline of the anisotropy factor with increasing spot diameter is expected, since the plasma's lateral diameter is expected to grow with spot diameter (assuming the target diameter is larger than the spot diameter). Hence, the shielding effect of the target's liquid tin phase on the in-band emission toward the

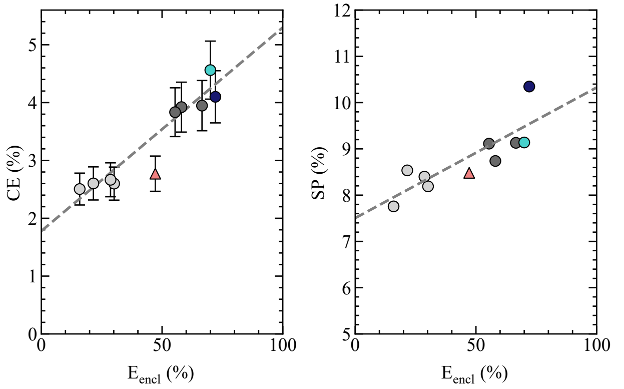

Figure 5.5: Panels depict (a) CE and (b) SP as a function of enclosed energy E_{encl}; the dot color indicates the corresponding beam profile shown in the upper panel in Fig. 5.4; the red dot shows data from the Gaussian beam profile depicted in Fig. 5.1(c). The error bars of the CE data are based on a systematic uncertainty of 11%. (a) The dashed line represents a linear fit $a_{\mathrm{CE}} + b_{\mathrm{CE}} \cdot E_{\mathrm{encl}}$ (excluding the Gaussian profile (▲)) with $a_{\mathrm{CE}} = 1.8$, $a_{\mathrm{CE}} = 0.035$. (b) The dashed line represents a linear fit $a_{\mathrm{SP}} + b_{\mathrm{SP}} \cdot E_{\mathrm{encl}}$ with $a_{\mathrm{SP}} = 7.5$, $a_{\mathrm{SP}} = 0.028$.

front hemisphere decreases with increasing lateral plasma extension, analogous to the description in the previous section Sec.5.3.2. The 70 µm flat-top (dark blue dot) has a relatively low anisotropy factor of 0.7 due to the target diameter of 116 µm which is significantly smaller than the 270–280 µm target diameters in the other cases (due to experimental limitations no larger target sizes are available for the 70 µm flat-top). This observation is in line with the behavior of the anisotropy factors for varying target diameters shown in Fig. 5.3(d). The significantly larger flat-top profile with a spot size of 144 µm (●) also shows an anisotropy factor of 0.7. Interestingly, the ratio of target diameter to spot diameter is roughly two and thus similar to the same ratio in the 70 µm flat-top case, which is 1.7. A similar target-to-spot diameter ratio could explain similar anisotropy factors because the target's liquid tin phase would have a similar shielding effect on the in-band emission in both cases.

The in-band energies in Fig. 5.4(e) show a quadratic increase from 0.3 to 10.3 mJ with increasing spot diameter. This can be explained from that fact that CEs remain relatively constant (with the exception of the non-flat-top profiles), and that the MP energy is scaled to approximately maintain constant laser intensities. To confirm quadratic scaling, we estimate the in-band energy according to $E_{\mathrm{IB},2\pi} = \overline{\mathrm{CE}} \cdot \overline{I_{\mathrm{L}}} t_{\mathrm{p}} \pi d_{\mathrm{s}}^2/4$, with the average conversion efficiency $\overline{\mathrm{CE}} = 4.1\%$, the average laser intensity $\overline{I_{\mathrm{L}}} = 0.55 \times 10^{11}\ \mathrm{W/cm^2}$, pulse duration $t_{\mathrm{p}} = 23$ ns, and the spot diameter d_{s}. The average CE and intensity are based on the data shown in Fig. 5.4(a), where the non-flat-top-like beams are excluded since they deviate significantly in CE and intensity from the flat-top data due to lower enclosed energy fraction in their respective MP beam profiles (cf. Fig5.5(a)). The resulting parabola is shown in Fig. 5.4(e) (dashed line) and confirms the quadratic scaling of the measured in-band energies with the spot size. Evidently, the in-band energy of the 144 µm flat-top beam (●) does not follow quadratic scaling, because the corresponding laser intensity of 0.4×10^{11} W/cm^2 is approximately 30% lower than the average intensity. Due to the observations in Sec.5.3.1 it can be assumed that this lower intensity would also linearly reduce the in-band energy, with the CE being barely affected. The 144 µm flat-top beam (▲) with a pulse duration of 26 ns has a slightly higher in-band energy than the quadratic scaling suggests due to its longer pulse duration (and also its intensity is approximately 20% larger than the other (▲)), demonstrating how the pulse duration scales the in-band energy without impacting the CE.

The SP shown in Fig. 5.4(b) is around 8% for the non-flat-top-like beam shapes below 60 µm spot diameter, and around 9% for the flat-top beam profiles — except for the smallest, 70 µm flat-top beam at 10% SP. The SP of that beam is slightly elevated because the target diameter is with 116 µm exceptionally small, leading to larger SPs as demonstrated in Fig. 5.3(b). Remarkably, the spot diameter and correlated the lateral plasma size do not affect the SP, as measured at a single angle at $\theta = 60°$.

The radiative efficiency η_{rad} shown in Fig. 5.3(b) is approximately 0.32 for the non-flat-top-like beam shapes, while the flat-top beam profiles show an increasing η_{rad} with spot diameter from 0.4 to 0.5. The reduced radiative efficiency for the non-flat-top-like beam shapes points out that there is less EUV light produced in the spectral range 5.5–25.5 nm also leading to less CE. Evidently, looking at the spectra in Fig. 5.3(f), the non-flat-top-like beams create more spectral features associated with low-charge ion states $\leq$ Sn^{6+} that emit at wavelengths longer than 16 nm [96] and beyond the monitored spectral range. These emissions from the lower charge states are possibly from underheated parts of the plasma due to the low-laser-intensity areas surrounding the highly intense center of the non-flat-top-like beam profile, as shown in the upper panel of Fig. 5.3. The flat-top beam profiles show less emission attributed to underheated plasma, leading to higher radiative efficiency and CEs.

Fig. 5.5(a) shows CE as a function of the enclosed energy E_{encl} for the data presented in Fig. 5.4, excluding the 144 µm diameter flat-top data marked with (▲) since there is no precise estimation for the corresponding enclosed energy fraction available. The enclosed energy is defined as the integral within the 50% contour line of the MP beam profile divided by the total integral to estimate the fraction of energy within the beam area with local intensities higher than 50% of the peak intensity. Enclosed energies based on a 50% contour line are about 15 percentage points below values for enclosed energies that are based on the 30% contour line (used for spot diameter estimation) for typical flat-top profiles. The enclosed energies vary from 20% for peak-like beam profiles, as shown in the gray box in Fig. 5.4, over 50% for a Gaussian MP as shown in Fig. 5.1(c), and up to 70% for flat-top profiles used in our experiments. The enclosed energy is closely correlated with CE, as indicated by the increase in CE from 2.5% to 4.6% with increasing E_{encl}, and this correlation readily explains the difference in CE between the sets of spot diameters below and above 60 µm in Fig. 5.4(a). A heuristic linear fit is depicted as a dashed line in Fig. 5.5(a), accurately matching the observed increase in CE. The CE of the Gaussian MP is not in agreement with the linear trend, because its beam profile has a wider radial extent than all other beam profiles (see Fig4.1(e)) leading to a maximum of ca. 90% energy on target (EoT) as indicated in Fig4.2(a), whereas all other beam profiles reach 100% EoT. This loss in laser energy available for plasma formation explains a lower CE in the Gaussian MP case than the linear trend with E_{encl} suggests. Note that an increased target size to achieve 100% EoT would most likely not increase CE since SP keeps declining as shown in Fig4.2(b) due to additional underheated plasma created by the long low-intensity wings of the Gaussian MP. This additional underheated plasma does not only add out-of-band emission from lower charge states, but it would also induce additional spectral broadening around 13.5 nm due to an increase of the optical depth. The hypothesized scaling with E_{encl} does not account for the increase in optical depth due to increased (underheated) plasma dimensions.

The SP Fig. 5.5(b) shows a similar trend to CE, albeit with a much lower rate of increase of SP with E_{encl}. The SP of 70 µm flat-top beam is, with a particularly large value of 10.3%, an outlier due to the target diameter of 116 µm being smaller than the 270–280 µm target diameter of the remaining data. A heuristic linear fit on the SP data, depicted as a dashed line in Fig. 5.5(b), indicates a near-linear increase in SP with increasing E_{encl}.

In Fig. 5.2(a), we show that CE increases dramatically with laser intensity before reaching the laser intensity of $0.7\,\mathrm{W/cm^2}$ for optimum plasma heating, and CE only drops moderately at higher intensities. A low E_{encl} of 20% means that 80% of the laser energy is impinging on the target at local intensities below half the peak intensity. Therefore, this beam profile is composed of a higher fraction of relatively low local intensities than a beam profile with $E_{\text{encl}} = 70\%$, that has a comparable *average* beam intensity. If the overall average intensity is close to optimal, E_{encl} directly gives the fraction of local intensities that are optimal for heating. $E_{\text{encl}} = 100\%$ would practically indicate a beam profile, where the local intensity at every position within the beam profile leads to close to optimum heating of the plasma to generate a charge-state balance that emits most in-band radiation. The fraction of the energy in the beam areas that have local intensities below the optimum increases proportionally with decreasing $E_{\text{encl}} < 100\%$. Since, as already established, the CE drops sharply with intensities below the optimum, the contribution from laser energy at such lower local intensities to the overall CE becomes insignificant. If the contribution is completely neglected, one can assume a linear decrease in CE with decreasing E_{encl} as observed in Fig. 5.5(a). Based on extrapolating the linear fit function, if this linear scaling holds up to nearly $E_{\mathrm{encl}} = 100\%$, one would expect a CE even larger than 5% for a perfect flat beam with a uniform intensity distribution at optimal intensity. SP also increases with increasing E_{encl} as shown in Fig. 5.5(b). The decrease of SP with decreasing E_{encl} can be attributed to the spectral emission from at wavelengths >15 nm due to a higher contribution of low-intensity parts of beams with $E_{\mathrm{encl}} < 50\%$, as observed in Fig. 5.4(f), due to the generation of a larger fraction of locally underheated plasma. This observation supports our explanation for the increase in CE with increasing E_{encl} because less laser energy contributes to an underheated plasma. Furthermore, one would expect the SP to decrease with decreasing E_{encl} due to spectral broadening caused by the underheated plasma corona, which increases optical depth in a multi-zone plasma, similar to the observations in Ch.2. Note that the radiative efficiency η_{rad} is also significantly lower, with values of around 0.3 for MP beams with $E_{\mathrm{encl}} < 50\%$, than flat-top MPs with $E_{\mathrm{encl}} \approx 70\%$ (cf. Fig. 5.4(c) and Fig. 5.3(c)). Therefore, less laser energy contributes to EUV emission from the spectral range of 5.5–25.5 nm.

5.4 Conclusion

We have studied plasmas from pre-pulse preformed tin targets using main pulses (MP) with flat-top beam profiles ranging in diameter from 70 to 144 µm at 2-µm wavelength. Record-high conversion efficiencies (CE) for solid-state laser driven EUV tin plasmas of up to 4.7% are achieved, significantly higher than the CE of up to 3% for Gaussian-shaped MP profiles, as demonstrated in previous Chapters. This increase in CE is attributed to a higher enclosed energy fraction E_{encl} in the case of a flat-top beam compared to a Gaussian beam profile, leading to a greater contribution of laser energy at optimal laser intensity. We observe a linear increase of CE with E_{encl} that, when extrapolated, would point out the possibility of reaching CEs above 5% for improved flat-top beam profiles. Therefore, E_{encl} is an important parameter to consider when designing future EUV sources.

Furthermore, target size scans show that flat-top beams reach full geometric overlap at target sizes closer to the actual beam spot size than for a Gaussian MP, allowing for more compact target and plasma sizes. Confirming the results of the previous Chapter 4, we find that CE, spectral purity (SP), radiative efficiency (η_{rad}), and the angular emission profile do not show strong dependence with laser intensity I_{L}, once optimum heating at $I_{\mathrm{L}} = 0.5\times10^{11}$ W/cm^2 is approximately reached. Furthermore, these plasma parameters are found to be nearly independent of the laser pulse duration (up to 31 ns) and MP flat-top spot diameter (up to 144 µm). Using the scaling with laser intensity, pulse duration, and spot size, we achieve an in-band energy $E_{\mathrm{IB},2\pi}$ of ca. 13 mJ at a conversion efficiency of 4.2%.

These results motivate further studies to enhance the conversion efficiency by improving the enclosed energy of the laser beam profile. Additionally, in-band energy scaling by, e.g., using longer laser pulse durations beyond the parameter space discussed in this work should be investigated to achieve in-band EUV pulse energies of several 10 mJ — bringing the concept of using a 2-µm drive laser for EUV lithography even closer to true application.

CONCLUSION & OUTLOOK

We aim to present a compelling case for the use of solid-state lasers with their typically high wall-plug efficiencies and ease of use, at possibly an optimum wavelength of 2-µm, for the future generation of EUV light from laser-produced plasma in nanolithographical applications in the semiconductor industry. In our scientific approach to substantiate these prospects, we have built a MOPA laser system from the ground up and applied it in characterizations of EUV light production at 13.5 nm in tin-laser-produced plasma. Over the course of the investigations in this Thesis, we have gained an in-depth understanding of the effects of the studied drive laser wavelength on plasma parameters and showcased the potential of 2-µm-wavelength solid-state lasers for future EUV sources. In the following section, we briefly summarize the main characteristics of the 2-µm-wavelength laser system introduced in Chapter 1 and discuss the key findings and conclusions obtained using this laser system in pathfinding EUV plasma experiments before giving an outlook for the future development of 2-µm-driven EUV sources.

In Chapter 1, we introduce a ns-pulsed laser system, capable of producing high laser pulse energies at 2-µm- wavelength, that has been used as a drive laser in various EUV plasma studies presented in Chapters 2–5. This laser system is based on a parametric oscillator power amplifier (MOPA) architecture with an optical parametric oscillator (OPO) generating 2-µm wavelength light that is amplified by an optical parametric amplifier (OPA). This laser architecture enables high laser pulse energies of up to 800 mJ, signal (2090 nm wavelength) and idler (2167 nm) combined, from 2 J of pump energy provided by a Nd:YAG pump laser operating at 1064 nm. These high laser pulse energies are obtained using four KTP crystals in the OPA stage and are reached while maintaining a good beam quality of $M^2 \approx 5$. In addition to favorable spatial properties, the MOPA can generate box-shaped temporal pulses with a tunable pulse duration from 10–24 ns due to the temporal pulse shaping capabilities of the Nd:YAG pump laser. Close to the 44% saturation level of the conversion efficiency of 1-µm- to 2-µm wavelength light, the spatial beam follows the flat-top shape of the pump beam. In the temporal domain, we observed analogous behavior, where the output pulse tends toward a box-shaped temporal profile, resembling the input pump pulse, as the pump intensity increases. Flat-top spatial and box-shaped temporal profiles are realized because of saturation effects of the conversion efficiency in the OPA stage.

At the highest output energies, the beam divergence allows the imaging of a highly intense flat-top profile with $\geq 60\,\mu$m diameter as has been demonstrated and applied in Chapter 5. EUV plasma studies require powerful pulsed laser radiation to irradiate sub-100 µm tin microdroplets at high intensities. Hence, achieving the MOPA system was a crucial first step in enabling all 2-µm-wavelength EUV plasma experiments presented in Chapters 2–5. Note that the MOPA laser system does not have the characteristics for a foreseen industrial application: the repetition rate is limited to 10 Hz without a prospect of scaling to multiple kHz, while the wall-plug conversion is certainly not what is aimed for with true solid-state lasers (where 20% may be in reach - once such systems will be developed).

Since previous studies on solid-state-laser driven tin plasmas were conducted primarily using 1-µm-wavelength from Nd:YAG lasers, we start out with experiments comparing 1-µm- with 2-µm-wavelength driven EUV tin plasmas as presented in Chapters 2 and 3. In these experiments, it is found that the laser intensity that is required to maintain a certain plasma temperature scales approximately inversely with the drive laser wavelength, when going from 1- to 2-µm drive laser wavelength. Chapter 3 explains how the reduced plasma density in the 2-µm case compared to the 1-µm case leads to this scaling. Aside from reducing the laser intensity required to optimally drive an EUV plasma, the reduced plasma density also impacts the obtainable conversion efficiency (CE) of laser pulse energy into usable in-band radiation at 13.5 nm within the 2% wavelength bandwidth emitted in the backward 2π steradian hemisphere. Using a Gaussian-shaped beam (temporally and spatially) in Chapter 2 in a first experiment using 2-µm light, the conversion efficiency is found to be around 3%, which is about a factor two larger than the CE of the 1-µm case under similar conditions. The difference in CE is qualitatively explained by additional self-absorption effects due to a higher density of the underheated plasma corona in the 1-µm case. In addition, from our microdroplet experiments shown in Chapter 3, we demonstrate a significant reduction in the optical depth of the 2-µm driven plasma due to the lower plasma density when compared to the 1-µm driver. This reduction in optical depth leads to less spectral broadening and consequently to a more efficient out-coupling of 13.5 nm in-band radiation even at larger plasma sizes compared to the 1-µm case. The reduced optical depth points out the possibility of irradiating preformed, extended tin sheet targets with 2-µm-wavelength light for better use of tin mass and improved geometric overlap between laser beam and target. This concept is studied in Chapter 4, where we find similar CEs of up to 3% and two times larger CE than the 1-µm case, as with the planar-solid target in Chapter 2. In the 2-µm case, it is found that the CE follows the geometric overlap between target and beam when the target size is varied. Interestingly, the CE and several other plasma parameters seem to be nearly independent of laser intensity and laser pulse duration in the here-studied parameter range. This independence indicates a close-to-linear scaling potential of the in-band energy with laser intensity and laser pulse duration.

In Chapter 5, we further study the scaling of in-band energy in addition to using flat-top beam profiles and box-shaped pulse shapes extending up to 31 ns. Chapter 5 shows that moving from Gaussian-shaped profiles to uniform flat-top profiles drastically increases the CE from about 3% up to 4.7% where the CE follows the increased relative energy fraction E_{encl} enclosed within the FWHM contour of the beam profile. We explain this behavior by the fact that the flat-top beam has more laser energy available at laser intensities sufficient for efficient EUV generation. A CE value of 4.7% marks a record value for solid-state-laser-driven EUV tin plasmas and significantly outperforms the 3.2% record obtained using a 1-µm-wavelength Nd:YAG laser [16]. Extrapolating our results, even CEs exceeding 5% seem possible for improved flat-top spatial beam profiles with $E_{\mathrm{encl}} > 90\%$. Confirming and extending the findings in Chapter 4, a close-to-linear scaling of the in-band energy with laser intensity, pulse duration, and laser spot area size with close to no loss in CE is found. All scaling parameters combined, an in-band energy of 13 mJ emitted in the 2π steradian angle with a 4.2% CE is achieved at 31 ns pulse duration and 140 µm beam spot diameter. Our findings indicate the possibility of scaling the in-band energy by means of the aforementioned laser irradiation parameters without significant impairment of the obtainable CE, which remains around 4-5%.

A CE of 5% close to the 6% CE achieved by traditional CO_2-gas lasers in combination with promising concepts for efficient solid-state laser systems makes the 2-µm-drive wavelength an attractive option for future EUV sources. Comparing the typical wall-plug efficiency of 20% of a solid-state laser combined with the 5% CE in the 2-µm case to the 3% wall-plug efficiency of the CO_2-gas laser combined with its 6% CE, a 2-µm solid-state-laser driven EUV source promises more than a five-fold improvement in overall energy efficiency. Furthermore, a 2-µm solid-state-laser driven EUV source would also be about 50% more energy efficient than a 1-µm solid-state-laser driven EUV source, due to a lower CE of (maximally) 3.2% in the 1-µm case. Thus, efficient 2-µm-wavelength solid-state lasers are an attractive alternative to the traditional CO_2-gas laser in EUV lithography without impairing the conversion of laser power to EUV power, but with a substantial improvement of the overall energy efficiency.

The necessary 2-µm-wavelength laser light could be provided by different laser technologies such as the high-power big-aperture thulium (BAT) laser or Ho:YAG lasers. In addition to high CEs, we show the favorable scaling potential of the total usable in-band pulse energy for 2-µm-driven plasmas. Due to the better scalability of laser pulse energy of solid-state laser systems compared to CO_2-gas lasers, the EUV power output of 2-µm-driven plasmas could be scaled by the in-band pulse energy in addition to scaling the repetition rate helping to eventually surpass the total EUV power output of current state-of-the-art EUV sources. To do so, it is necessary to study avenues for efficient tin-mass use in the 2-µm case. Knowing about the tin mass consumption rate and the dynamics of the liquid tin phase after laser impact is vital to ensure an efficient and sufficient supply of tin even at higher laser pulse energies.

Looking forward to further investigating the feasibility of industrial application of 2-µm-wavelength solid-state lasers, one should increase the laser pulse energy of the MOPA laser system to the joule-level to enable studying the scaling of EUV in-band energy to 30 mJ and beyond. In particular, the laser pulse durations should be scaled to 100 ns and beyond to aim for a complete depletion of the entire tin target mass. This endeavor would require several updates to the MOPA such as improved anti-reflective coatings on the KTP crystals to avoid laser-induced damage potentially caused by increasing the laser pulse energy along with the pulse duration of the Nd:YAG laser used for pumping the MOPA. In addition, one might even consider replacing the entire OPA stage by a Tm:YLF laser amplifier to amplify 1.88-µm-wavelength seed light. A Tm:YLF amplifier could provide a joule-class energy output at pulse duration exceeding 100 ns, based on the approach of Tamer et al. [18]. Furthermore, it is advisable to optimize the seed used in the MOPA for an improved spatial beam profile, and overall beam quality and stability. This measure could help to enhance the energy fraction enclosed within the FWHM of the flat-top beam profile to eventually maximize the CE. Besides improving the 2-µm drive laser used in experiments, additional studies are necessary to further investigate different “plasma recipes” such as main-pulse only operation with elongated pulse duration to aim for high in-band energies at smaller beam spot sizes. These additional studies should also aim to get an understanding of how many tin mass atoms contribute to the EUV emission per incoming laser photon to optimize tin mass use, especially at higher laser pulse energies. It is still not known how efficiently tin mass is used in the 2-µm case compared to the 10-µm case of the CO_2 laser-powered EUV source. In addition, it would be viable to study and understand the full energy balance including out-of-band emission and ion emission of a 2-µm EUV source relative to the 10-µm case. These studies are crucial for gauging the debris generation and the potential risk to the collector mirror in a possible industrial application 2-µm drive laser light powering future EUV sources.

BIBLIOGRAPHY

[1] J. Koomey, S. Berard, M. Sanchez, and H. Wong, *Implications of historical trends in the electrical efficiency of computing*, IEEE Annals of the History of Computing **33**, 46–54 (2011).

[2] I. Fomenkov, *EUV Source for Lithography in HVM: performance and prospects*, EUV Source Workshop 2019, presented: November 5, 2019.

[3] U. Gupta, Y. G. Kim, S. Lee, J. Tse, H.-H. S. Lee, G.-Y. Wei, D. Brooks, and C.-J. Wu, *Chasing carbon: the elusive environmental footprint of computing*, in 2021 IEEE International symposium on high-performance computer architecture (hpca) (2021), pp. 854–867.

[4] A. Killi, I. Zawischa, D. Sutter, J. Kleinbauer, S. Schad, J. Neuhaus, and C. Schmitz, *Current status and development trends of disk laser technology - art. no. 68710l*, Proceedings of SPIE - The International Society for Optical Engineering, `10.1117/12.761664` (2008).

[5] C. N. Danson, C. Haefner, J. Bromage, T. Butcher, J.-C. F. Chanteloup, E. A. Chowdhury, A. Galvanauskas, L. A. Gizzi, J. Hein, D. I. Hillier, N. W. Hopps, Y. Kato, E. A. Khazanov, R. Kodama, G. Korn, R. Li, Y. Li, J. Limpert, J. Ma, N. Chang-hee, D. Neely, D. Papadopoulos, R. R. Penman, L. Qian, J. J. Rocca, A. A. Shaykin, C. W. Siders, C. Spindloe, S. Szatmári, R. M. G. M. Trines, J. Zhu, P. Zhu, and J. D. Zuegel, *Petawatt and exawatt class lasers worldwide*, High Power Laser Sci. Eng. **7** (2019).

[6] E. Sistrunk, D. A. Alessi, A. Bayramian, K. Chesnut, A. Erlandson, T. C. Galvin, D. Gibson, H. Nguyen, B. Reagan, K. Schaffers, C. W. Siders, T. Spinka, and C. Haefner, *Laser Technology Development for High Peak Power Lasers Achieving*

Kilowatt Average Power and Beyond, in Short-pulse high-energy lasers and ultrafast optical technologies, Vol. 11034 (SPIE, 2019), pp. 1 –8.

[7] D. J. Hemminga, O. O. Versolato, and J. Sheil, *Simulations of plasmas driven by laser wavelengths in the 1:0642—10:6 μm range for their characterization as future extreme ultraviolet light sources*, Physics of Plasmas **30**, 033301 (2023).

[8] Lars Behnke, "Euv radiation source", Patent WO2021228517 (2021), International Patent WO/2021/228517.

[9] F. K. Tittel, D. Richter, and A. Fried, "Mid-infrared laser applications in spectroscopy", in *Solid-state mid-infrared laser sources* (Springer Berlin Heidelberg, Berlin, Heidelberg, 2003), pp. 458–529.

[10] T. Wagener, N. Demma, J. Kmetec, and T. Kubo, *2 μm LIDAR for laser-based remote sensing: flight demonstration and application survey*, IEEE Aerospace and Electronic Systems Magazine **10**, 23–28 (1995).

[11] V. Serebryakov, E. Boĭko, N. Petrishchev, and A. Yan, *Medical applications of mid-IR lasers. Problems and prospects*, J. Opt. Technol. **77**, 6–17 (2010).

[12] V. Petrov, *Parametric down-conversion devices: the coverage of the mid-infrared spectral range by solid-state laser sources*, Optical Materials **34**, 536–554 (2012).

[13] A. Godard, *Infrared (2–12 μm) solid-state laser sources: a review*, Comptes Rendus Physique **8**, 1100–1128 (2007).

[14] J. Ma, Z. Qin, G. Xie, L. Qian, and D. Tang, *Review of mid-infrared mode-locked laser sources in the 2.0 μm–3.5 μm spectral region*, Applied Physics Reviews **6**, 021317 (2019).

[15] L. Behnke, R. Schupp, Z. Bouza, M. Bayraktar, Z. Mazzotta, R Meijer, J Sheil, S Witte, W Ubachs, R. Hoekstra, et al., *Extreme ultraviolet light from a tin plasma driven by a 2-μm-wavelength laser*, Opt. Express **29**, 4475–4487 (2021).

[16] R. Schupp, F. Torretti, R. A. Meijer, M. Bayraktar, J. Scheers, D. Kurilovich, A. Bayerle, K. S. E. Eikema, S. Witte, W. Ubachs, R. Hoekstra, and O. O. Versolato, *Efficient generation of extreme ultraviolet light from Nd:YAG-driven microdroplet-tin plasma*, Phys. Rev. Appl. **12**, 014010 (2019).

[17] I. Tamer, B. A. Reagan, T. Galvin, J. Galbraith, E. Sistrunk, A. Church, G. Huete, H. Neurath, and T. Spinka, *Demonstration of a compact, multi-joule, diode-pumped Tm:YLF laser*, Opt. Lett. **46**, 5096–5099 (2021).

[18] I. Tamer, B. A. Reagan, T. Galvin, F. Batysta, E. Sistrunk, D. Willard, A. Church, H. Neurath, J. Galbraith, G. Huete, and T. Spinka, *1 GW peak power and 100 J pulsed operation of a diode-pumped Tm:YLF laser*, Opt. Express **30**, 46336–46343 (2022).

[19]G. A. Rines, D. M. Rines, and P. F. Moulton, *Efficient, high-energy, KTP optical parametric oscillators pumped with 1 micron Nd-lasers*, in Advanced solid state lasers (1994), PO9.

[20]M. S. Webb, P. F. Moulton, J. J. Kasinski, R. L. Burnham, G. Loiacono, and R. Stolzenberger, *High-average-power* $KTiOAsO_4$ *optical parametric oscillator*, Opt. Lett. **23**, 1161–1163 (1998).

[21]A. V. Smith and M. S. Bowers, *Image-rotating cavity designs for improved beam quality in nanosecond optical parametric oscillators*, J. Opt. Soc. Am. B **18**, 706–713 (2001).

[22]G. Arisholm, Ø. Nordseth, and G. Rustad, *Optical parametric master oscillator and power amplifier for efficient conversion of high-energy pulses with high beam quality*, Opt. Express **12**, 4189–4197 (2004).

[23]B. C. Johnson, V. J. Newell, J. B. Clark, and E. S. McPhee, *Narrow-bandwidth low-divergence optical parametric oscillator for nonlinear frequency-conversion applications*, J. Opt. Soc. Am. B **12**, 2122–2127 (1995).

[24]W. A. Neuman and S. P. Velsko, *Effect of cavity design on optical parametric oscillator performance*, in Advanced solid state lasers (1996), OP12.

[25]J. N. Farmer, M. S. Bowers, and W. S. Scharpf, *High brightness eyesafe optical parametric oscillator using confocal unstable resonators*, in Advanced solid state lasers (1999), WC2.

[26]S. Haidar and H. Ito, *Injection-seeded optical parametric oscillator for efficient difference frequency generation in mid-IR*, Optics Communications **171**, 171–176 (1999).

[27]Y. Ehrlich, S. Pearl, and S. Fastig, *High brightness tunable tandem optical parametric oscillator at 8-12* μm, in Advanced solid-state photonics (tops) (2004), p. 398.

[28]D. J. Armstrong and A. V. Smith, *Demonstration of improved beam quality in an image-rotating optical parametric oscillator*, Opt. Lett. **27**, 40–42 (2002).

[29]A. V. Smith and D. J. Armstrong, *Nanosecond optical parametric oscillator with 90° image rotation: design and performance*, J. Opt. Soc. Am. B **19**, 1801–1814 (2002).

[30]W. R. Bosenberg and D. R. Guyer, *Broadly tunable, single-frequency optical parametric frequency-conversion system*, J. Opt. Soc. Am. B **10**, 1716–1722 (1993).

[31]J. C. McCarthy, R. C. Day, and E. P. Chicklis, *Novel, efficient, high brightness KTP optical parametric oscillator - amplifier in single beamline*, in Advanced solid-state lasers (2001), WD4.

[32] R Schupp, L. Behnke, J Sheil, Z Bouza, M Bayraktar, W Ubachs, R. Hoekstra, and O. O. Versolato, *Characterization of 1- and 2-μm-wavelength laser-produced microdroplet-tin plasma for generating extreme-ultraviolet light*, Phys. Rev. Res. **3**, 013294 (2021).

[33] R. Schupp, L. Behnke, Z. Bouza, Z. Mazzotta, Y. Mostafa, A Lassise, L. Poirier, J. Sheil, M. Bayraktar, W. Ubachs, et al., *Characterization of angularly resolved EUV emission from 2-μm-wavelength laser-driven Sn plasmas using preformed liquid disk targets*, J. Phys. D **54** (2021).

[34] A. Godard, M. Guionie, J.-B. Dherbecourt, J.-M. Melkonian, and M. Raybaut, *Backward optical parametric oscillator threshold and linewidth studies*, J. Opt. Soc. Am. B **39**, 408–420 (2022).

[35] G. Arisholm, R. Paschotta, and T. Südmeyer, *Limits to the power scalability of high-gain optical parametric amplifiers*, J. Opt. Soc. Am. B **21**, 578–590 (2004).

[36] A. V. Smith, *Crystal nonlinear optics: with SNLO examples* (AS-Photonics, Albuquerque, NM, USA, 2018), p. 58.

[37] A. V. Smith, R. J. Gehr, and M. S. Bowers, *Numerical models of broad-bandwidth nanosecond optical parametric oscillators*, J. Opt. Soc. Am. B **16**, 609–619 (1999).

[38] A. V. Smith, AS-Photonics, *Snlo nonlinear optics code*, `https://as-photonics.com/products/snlo/`, version 79, Albuquerque, NM, 2023.

[39] O. O. Versolato, *Physics of laser-driven tin plasma sources of EUV radiation for nanolithography*, Plasma Sources Sci. Technol. **28**, 083001 (2019).

[40] M. Purvis, I. V. Fomenkov, A. A. Schafgans, M. Vargas, S. Rich, Y. Tao, S. I. Rokitski, M. Mulder, E. Buurman, M. Kats, J. Stewart, A. D. LaForge, C. Rajyaguru, G. Vaschenko, A. I. Ershov, R. J. Rafac, M. Abraham, D. C. Brandt, and D. J. Brown, *Industrialization of a robust EUV source for high-volume manufacturing and power scaling beyond 250W*, in Extreme ultraviolet (euv) lithography ix, Vol. 10583 (SPIE, 2018), p. 1058327.

[41] M. A. Purvis, A. Schafgans, D. J. W. Brown, I. Fomenkov, R. Rafac, J. Brown, Y. Tao, S. Rokitski, M. Abraham, M. Vargas, S. Rich, T. Taylor, D. Brandt, A. Pirati, A. Fisher, H. Scott, A. Koniges, D. Eder, S. Wilks, A. Link, and S. Langer, *Advancements in predictive plasma formation modeling*, in Extreme ultraviolet (euv) lithography vii, Vol. 9776 (SPIE, 2016), pp. 159 –170.

[42] A. A. Schafgans, D. J. Brown, I. V. Fomenkov, R. Sandstrom, A. Ershov, G. Vaschenko, R. Rafac, M. Purvis, S. Rokitski, Y. Tao, D. J. Riggs, W. J. Dunstan, M. Graham, N. R. Farrar, D. C. Brandt, N. Böwering, A. Pirati, N. Harned, C. Wagner, H. Meiling, and R. Kool, *Performance optimization of MOPA pre-pulse LPP light source*, in Extreme ultraviolet (euv) lithography vi, Vol. 9422 (SPIE, 2015), pp. 56 –66.

[43] F. Torretti, J. Sheil, R. Schupp, M. M. Basko, M. Bayraktar, R. A. Meijer, S. Witte, W. Ubachs, R. Hoekstra, O. O. Versolato, A. J. Neukirch, and J Colgan, *Prominent radiative contributions from multiply-excited states in laser-produced tin plasma for nanolithography*, Nat. Commun. **11**, 2334 (2020).

[44] G. O'Sullivan, B. Li, R. D'Arcy, P. Dunne, P. Hayden, D. Kilbane, T. McCormack, H. Ohashi, F. O'Reilly, P. Sheridan, E. Sokell, C. Suzuki, and T. Higashiguchi, *Spectroscopy of highly charged ions and its relevance to EUV and soft x-ray source development*, J. Phys. B **48**, 144025 (2015).

[45] V. I. Azarov and Y. N. Joshi, *Analysis of the* $4d^7$*-*$4d^6 5p$ *transition array of the eighth spectrum of tin: Sn VIII*, J. Phys. B **26**, 3495–3514 (1993).

[46] S. S. Churilov and A. N. Ryabtsev, *Analysis of the spectra of In XII–XIV and Sn XIII–XV in the far-VUV region*, Opt. Spectrosc. **101**, 169–178 (2006).

[47] A. N. Ryabtsev, É. Y. Kononov, and S. S. Churilov, *Spectra of rubidium-like Pd X-Sn XIV ions*, Opt. Spectrosc. **105**, 844–850 (2008).

[48] H. Ohashi, S. Suda, H. Tanuma, S. Fujioka, H. Nishimura, A. Sasaki, and K. Nishihara, *EUV emission spectra in collisions of multiply charged Sn ions with He and Xe*, J. Phys. B **43**, 065204 (2010).

[49] J. Colgan, D. P. Kilcrease, J. Abdallah, M. E. Sherrill, C. J. Fontes, P. Hakel, and G. S. J. Armstrong, *Atomic structure considerations for the low-temperature opacity of Sn*, High Energy Density Phys. **23**, 133–137 (2017).

[50] F. Torretti, A. Windberger, A. Ryabtsev, S. Dobrodey, H. Bekker, W. Ubachs, R. Hoekstra, E. V. Kahl, J. C. Berengut, J. R. C. López-Urrutia, and O. O. Versolato, *Optical spectroscopy of complex open-*4*d-shell ions* $\mathrm{Sn}^{7+} - \mathrm{Sn}^{10+}$, Phys. Rev. A **95**, 042503 (2017).

[51] R. Schupp, F. Torretti, R. A. Meijer, M. Bayraktar, J. Sheil, J. Scheers, D. Kurilovich, A. Bayerle, A. A. Schafgans, M. Purvis, K. S. E. Eikema, S. Witte, W. Ubachs, R. Hoekstra, and O. O. Versolato, *Radiation transport and scaling of optical depth in Nd:YAG laser-produced microdroplet-tin plasma*, Appl. Phys. Lett. **115**, 124101 (2019).

[52] J. R. Freeman, S. S. Harilal, B. Verhoff, A. Hassanein, and B. Rice, *Laser wavelength dependence on angular emission dynamics of Nd:YAG laser-produced Sn plasmas*, Plasma Sources Sci. Technol. **21**, 055003 (2012).

[53] S. S. Harilal, T. Sizyuk, A. Hassanein, D. Campos, P. Hough, and V. Sizyuk, *The effect of excitation wavelength on dynamics of laser-produced tin plasma*, J. Appl. Phys. **109**, 063306 (2011).

[54] S. Fujioka, H. Nishimura, K. Nishihara, A. Sasaki, A. Sunahara, T. Okuno, N. Ueda, T. Ando, Y. Tao, Y. Shimada, K. Hashimoto, M. Yamaura, K. Shigemori, M. Nakai, K. Nagai, T. Norimatsu, T. Nishikawa, N. Miyanaga, Y. Izawa, and K. Mima, *Opacity Effect on Extreme Ultraviolet Radiation from Laser-Produced Tin Plasmas*, Phys. Rev. Lett. **95**, 235004 (2005).

[55] H. Tanaka, A. Matsumoto, K. Akinaga, A. Takahashi, and T. Okada, *Comparative study on emission characteristics of extreme ultraviolet radiation from* CO_2 *and Nd:YAG laser-produced tin plasmas*, Appl. Phys. Lett. **87**, 041503 (2005).

[56] P. Hayden, A. Cummings, N. Murphy, G. O'Sullivan, P. Sheridan, J. White, and P. Dunne, *13.5 nm extreme ultraviolet emission from tin based laser produced plasma sources*, J. Appl. Phys. **99**, 093302 (2006).

[57] J. White, P. Dunne, P. Hayden, F. O'Reilly, and G. O'Sullivan, *Optimizing 13.5 nm laser-produced tin plasma emission as a function of laser wavelength*, Appl. Phys. Lett. **90**, 181502 (2007).

[58] C. W. Siders, A. C. Erlandson, T. C. Galvin, H. Frank, S. Langer, B. A. Reagan, H. Scott, E. F. Sistrunk, and T. M. Spinka, *Efficient high power laser drivers for next-generation High Power EUV sources*, in 2019 Source Workshop (EUV Litho, Inc., 2019), pp. 1–23.

[59] S. Langer, H. Scott, T. Galvin, E. Link, B. Regan, and C. Siders, *Simulations of Laser Driven EUV Sources – the Impact of Laser Wavelength*, EUVL Workshop 2020, presented: June 11, 2020.

[60] V. Bakshi, *EUV sources for lithography*, edited by V. Bakshi, Vol. 149, SPIE Press monograph (SPIE press Bellingham, Washington, 2006) Chap. 11.

[61] M. M. Basko, *On the maximum conversion efficiency into the 13.5-nm extreme ultraviolet emission under a steady-state laser ablation of tin microspheres*, Phys. Plasmas **23**, 083114 (2016).

[62] K. Bergmann, S. V. Danylyuk, and L. Juschkin, *Optimization of a gas discharge plasma source for extreme ultraviolet interference lithography at a wavelength of 11 nm*, Journal of Applied Physics **106**, 073309 (2009).

[63] A. P. Shevelko, L. A. Shmaenok, S. S. Churilov, R. K. F. J. Bastiaensen, and F. Bijkerk, *Extreme ultraviolet spectroscopy of a laser plasma source for lithography*, Phys. Scr. **57**, 276–282 (1998).

[64] R. L. Kauffman, D. W. Phillion, and R. C. Spitzer, *X-ray production ~13 nm from laser-produced plasmas for projection x-ray lithography applications*, Appl. Opt. **32**, 6897–6900 (1993).

[65] S. S. Harilal, B. O. Shay, M. S. Tillack, Y. Tao, R. Paguio, A. Nikroo, and C. A. Back, *Spectral control of emissions from tin doped targets for extreme ultraviolet lithography*, J. Appl. Phys. **39**, 484–487 (2006).

[66] Y. Tao, S. S. Harilal, M. S. Tillack, K. L. Sequoia, B. O'Shay, and F. Najmabadi, *Effect of focal spot size on in-band 13.5 nm extreme ultraviolet emission from laser-produced Sn plasma*, Opt. Lett. **31**, 2492–2494 (2006).

[67] R. W. Coons, S. S. Harilal, D. Campos, and A. Hassanein, *Analysis of atomic and ion debris features of laser-produced Sn and Li plasmas*, J. Appl. Phys. **108**, 063306 (2010).

[68] R. C. Spitzer, T. J. Orzechowski, D. W. Phillion, R. L. Kauffman, and C. Cerjan, *Conversion efficiencies from laser-produced plasmas in the extreme ultraviolet regime*, J. Appl. Phys. **79**, 2251–2258 (1996).

[69] D. Campos, S. S. Harilal, and A. Hassanein, *The effect of laser wavelength on emission and particle dynamics of Sn plasma*, J. Appl. Phys. **108**, 113305 (2010).

[70] S. A. George, W. T. Silfvast, K. Takenoshita, R. T. Bernath, C.-S. Koay, G. Shimkaveg, and M. C. Richardson, *Comparative extreme ultraviolet emission measurements for lithium and tin laser plasmas*, Opt. Lett. **32**, 997–999 (2007).

[71] A. Z. Giovannini and R. S. Abhari, *Effects of the dynamics of droplet-based laser-produced plasma on angular extreme ultraviolet emission profile*, Appl. Phys. Lett. **104**, 194104 (2014).

[72] Y. Shimada, H. Nishimura, M. Nakai, K. Hashimoto, M. Yamaura, Y. Tao, K. Shigemori, T. Okuno, K. Nishihara, T. Kawamura, A. Sunahara, T. Nishikawa, A. Sasaki, K. Nagai, T. Norimatsu, S. Fujioka, S. Uchida, N. Miyanaga, Y. Izawa, and C. Yamanaka, *Characterization of extreme ultraviolet emission from laser-produced spherical tin plasma generated with multiple laser beams*, Appl. Phys. Lett, **86**, 051501 (2005).

[73] S. S. Harilal, R. W. Coons, P. Hough, and A. Hassanein, *Influence of spot size on extreme ultraviolet efficiency of laser-produced Sn plasmas*, Appl. Phys. Lett. **95**, 221501 (2009).

[74] Y. Ueno, G. Soumagne, A. Sumitani, A. Endo, and T. Higashiguchi, *Enhancement of extreme ultraviolet emission from a* CO_2 *laser-produced Sn plasma using a cavity target*, Appl. Phys. Lett. **91**, 231501 (2007).

[75] R. Amano, T.-H. Dinh, A. Sasanuma, G. Arai, H. Hara, Y. Fujii, T. Hatano, T. Ejima, W. Jiang, A. Sunahara, A. Takahashi, D. Nakamura, T. Okada, K. Sakaue, T. Miura, G. O'Sullivan, and T. Higashiguchi, *Influence of short pulse duration of carbon dioxide lasers on extreme ultraviolet emission from laser-produced plasmas*, Jpn. J. Appl. Phys. **57**, 070311 (2018).

[76] H. Mizoguchi, H. Nakarai, T. Abe, H. Tanaka, Y. Watanabe, T. Hori, Y. Shiraishi, T. Yanagida, G. Soumagne, T. Yamada, and T. Saitou, *Challenge of* $> 300W$ *high power LPP-EUV source with long collector mirror lifetime for semiconductor HVM*, in Extreme ultraviolet (euv) lithography xi, Vol. 11323 (SPIE, 2020), pp. 225 –238.

[77] I. Fomenkov, D. Brandt, A. Ershov, A. Schafgans, Y. Tao, G. Vaschenko, S. Rokitski, M. Kats, M. Vargas, M. Purvis, R. Rafac, B. L. Fontaine, S. D. Dea, A. LaForge, J. Stewart, S. Chang, M. Graham, D. Riggs, T. Taylor, M. Abraham, and D. Brown, *Light sources for high-volume manufacturing EUV lithography: technology, performance, and power scaling*, Adv. Opt. Techn. **6**, 173–186 (2017).

[78] M. Yamaura, S. Uchida, A. Sunahara, Y. Shimada, H. Nishimura, S. Fujioka, T. Okuno, K. Hashimoto, K. Nagai, T. Norimatsu, K. Nishihara, N. Miyanga, Y. Izawa, and C. Yamanaka, *Characterization of extreme ultraviolet emission using the fourth harmonic of a Nd:YAG laser*, Appl. Phys. Lett. **86**, 181107 (2005).

[79] A. Kramida, Yu. Ralchenko, and J. R. and NIST ASD Team, NIST Atomic Spectra Database (ver. 5.3, 2015), http://physics.nist.gov/asd, 2015.

[80] M. Bayraktar, H. M. Bastiaens, C. Bruineman, B. Vratzov, and F. Bijkerk, *Broadband transmission grating spectrometer for measuring the emission spectrum of EUV sources*, NEVAC blad **54**, 14–19 (2016).

[81] R. A. Meijer, A. S. Stodolna, K. S. E. Eikema, and S. Witte, *High-energy Nd:YAG laser system with arbitrary sub-nanosecond pulse shaping capability*, Opt. Lett. **42**, 2758–2761 (2017).

[82] S. S. Churilov and A. N. Ryabtsev, *Analyses of the Sn IX–Sn XII spectra in the EUV region*, Phys. Scr. **73**, 614 (2006).

[83] F. Torretti, R. Schupp, D. Kurilovich, A. Bayerle, J. Scheers, W. Ubachs, R. Hoekstra, and O. O. Versolato, *Short-wavelength out-of-band EUV emission from Sn laser-produced plasma*, J. Phys. B **51**, 045005 (2018).

[84] J. Scheers, C. Shah, A. Ryabtsev, H. Bekker, F. Torretti, J. Sheil, D. A. Czapski, J. C. Berengut, W. Ubachs, J. R. C. López-Urrutia, R. Hoekstra, and O. O. Versolato, *EUV spectroscopy of highly charged* $\mathrm{Sn}^{13+} - \mathrm{Sn}^{15+}$ *ions in an electron-beam ion trap*, Phys. Rev. A **101**, 062511 (2020).

[85] M. M. Basko, V. G. Novikov, and A. S. Grushin, *On the structure of quasi-stationary laser ablation fronts in strongly radiating plasmas*, Phys. Plasmas **22**, 053111 (2015).

[86] T. Sizyuk and A. Hassanein, *Tuning laser wavelength and pulse duration to improve the conversion efficiency and performance of EUV sources for nanolithography*, Phys. Plasmas **27**, 103507 (2020).

[87] T. Ando, S. Fujioka, H. Nishimura, N. Ueda, Y. Yasuda, K. Nagai, T. Norimatsu, M. Murakami, K. Nishihara, N. Miyanaga, Y. Izawa, K. Mima, and A. Sunahara, *Optimum laser pulse duration for efficient extreme ultraviolet light generation from laser-produced tin plasmas*, Appl. Phys. Lett. **89**, 151501 (2006).

[88] O. Morris, F. O'Reilly, P. Dunne, and P. Hayden, *Angular emission and self-absorption studies of a tin laser produced plasma extreme ultraviolet source between 10 and 18 nm*, Appl. Phys. Lett. **92**, 2006–2009 (2008).

[89] K. L. Sequoia, Y. Tao, S. Yuspeh, R. Burdt, and M. S. Tillack, *Two dimensional expansion effects on angular distribution of 13.5nm in-band extreme ultraviolet emission from laser-produced Sn plasma*, Appl. Phys. Lett. **92**, 221505 (2008).

[90] C. Hong, L. Hui, C. Zi-Qi, L. Lu-Ning, T. Tao, Z. Du-Luo, L. Pei-Xiang, and W. Xin-Bing, *Experimental study on laser produced tin droplet plasma extreme ultraviolet light source*, Acta. Phys. Sin. **64**, 075202 (2015).

[91] C.-S. Koay, S. George, K. Takenoshita, R. Bernath, E. Fujiwara, M. Richardson, and V. Bakshi, *High conversion efficiency microscopic tin-doped droplet target laser-plasma source for EUVL*, in Emerging lithographic technologies ix, Vol. 5751 (SPIE, 2005), pp. 279 –292.

[92] S. Yuspeh, Y. Tao, R. A. Burdt, M. S. Tillack, Y. Ueno, and F. Najmabadi, *Dynamics of laser-produced Sn microplasma for a high-brightness extreme ultraviolet light source*, Appl. Phys. Lett. **98**, 201501 (2011).

[93] J. P. Apruzese, J. Davis, K. G. Whitney, J. W. Thornhill, P. C. Kepple, R. W. Clark, C. Deeney, C. A. Coverdale, and T. W. L. Sanford, *The physics of radiation transport in dense plasmas*, Phys. Plasmas **9**, 2411–2419 (2002).

[94] A. Sasaki, A. Sunahara, K. Nishihara, T. Nishikawa, K. Fujima, T. Kagawa, F. Koike, and H. Tanuma, *Atomic modeling of the plasma EUV sources*, High Energy Density Phys. **3**, 250 –255 (2007).

[95] T. Krücken, K. Bergmann, L. Juschkin, and R. Lebert, *Fundamentals and limits for the EUV emission of pinch plasma sources for EUV lithography*, Journal of Physics D: Applied Physics **37**, 3213–3224 (2004).

[96] Z. Bouza, J. Scheers, A. Ryabtsev, R. Schupp, L. Behnke, C. Shah, J. Sheil, M. Bayraktar, J. R. C. López-Urrutia, W. Ubachs, R. Hoekstra, and O. O. Versolato, *EUV spectroscopy of Sn^{5+}–Sn^{10+} ions in an electron beam ion trap and laser-produced plasmas*, J. Phys. B **53**, 195001 (2020).

[97] S. K. Moore, *EUV lithography finally ready for fabs*, IEEE Spectrum **55**, 46–48 (2018).

[98] V. Y. Banine, K. N. Koshelev, and G. H. P. M. Swinkels, *Physical processes in EUV sources for microlithography*, J. Phys. D: Appl. Phys. **44**, 253001 (2011).

[99] J. Benschop, V. Banine, S. Lok, and E. Loopstra, *Extreme ultraviolet lithography: Status and prospects*, J. Vac. Sci. Technol. B **26**, 2204 (2008).

[100] S. S. Churilov and A. N. Ryabtsev, *Analysis of the $4p^64d^7$ - $(4p^64d^64f + 4p^54d^8)$ transitions in the Sn VIII spectrum*, Opt. Spectrosc. **100**, 660–666 (2006).

[101] I. Y. Tolstikhina, S. S. Churilov, A. N. Ryabtsev, and K. N. Koshelev, “Atomic tin data”, in *EUV sources for lithography*, edited by V. Bakshi (SPIE Press, 2006) Chap. 4, pp. 113–148.

[102] R. D’Arcy, H. Ohashi, S. Suda, H. Tanuma, S. Fujioka, H. Nishimura, K. Nishihara, C. Suzuki, T. Kato, F. Koike, J. White, and G. O’Sullivan, *Transitions and the effects of configuration interaction in the spectra of Sn XV–Sn XVIII*, Phys. Rev. A **79**, 042509 (2009).

[103] S. Bajt, J. B. Alameda, T. W. Barbee Jr., W. M. Clift, J. A. Folta, B. Kaufmann, and E. A. Spiller, *Improved reflectance and stability of Mo-Si multilayers*, Opt. Eng. **41**, 1797–1804 (2002).

[104] Q. Huang, V. Medvedev, R. van de Kruijs, A. Yakshin, E. Louis, and F. Bijkerk, *Spectral tailoring of nanoscale EUV and soft x-ray multilayer optics*, Appl. Phys. Rev. **4**, 011104 (2017).

[105] M. M. Basko, J. Maruhn, and A. Tauschwitz, *Development of a 2D radiation-hydrodynamics code RALEF for laser plasma simulations*, GSI report **1**, 410 (2010).

[106] W. Svendsen and G. O’Sullivan, *Statistics and characteristics of XUV transition arrays from laser-produced plasmas of the elements tin through iodine*, Phys. Rev. A **50**, 3710–3718 (1994).

[107] F. Torretti, F. Liu, M. Bayraktar, J. Scheers, Z. Bouza, W. Ubachs, R. Hoekstra, and O. O. Versolato, *Spectral characterization of an industrial EUV light source for nanolithography*, J. Phys. D: Appl. Phys. **53**, 055204 (2019).

[108] L. Oster, *Emission, absorption, and conductivity of a fully ionized gas at radio frequencies*, Rev. Mod. Phys. **33**, 525–543 (1961).

[109] H. A. Kramers, *XCIII. On the theory of X-ray absorption and of the continuous X-ray spectrum*, Philos. Mag. **46**, 836–871 (1923).

[110] F. Torretti, J. Sheil, R. Schupp, M. M. Basko, M. Bayraktar, R. A. Meijer, S. Witte, W. Ubachs, R. Hoekstra, O. O. Versolato, A. J. Neukirch, and J. Colgan, *Prominent radiative contributions from multiply-excited states in laser-produced tin plasma for nanolithography*, Nat. Commun. **11**, 2334 (2020).

[111] M. van de Kerkhof, F. Liu, M. Meeuwissen, X. Zhang, M. Bayraktar, R. de Kruif, and N. Davydova, *High-power EUV lithography: spectral purity and imaging performance*, J. Micro Nanolithogr. MEMS MOEMS **19**, 033801 (2020).

[112] H. Mizoguchi, H. Nakarai, T. Abe, K. M. Nowak, Y. Kawasuji, H. Tanaka, Y. Watanabe, T. Hori, T. Kodama, Y. Shiraishi, T. Yanagida, G. Soumagne, T. Yamada, T. Yamazaki, and T. Saitou, *High power LPP-EUV source with long collector mirror lifetime for high volume semiconductor manufacturing*, in Proc. CSTIC 2018 (IEEE, 2018), pp. 1–7.

[113] A. Y. Vinokhodov, M. S. Krivokorytov, Y. V. Sidelnikov, V. M. Krivtsun, V. V. Medvedev, and K. N. Koshelev, *Droplet-based, high-brightness extreme ultraviolet laser plasma source for metrology*, J. Appl. Phys. **120**, 163304 (2016).

[114] J. Bauche, C. Bauche-Arnoult, and M. Klapisch, *Transition arrays in the spectra of ionized atoms*, Adv. Atom. Mol. Phys. **23**, 131–195 (1988).

[115] K. Nishihara, A. Sunahara, A. Sasaki, M. Nunami, H. Tanuma, S. Fujioka, Y. Shimada, K. Fujima, H. Furukawa, T. Kato, et al., *Plasma physics and radiation hydrodynamics in developing an extreme ultraviolet light source for lithography*, Phys. Plasmas **15**, 056708 (2008).

[116] S. Fujioka, M. Shimomura, Y. Shimada, S. Maeda, H. Sakaguchi, Y. Nakai, T. Aota, H. Nishimura, N. Ozaki, A. Sunahara, K. Nishihara, N. Miyanaga, Y. Izawa, and K. Mima, *Pure-tin microdroplets irradiated with double laser pulses for efficient and minimum-mass extreme-ultraviolet light source production*, Appl. Phys. Lett. **92**, 241502 (2008).

[117] H. Matsukuma, A. Sunahara, T. Yanagida, H. Tomuro, K. Kouge, T. Kodama, T. Hosoda, S. Fujioka, and H. Nishimura, *Correlation between laser absorption and radiation conversion efficiency in laser produced tin plasma*, Appl. Phys. Lett. **107**, 121103 (2015).

[118]T. Higashiguchi, N. Dojyo, M. Hamada, W. Sasaki, and S. Kubodera, *Low-debris, efficient laser-produced plasma extreme ultraviolet source by use of a regenerative liquid microjet target containing tin dioxide (SnO_2) nanoparticles*, Appl. Phys. Lett. **88**, 201503 (2006).

[119]D. Nakamura, T. Akiyama, K. Okazaki, K. Tamaru, A. Takahashi, and T. Okada, *Ablation dynamics of tin micro-droplet irradiated by double pulse laser used for extreme ultraviolet lithography source*, J. Phys. D: Appl. Phys. **41**, 245210 (2008).

[120]A. Z. Giovannini and R. S. Abhari, *Three-dimensional extreme ultraviolet emission from a droplet-based laser-produced plasma*, J. Appl. Phys. **114**, 033303 (2013).

[121]I. W. Choi, H. Daido, S. Yamagami, K. Nagai, T. Norimatsu, H. Takabe, M. Suzuki, T. Nakayama, and T. Matsui, *Detailed space-resolved characterization of a laser-plasma soft-x-ray source at 13.5-nm wavelength with tin and its oxides*, J. Opt. Soc. Am. B **17**, 1616–1625 (2000).

[122]D. Kurilovich, A. L. Klein, F. Torretti, A. Lassise, R. Hoekstra, W. Ubachs, H. Gelderblom, and O. O. Versolato, *Plasma propulsion of a metallic microdroplet and its deformation upon laser impact*, Phys. Rev. Appl. **6**, 014018 (2016).

[123]D. Kurilovich, M. M. Basko, D. A. Kim, F. Torretti, R. Schupp, J. C. Visschers, J. Scheers, R. Hoekstra, W. Ubachs, and O. O. Versolato, *Power-law scaling of plasma pressure on laser-ablated tin microdroplets*, Phys. Plasmas **25**, 012709 (2018).

[124]B. Liu, D. Kurilovich, H. Gelderblom, and O. O. Versolato, *Mass Loss from a Stretching Semitransparent Sheet of Liquid Tin*, Phys. Rev. Appl. **13**, 024035 (2020).

[125]B. Liu, R. A. Meijer, J. Hernandez-Rueda, D. Kurilovich, Z. Mazzotta, S. Witte, and O. O. Versolato, *Laser-induced vaporization of a stretching sheet of liquid tin*, J. Appl. Phys. **129**, 053302 (2021).

[126]T. de Faria Pinto, J. Mathijssen, R. Meijer, H. Zhang, A. Bayerle, D. Kurilovich, O. O. Versolato, K. S. E. Eikema, and S. Witte, *Cylindrically and non-cylindrically symmetric expansion dynamics of tin microdroplets after ultrashort laser pulse impact*, Appl. Phys. A **127**, 1–10 (2021).

[127]S. Yuspeh, K. L. Sequoia, Y. Tao, M. S. Tillack, R. Burdt, and F. Najmabadi, *Optimization of the size ratio of Sn sphere and laser focal spot for an extreme ultraviolet light source*, Appl. Phys. Lett. **93**, 221503 (2008).

[128]G. D. O'Sullivan and R. Faulkner, *Tunable narrowband soft x-ray source for projection lithography*, Opt. Eng. **33**, 3978–3984 (1994).

[129]S. A. Reijers, D. Kurilovich, F. Torretti, H. Gelderblom, and O. O. Versolato, *Laser-to-droplet alignment sensitivity relevant for laser-produced plasma sources of extreme ultraviolet light*, J. Appl. Phys. **124**, 013102 (2018).

[130] T. Sizyuk and A. Hassanein, *Tuning laser wavelength and pulse duration to improve the conversion efficiency and performance of EUV sources for nanolithography*, Phys. Plasmas **27**, 103507 (2020).

[131] H. Chen, X. Wang, L. Duan, H. Lan, Z. Chen, D. Zuo, and P. Lu, *Angular distribution of ions and extreme ultraviolet emission in laser-produced tin droplet plasma*, J. Appl. Phys. **117**, 193302 (2015).

[132] H. Gelderblom, H. Lhuissier, A. L. Klein, W. Bouwhuis, D. Lohse, E. Villermaux, and J. H. Snoeijer, *Drop deformation by laser-pulse impact*, J. Fluid Mech. **794**, 676–699 (2016).

[133] J. Hernandez-Rueda, B. Liu, D. J. Hemminga, Y. Mostafa, R. A. Meijer, D. Kurilovich, M. Basko, H. Gelderblom, J. Sheil, and O. O. Versolato, *Early-time hydrodynamic response of a tin droplet driven by laser-produced plasma*, Phys. Rev. Res. **4**, 013142 (2022).

LIST OF PUBLICATIONS

CHAPTER 1

L. Behnke, E. J. Salumbides, G. Göritz, Y. Mostafa, D. Engels, W. Ubachs, and O. O. Versolato, *High-energy parametric oscillator and amplifier pulsed light source at 2-μm*, Opt. Express **31** (2023).

CHAPTER 2

L. Behnke, R. Schupp, Z. Bouza, M. Bayraktar, M. Mazzotta, R. Meijer, J. Sheil, S. Witte, W. Ubachs, R. Hoekstra and O. O. Versolato, *Extreme ultraviolet light from a tin plasma driven by a 2-μm-wavelength laser*, Opt. Express **29** (2021).

CHAPTER 3

R. Schupp, L. Behnke, J. Sheil, Z. Bouza, M. Bayraktar, W. Ubachs, R. Hoekstra and O. O. Versolato, *Characterization of 1- and 2-μm-wavelength laser-produced microdroplet-tin plasma for generating extreme-ultraviolet light*, Phys. Rev. Res. **3** (2021).

CHAPTER 4

R. Schupp, L. Behnke, Z. Bouza, Z. Mazzotta, Y. Mostafa, A. Lassise, L. Poirier, J. Sheil, M. Bayraktar, W. Ubachs, R. Hoekstra and O. O. Versolato, *Characterization of angularly resolved EUV emission from 2-μm-wavelength laser-driven Sn plasmas using preformed liquid disk targets*, J. Phys. D **54** (2021).

PATENT

L. Behnke, *EUV radiation source*, International Patent: WO/2021/228517 (2021).

The author has also contributed to the following publications:

L. Poirier, A. Lassise, Y. Mostafa, L. Behnke, N. Braaksma, L. Assink, R. Hoekstra and O. O. Versolato, *Energy- and charge-state-resolved spectrometry of tin laser-produced plasma using a retarding field energy analyzer*, Applied Physics B **128** (2022).

L. Poirier, A. Bayerle, A. Lassise, F. Torretti, R. Schupp, L. Behnke, Y. Mostafa, W. Ubachs, O. O. Versolato and R. Hoekstra, *Cross-calibration of a combined electrostatic and time-of-flight analyzer for energy- and charge-state-resolved spectrometry of tin laser-produced plasma*, Applied Physics B **128** (2022).

Z. Bouza, J. Byers, J. Scheers, R. Schupp, Y. Mostafa, L. Behnke, Z. Mazzotta, J. Sheil, W. Ubachs, R. Hoekstra, M. Bayraktar and O. O. Versolato, *The spectrum of a 1-μm-wavelength-driven tin microdroplet laser-produced plasma source in the 5.5–265.5 nm wavelength range*, AIP Advances **11** (2021).

Z. Bouza, J. Scheers, A. Ryabtsev, R. Schupp, L. Behnke, C. Shah, J. Sheil, M. Bayraktar, J. Crespo Lopez-Urrutia, W. Ubachs, R. Hoekstra and O. O. Versolato, *EUV spectroscopy of* Sn^{5}*-*Sn^{10+} *ions in an electron beam ion trap and laser-produced plasmas*, J. Phys. B: At. Mol. Opt. Phys **53** (2020).

ACKNOWLEDGMENTS

During the last four years of pursuing my PhD at ARCNL, I have been blessed with the unwavering support of countless individuals whose contributions, both big and small, have shaped this work in many ways. First, I wish to express my deepest gratitude to my advisor, Oscar, whose expertise, guidance, and mentorship have been instrumental in the completion of this thesis. I enjoyed your enthusiasm and positivity, especially when I faced the numerous challenges of my project. Second, I would like to thank my other promoter Wim for his wisdom and guidance. His contributions during our many meetings have been proven invaluable for this thesis. A special note of thanks to Oscar, Wim, and Ronnie for their meticulous proofreading and contributions to my manuscripts.

I also like to thank Ruben, who is responsible for giving me a smooth start at ARCNL, for teaching me all those useful skills required for complex EUV plasma experiments and for building the mighty MOPA laser system. Thanks to you and my close colleagues, Yahia, Zoi, Dion, Adam, Edcel, Lucas, and Youssef, for the great time in the lab. Together, we managed to get amazing results, even after I eventually burned one (or more) KTP crystals (along with some other optics). Special thanks also to Laurens for your hard work and invaluable help in maintaining and improving the experimental setup. I really enjoyed our regular chats in front of the coffee machine!

I am deeply grateful to the entire Source department of ARCNL for making my time at the institute not only productive, but also truly memorable and joyous. I would like to thank Joris, Dmitry, Alex, Francesco, Bo, Randy, John, Javier, Diko, Karl, Klaas, Luc, Jane, Stan, Jorge, Mikheil, Hugo, Kevin, Subam, Mardou, Sander, Bowie, Jaap, and Job. Furthermore, I would like to thank Zeudi, Jan, and Stefan from the

EUV Generation and Imaging group for their insight, comments, and support on the 2-µm-laser development.

Also, many thanks to Wim van der Zande for the fruitful discussions and his grandiose work as director of ARCNL.

This work was also made possible by productive collaboration with a number of people outside of ARCNL. I would like to highlight the contribution of Guido Göritz from GWU for his invaluable first-hand expertise that made the quick realization of the MOPA system possible. This thesis also benefited from insightful discussions with Michael Purvis and his team at ASML San Diego. I eagerly look forward to continuing my journey in the field of EUV sources with ASML San Diego!

I also would like to thank the entire support staff for their guidance and technical advice. In particular, Henk-Jan and Iliya from the mechanical engineering department, who helped many times with great ideas and clever designs. These designs were usually machined by an exceptional mechanical workshop. Since I had to order many things, I also would like to thank the finance and purchasing department and especially to Radjin, André, and Remco. I also thank the entire ICT department for their technical advice and, in particular, Rutger for taking care of my laptop on multiple occasions. A big thank you is also needed for the software department, especially for Jorijn and Marco for their excellent work on our data acquisition software, your work was absolutely crucial for the success of this thesis. I am also grateful for the invaluable advice of the electronics department. Many thanks also to the secretaries Romy, Rosa, Cathelijne, Jusra, and Marga who were always at hand to help.

I really enjoyed my time at ARCNL. This is also thanks to the ARCNL's excellent management team, including Marjan, Joost (former director), and Wim van der Zande (current director). Additionally, I thank the PV for organizing numerous fun activities and group outings. I always had a great time during our coffee / lunch breaks, foosball matches, and occasional beers, thanks to all my amazing colleagues at ARCNL!

Many thanks to my entire family for their support and love, every step of the way. I would like to end my acknowledgments by thanking Rohini, your warmth and your laughter brighten up my day.